THERMAL MODELLING FOR ELECTRIC MACHINES USING THERMAL CAPACITANCE CALCULATION METHOD: EXTERNAL ROTOR SWITCHED RELUCTANCE MOTOR CASE STUDY

THERMAL MODELLING FOR ELECTRIC MACHINES USING THERMAL CAPACITANCE CALCULATION METHOD: EXTERNAL ROTOR SWITCHED RELUCTANCE MOTOR CASE STUDY

By ELIZABETH TRICKETT, B.Sc., M.A.Sc.

A thesis submitted to the McMaster School of Graduate Studies in partial fulfilment of the requirements for the Doctor of Philosophy degree in Mechanical Engineering

Doctor of Philosophy in Mechanical Engineering (2020)

McMaster University, Hamilton, Ontario.

TITLE: Thermal Modelling for Electric Machines Using Thermal Capacitance Calculation Method: External Rotor Switched Reluctance Motor Case Study

AUTHOR: Elizabeth Trickett, B.Sc., M.A.Sc.

SUPERVISOR: Dr. Ali Emadi

PAGES: xxi, 144

Lay Abstract

This thesis deals with the thermal modelling of electric machines for traction applications using lumped parameter thermal modelling. A novel approach is presented for calculating and distributing thermal capacitance in motor coils. A 12/16 External Rotor Switched Reluctance Motor is characterized based on its transient thermal response and the novel methods proposed are validated. The sizing of a coil-based thermal model is discussed and a criterion for physical validity proposed. The validated model is used in a sensitivity analysis of coil and motor capacitances. For severe overload conditions and short periods, a result is obtained showing the coil can be modelled as adiabatic. Finally, a rated load condition is tested, and a transition is suggested between overload conditions and non-overload conditions.

Abstract

This thesis characterizes the transient thermal response of a 12/16 External Rotor Switched Reluctance Machine (ERSRM) for an E-bike application. A method for calculating coil capacitance based on machine design parameters was introduced and implemented into a standard commercial Lumped Parameter Thermal Network (LPTN). A sizing criterion was proposed for the cuboid number in a physically accurate LPTN coil model design. This sizing criterion considers the change in model size with motor speed or forced convection. The LPTN with a more accurate calculation of capacitance within the coil and a known number of cuboids in the coil was validated with experimental results. An analytical proof was provided that a small number of capacitances is not sufficient to model a typical power-dense coil design.

The validated model was used to study the impact of a more accurate capacitance calculation method on motor temperature. Both overload and rated operation were investigated. During overload conditions, it was found that the standard capacitance calculation from commercial software massively underestimated the heating rate and peak temperature of the coil hot spot, even with the same number of cuboids.

The capacitance of the rest of the motor was able to be varied and investigated for its effects on cooldown dynamics. It was found that for short-time transients the coil could be assumed to act adiabatically in this operating range. Operating

points across the operating envelope for the motor under study were mapped to determine the region where the adiabatic assumption could be made. It was shown that a transition occurred where the adiabatic assumption ceases to be valid.

Dedication

This doctoral thesis is dedicated to the memory of Dr. Jason Lo.

To my teacher, my mentor, and my friend: you saw within me what I could not see in myself. May I honour your legacy of kindness, honesty, and courage, and may I be the mentor to others that you were to me.

Acknowledgements

I would like to thank my supervisor, Dr. Ali Emadi, whose kindness, patience, and incredible insight has helped me persevere through an endeavour that has changed my life. You have raised up so many. That you took the time to raise me up too – I will be forever in your debt. You taught me what it meant to build things that last, and I will always remember this lesson.

Next, I wish to thank my supervisory committee, Dr. James Cotton and Dr. Ryan Ahmed. It was a privilege to be able to work with both of you. Each step of the way you always guided me down the right path. The combination of your tremendous knowledge and good humour gave me a lot of hope in equal measure.

I would also like to thank Dr. Berker Bilgin for all his help and support throughout my degree. I learned from your example the rewards of discipline, patience, and hard work. You continue to inspire those around you to new heights.

I have been blessed to be supported by so many communities that I cannot hope to do them all justice. I only hope each one of you knows what you mean to me.

To my colleagues at MARC: we have been through so much together, you are all family to me now. Thank you for sharing so much of yourselves with me and for helping me find my voice. Although the list is not complete, I wanted to recognize Dr. Lea Dorn-Gomba, Dr. Romina Rodriguez, Dr. Diego Fernando Valencia Garcia, Sumedh Dhale, Maryam Alizadeh, Jack Gillies, Dr. Carlos Vidal, Silvio Rotilli, Dr. Joanna Lin and Dr. James Jiang. Special thanks to Dr. Brock Howey for trusting me with his motor.

To my good friends at Canmet who helped put me on the path towards my Ph.D. and supported me to its conclusion, thank you for believing in me.

To my friends and family, thank you for standing by me and for offering me refuge again and again through these many long hours. You were the ones who held my hand when I first took this leap, and your loving-kindness has carried me through.

Finally, to my husband John for his infinite love, joyful encouragement, and indefatigable support. You have been my rock, my light, and my heart. Thank you for taking this wild adventure with me and for being by my side every step of the way.

Contents

Lay Abstract iii

Abstract iv

Dedication vi

Acknowledgements vii

Contents viii

List of Figures xii

List of Tables xvi

List of Abbreviations and Symbols xvii

Declaration of Academic Achievement xxi

Chapter 1 INTRODUCTION 1

1.1 Background and State-of-the-Art 1

1.2 Goals and Contributions 4

1.3 Chapter Overview 6

Chapter 2 FUNDAMENTALS OF HEAT TRANSFER 9

2.1 Energy Transfer 11

2.2 Conduction 13

2.3 Convection 15

2.3.1 Convection Heat Transfer Coefficient 16
2.3.2 Boundary Layers and Dimensionless Numbers 17
2.4 Radiation 22
2.4.1 Blackbody Radiation and the Stephen-Boltzmann Law 23
2.4.2 Radiation Flux and Radiation Intensity 26
2.4.3 View Factor and Radiation Exchange Between Surfaces 32
Chapter 3 FUNDAMENTALS OF SWITCHED RELUCTANCE MACHINES 38
3.1 How Do We Produce Torque? 39
3.1.1 What is Electrical Angle and Rotor Position? 40
3.1.2 What is a Magnetic Circuit? 42
3.1.3 Flux-Linkage-Current Dependency 45
3.2 Maximizing Torque Production and Power Factor 48
3.3 Complications to Torque Production 51
3.4 Sources of Loss 54
3.4.1 Copper Loss 55
3.4.2 Core Loss 58
Chapter 4 LUMPED PARAMETER THERMAL MODELLING FOR ELECTRICAL MACHINES 63
4.1 Lumped Systems Modelling 64

4.1.1 Lumped Parameter Networks 64

4.1.2 Characteristic Length Definition 66

4.2 Heat Transfer Coefficient Approximation in Motors 68

4.2.1 Conductive Heat Transfer 68

4.2.2 Convective Heat Transfer 70

4.2.3 Radiative Heat Transfer 73

4.3 Physically Accurate Lumped Systems in an Electric Machine 75

Chapter 5 THERMAL ANALYSIS OF A 12/16 EXTERNAL ROTOR SWITCHED RELUCTANCE MOTOR 78

5.1 Characterizing the Motor Transient Thermal Response 79

5.1.1 External Rotor Motor Heat Paths 79

5.1.2 Traction Motor Transient Operation 82

5.2 Analysis of Lumped Systems Approximation for Motor Coils 84

5.2.1 Winding System Anisotropy 84

5.2.2 RC Dynamics of Cuboids 86

5.2.3 Lumped Volume Dimensional Analysis 87

Chapter 6 EXPERIMENTAL VALIDATION – 12/16 EXTERNAL ROTOR SWITCHED RELUCTANCE MOTOR 92

6.1 Experimental Investigation 93

6.1.1 Set-up 93

6.1.2 Experimental Results 96

6.2 Stator Winding Thermal Capacitance 100

6.2.1 Methods for Determining Model Capacitance 100

6.2.2 Maximum Packing Factor Model 104

6.3 Implementation and Validation of Physically Accurate Capacitance in LPTN Model 106

Chapter 7 SENSITIVITY ANALYSIS OF VALIDATED LUMPED PARAMETER THERMAL NETWORK MODEL 112

7.1 Dynamics at Severe Overload Conditions 113

7.1.2 Hot-Spot Temperature Profile Sensitivity to Thermal Capacitance Variance 113

7.2 Dynamics Over the Operating Envelope 118

Chapter 8 CONCLUSIONS AND FUTURE WORK 121

8.1 Summary and Conclusions 121

8.2 Future Work 124

Bibliography 127

Appendix A: Lumped Parameter Thermal Network Model Parameters 141

List of Figures

Figure 2-1: A general approach for solving rating heat transfer problems 11

Figure 2-2: A comparison between the fluid characteristics considered in the calculation of the a) Nusselt number, b) Prandtl number and c) Reynolds number 22

Figure 2-3: A solid angle describing radiation intensity of light 27

Figure 2-4: Total radiation leaving a surface with $\epsilon \neq 1$ 30

Figure 2-5: Media with a non-zero transmissivity, $1 > \tau > 0$ 33

Figure 2-6: a) Intensity from specular surfaces varies with direction while b) Diffuse surfaces are equal in all directions [13] 34

Figure 2-7:Illustration of angle factor between two surfaces. 36

Figure 3-1: A fractional model of a 12/8 SRM where the red component is the rotor, the yellow are the coils, the blue is the stator and the purple is the housing [from JMAG] 39

Figure 3-2: Idealized inductance versus rotor position by excited phase 41

Figure 3-3: B-H curve [16] 43

Figure 3-4: Flux path produced by a) a cored solenoid and b) a coreless solenoid 44

Figure 3-5: Flux-linkage vs current for various rotor positions [17] 46

Figure 3-6: Variation of flux linkage with phase current and position 50
Figure 3-7: Phase current and voltage for low speed (blue) and high speed (green). (Adapted from [20]) 53
Figure 3-8: Phase leg of an asymmetric bridge converter for a) forward current, b) reverse current and c) freewheeling [21] 54
Figure 3-9:Power-flow diagram: Loss distribution of a typical switched reluctance machine. (Adapted from [22]) 55
Figure 3-10: Skin effect in a circular wire (left) and proximity effect for adjacent wires with the same current direction (right) [25] 58
Figure 3-11: Curves of core losses at different frequencies, for lamination steel JFE 30JN loss per volume [18] 60
Figure 3-12: 4-phase 16/12 traction SRM flux density curves at low speed (left) and high speed (right) for a single element [36] 61
Figure 4-1: a) Nodalization of the motor geometry b) Node within the classic thermal circuit 65
Figure 5-1: Illustration of the 12/16 E-bike ERSRM 79
Figure 5-2: Internal Rotor SRM Heat Paths 80
Figure 5-3: External Rotor SRM Heat Paths 81
Figure 5-4: Frames of reference for coil heat transfer: a) Motor frame: cross-section illustration in the radial plane of the ERSRM b) Wire frame: radial and axial directions of an individual wire 85

Figure 5-5: Nearest neighbours in the radial wire frame for local equilibrium from an individual wire 89
Figure 6-1: MUT with electrical tape on the radial housing to prepare for measurements by the thermal camera 94
Figure 6-2: Placement of the camera and tripod relative to the motor outer surface 97
Figure 6-3: Thermistor positions are shown schematically which are placed on phases A, B and C 98
Figure 6-4: Temperature over time for the three positions on phases A, B and C 98
Figure 6-5: Temperature over time for the thermistors on one phase vs. the housing temperature 99
Figure 6-6: The heating trend of the three thermistor positions for phase A resampled with a low pass filter, with motor turn off at 113.31 s (vertical line) . 100
Figure 6-7: Motor geometry representation in MotorCAD: radial (top), axial (bottom) 107
Figure 6-8: Main temperature profile regions for phase A, position 3 thermistor 109
Figure 6-9: Torque profile of the MUT during loading 110
Figure 6-10: LPTN with MPF capacitance calculation plotted against the temperature profile for phase A, position 3 thermistor 111
Figure 7-1: Variation in Coil Capacitance for Fifteen Cuboids 114

Figure 7-2: Reduction in stator capacitance by component, ... 116

Figure 7-3: Change in dT/dt by operating point for five-second temperature ‘snapshots’ 119

Figure 7-4: Change in Cooling Profile with Reducing Thermal Capacitance for 25A peak, 150 RPM 120

List of Tables

Table 2-1: Boundary condition examples for a one-dimensional system 14

Table 2-2: Value ranges for types of convection[7] 16

Table 2-3: Factors that distinguish flow classifications [7] 18

Table 2-4: Value ranges for Prandtl number for example fluids 19

Table 6-1: Basic ERSRM Details 94

Table 6-2: Capacitances Comparison between MotorCAD and the Maximum Packing Factor Model 105

Table 6-3: Coil Specifications for the 12/16 ERSRM and Corresponding Model Parameters 108

Table 7-1: Variation of Coil Thermal Capacitances 114

Table 7-2: Variation of Stator Thermal Capacitances 116

List of Abbreviations and Symbols

Q	heat	J
$\dot{Q}$	heat transfer rate	W
$\dot{q}$	average heat flux	W/m^2
$\dot{g}$	rate of heat generation	W/m^3
$\dot{G}$	total rate of heat generation	W/m^3
k	thermal conductivity	W/m^2K
α	thermal diffusivity	m^2/s
h	convection heat transfer coefficient	W/m^2K
ρ	density	kg/m^3
c_p	specific heat at constant pressure	J/(kgK)
Nu	Nusselt number	-
L_c	characteristic length	m
μ	dynamic viscosity	Pa s
Pr	Prandtl number	-
Re	Reynolds number	-
ν	kinematic viscosity	m^2/s
ϵ_{rad}	emissivity	-
α_{rad}	absorptivity	-
E_b	blackbody total emissive power	W/m^2
σ_{rad}	Stephan-Boltzmann constant	$W{\cdot}m^{-2}{\cdot}K^{-4}$
Ω	solid angle	sr
S_{rad}	hemispherical surface area	m^2
I_e	intensity for the total emitted radiation	W/m^2 sr
G_{rad}	radiative flux of the incident radiation	W/m^2
I_i	intensity of incident radiation	W/m^2 sr
E_{rad}	diffusely emitting surface emissive power	W/m^2

J_{rad}	radiosity	W/m^2
I_λ	spectral radiative intensity	W/m^2 sr
λ_{rad}	wavelength	m
τ_{rad}	transmissivity	-
ρ_{rad}	reflectivity	-
$F_{1\,2}$	view factor	-
β_1, β_2	angles away from the normal direction for each face	radians
L	inductance	H
τ	torque	N m
i	current	A
λ	flux-linkage	Wb
S	strokes	-
N_R	number of rotor poles	-
N_{phases}	number of phases	-
θ_{elec}	electrical angle	degrees
θ_{mech}	mechanical angle	degrees
$\boldsymbol{B}$	magnetic flux density	T
$\boldsymbol{H}$	magnetic field intensity	A/m
μ_0	permeability of free space	N/A
μ_r	permeability of the material	-
Φ	magnetic flux density	Wb
N	number of turns	-
$\mathcal{R}$	reluctance of the circuit	
g	air-gap width	mm
W_f	magnetic field energy storage	J
W_c	co-energy	J
V	voltage	V
R	resistance	Ω
$\mathcal{E}$	induced electromotive force (EMF)	V
ω	motor speed	RPM
η	efficiency of a system	%
P_{in}	input power	W, kW
P_{loss}	total losses	W, kW

P_{cu}	copper loss	W, kW
J	current density	A/m^2
δ	skin depth	m
f	excitation frequency	Hz
σ	electrical conductivity	S/m
ρ_0	resistivity of copper at temperature T_0	Ω·m
ξ	temperature coefficient of resistivity of copper	-
P_{core}	core loss	W
P_v	power by volume	W
$\hat{B}$	peak magnetic flux density	T
α_s, β_s, C_m	Steinmentz fitting coefficients	-
P_h	hysteresis loss	W
P_c	eddy current loss	W
P_e	excess loss	W
K_h	material constant due to hysteresis loss	J/m^3
K_c	material constant due to eddy current loss	J/m^3
K_e	material constant due to excess loss	J/m^3
C_{DC}	coefficient due to DC component in the flux density	-
$C_{thermal}$	thermal capacitance	J/C
Bi	Biot number	-
$\bar{h}$	effective heat transfer coefficient from the surface from all sources	W/m^{2}K
R_{cond}	conduction thermal resistance	K/W
R_{conv}	convective thermal resistance	K/W
R_{rad}	radiative thermal resistance	K/W
$\tau_{thermal}$	thermal time constant	s
m	mass of a body	kg

$R_{thermal}$	thermal resistance	K/W
V_{body}	volume of a body	m^3
k_{radial}	thermal conductivity in the radial direction	W/m^2K
$\bar{h}_{cuboid}$	effective heat transfer coefficient from the surface of the cuboid from all sources	W/m^2K
L_{cuboid}	characteristic length of the cuboid	m
$C_{winding}$	coil thermal capacitance	J/C
$V_{winding}$	volume of the motor coil	m^3
ρ_{Cu}	density of pure copper at 20 °C	kg/ m^3
c_{cu}	specific heat of pure copper at 20 °C	J/(kgK)
C_{MPF}	effective capacitance for the Maximum Packing Factor (MPF)	J/C

Declaration of Academic Achievement

All of the text, figures, and ideas presented in this manuscript were created by Elizabeth Trickett unless explicitly referenced elsewhere or stated otherwise. Any ideas that were not original or were based on academic literature have been properly referenced, to the best knowledge of the author. The only exception to this is where such information is considered basic common knowledge in the field.

The motor design of the 12/16 External Rotor Switched Reluctance Motor, JMAG modelling of its losses, and controller were all created by Brock Howey as detailed in his thesis. Also, the experimental work discussed in section 7.2 and shown in Figure 7-3 was done by Brock. Finally, Brock assisted with the experimental set-up detailed in 6.1.

The software used for the Lumped Parameter Thermal Network (LPTN) analysis was MotorCAD designed by Motor Design Ltd. They assisted with the minor modifications to transition their External Rotor Brushless Permanent Magnet (BPM) template to an External Rotor Switched Reluctance Motor. However, all other modification of the LPTN was performed by Elizabeth Trickett.

Chapter 1

INTRODUCTION

1.1 Background and State-of-the-Art

Today, the drive towards full transportation electrification requires mass commercialization of hybrid and electric vehicles, in addition to other modes of transportation. To achieve this, traction motors are required to be low-cost, reliable, lightweight, high-efficiency, and high-power-density. The electromagnetic, mechanical and thermal design of the motor will determine how able it is to meet these criteria [1]. While the performance of traction motors, in general, is dependent on their electromagnetic and thermal designs it is particularly crucial for motors for in-wheel electric bicycle (e-bike) motors, also known as hub motors. The combination of the demanding operating conditions of a traction motor and the stranded heat that can occur in an external rotor motor can cause a rapid rise in the working temperature in the motor. The higher temperature results in lower efficiency and reduces the working life of the motor, possibly risking operation failure. Thermal management systems can help to alleviate the consequences of high operating temperatures, such asperformance reduction from the controller to avoid thermal breakdown and premature ageing.

For Switched Reluctance Machines (SRM), the thermal rating of the motor is primarily determined by the temperature rating of the magnet wire. Since the SRM has no magnets, the coils and slot liners are often the most vulnerable areas. Evaluating a motor's ability to not exceed its thermal rating requires a knowledge of how well the motor can dissipate heat and the magnitude and distribution of heat it will experience during its standard operation. Often thermal ratings are known for individual components, but not for the whole system. Individual components are chosen so that their lifetime and durability are well within the motor's expected drive-cycle.

Losses determine how quickly the machine will heat up and therefore impact the maximum rating or power output it can produce without failure. For an SRM, some of the most sensitive components to temperature are also part of the structures that produce loss. Losses inside temperature-sensitive parts like coils can pose a problem if they become 'stranded', (i.e. produce a temperature rise locally that cannot be efficiently dissipated). These 'hot spots' can cause localized insulation failure, even if the rest of the motor is well below its thermal limit. Hot spots can be created due to localized high resistance in the copper of the magnet wire or damage to the wire coating. Therefore, the temperature distribution of the motor during operation must be considered to avoid failure, as well as how much heat each component can handle, and how quickly that heat can be transported out of the motor. The lifetime of a motor is directly related to how hot that motor

will get over its lifetime. The importance of managing temperature rise to keep it within the acceptable bounds of the thermal limit of the motor is well known [1][2].

Thermal capacity in motors determines their ability to maintain short term overloads and can affect their ability to persist at peak power operation. Motors are currently sized primarily due to the steady-state thermal performance as opposed to transient, even though for most traction motors they will spend their lifetimes in highly transient duty-cycle operation [3]. However, motor component thermal capacitance causes non-linear thermal performance. Also, component thermal capacitance is difficult to measure and has not been well explored in literature.

Thermal models like Lumped Parameter Thermal Networks (LPTN) predict temperature on a large scale with most components interacting with one another and with the environment [4]. Generating a thermal model begins early in the motor design with modifications continuing as notions of the design and performance get firmer. The process usually involves correcting modelling errors or inaccuracies (determined based on the level of accuracy needed for the study) and updating assumptions related mostly to heat dissipation and tolerances on component properties. For these models to provide the information necessary to allow designs based on the transient thermal performance they would need to be more physically accurate, with transient thermal characteristics based on motor and materials properties. Also, the transient thermal design criteria would need to be formulated in such a way that they could be optimized versus the other

necessary objectives such as, electromagnetic performance, noise, vibration, harshness, cost, volume, and weight.

1.2 Goals and Contributions

The goal of this thesis was to integrate the knowledge from the fields of motor design, heat transfer and materials science to solve heat dissipation challenges in electric machines that no one field could solve alone. One of the main challenges of interdisciplinary work is the identification of challenges that require this approach. This research focuses on identifying and characterizing the areas that such an approach is valid, within the context of the ongoing development of thermal models for electric machines for vehicle applications.

To that end, this work has focused on the areas of greatest thermal challenge in traction switched reluctance motors: the coils. An external rotor motor configuration was selected due to the heat dissipation challenges inherent in the design. The peril of sudden high-temperature rise to coils is an interdisciplinary challenge:

- The coil insulation is vulnerable due to the polymer compound that comprises the insulation,
- The high power density design of the motor translates to more losses with less surface to dissipate heat from, and less thermal capacity to store thermal energy,

- The geometry, composition, and manufacture of the coil component makes it difficult to model thermally – and the transient nature of the problem requires additional care,
- The overall temperature dynamics for the motor are not obvious from a static design and require dynamic simulation of electromagnetic, thermal and sometimes materials design parameters.

The most common problem for rapid temperature rise in coils was studied: motor overload conditions. Traction motors can safely sustain overload conditions for brief periods as part of a drive-cycle if the thermal character of the system is known. Therefore, it was necessary to analyze the thermal dynamics of the overloaded motor before model implementation. Transient thermal characteristics in materials must be combined with the realities of the physical motor design to characterize the temperature rise in a format that is meaningful to the motor application. As a first step, simple characterization tools were developed for coils in slot based on the Lumped Parameter Thermal Networks (LPTN) formalism. One of the difficulties with LPTN formalism is parameter investigation for each element in the network. Until this point, there were no sizing models (known to the author) for determining the number of nodes in the coil in a way that also provided a physical estimate for the capacitance of that node. Without a known capacitance, evaluating the accuracy of the nodes would be guesswork. Without a sizing model, it would be difficult to validate the capacitance in the LPTN

formalism. Both characterization tools are required, and both must be grounded in solid physical understanding.

Therefore, a model of local thermal equilibrium was developed for motor windings based on the materials science concept of nearest neighbours in a regular repeating structure. This is a well-known technique for many physical systems [5]. To complement this, a method of calculating coil capacitance based on the anisotropic winding structure was developed. Called the Maximum Packing Factor (MPF) method it uses the known maximum density of cylinders in a volume to calculate a theoretical lowest bound for the capacitance of a winding system based on machine design parameters. This ‘lowest bound’ can be modified by additional manufacturing if known and if not, it provides the basis for a sound physical sensitivity analysis. Finally, the MPF factor implemented into a commercial LPTN was experimentally validated and a motor capacitance sensitivity analysis was performed. The analysis found that in overload conditions over short periods the motor coil could be modelled adiabatically for hot spot temperature determination. In light of this finding, a brief survey of motor parameters revealed likely transition points where at high currents the motor could or could not be modelled adiabatically.

1.3 Chapter Overview

This dissertation is divided into seven chapters following this one:

Chapter 2: discusses the fundamentals of heat transfer relevant to the thermal analysis of electric machines. Heat transfer problems require a firm foundation of a well-defined problem to make accurate predictions. This chapter introduces the fundamentals of heat flow, defines the heat transfer coefficients necessary for thermal model construction and identifies the dependencies of the heat transfer coefficients on the physical properties of the system and the problem definition.

Chapter 3: discusses the operational characteristics of Switched Reluctance Motors. Torque production is explored as well as the performance dynamics over the operating envelope to get an understanding of the application to which the proposed solution is being applied. Finally, losses are introduced which provide the basis for heat generation in the motor.

Chapter 4: explores the numerical methods used to characterize the motor transient thermal problem – namely Lumped Parameter Thermal Modelling. This chapter investigates the physical basis for the Lumped Volume assumption and relates key heat transfer concepts to motor parameters. Finally, the current methods used in literature for determining heat transfer coefficients for our motor are explored and the dependencies on motor constraints are identified.

Chapter 5: presents the thermal analysis of the 12/16 External Rotor Switched Reluctance Machine under consideration. The expected transient thermal behaviour is discussed in terms of machine construction and operating point and motor coils are identified as a critical component for investigation. A thorough

analysis of winding anisotropy follows and its effects on the calculation of lumped parameter values in RC systems.

Chapter 6: presents the experimental results for the 12/16 External Rotor Switched Reluctance Machine at overload conditions. A method for calculating thermal capacitance based on motor parameters is introduced, implemented into a commercial LPTN and validated.

Chapter 7: analyzes the validated model from Chapter 6 to determine the significance of the characterized capacitance to the system thermal response. The hot spot sensitivity at severe overload conditions to variations in full model capacitance is investigated and key findings for reduced model construction are recorded. Finally, the validated model is investigated at rated operation conditions and the operating envelope is surveyed to determine the conditions that can be considered as ‘severe overloads’.

Chapter 8: summarizes and concludes the findings of this thesis as well as opening the door to future work that can build upon this unique approach

Chapter 2

FUNDAMENTALS OF HEAT TRANSFER

The fundamental equations of thermodynamics are the starting point to solve heat transfer problems. Heat transfer problems are temperature and time-dependent questions found in both engineering problems and every-day concerns, such as: “how long with my tea take to cool to a temperature I want to drink?” Thermodynamics is primarily concerned with the behaviour of matter and the states that matter can occupy. When thermodynamics is applied to a system, it is usually to determine how a driving force or influence will take the system out of one equilibrium state and into another. States are normally defined in terms of these influences; for instance, pressure, temperature, and volume can be used to describe the states of frozen or liquid water (but may also depend on more parameters). Thermodynamics establishes relationships between the equilibrium state (i.e., liquid water) and the resultant change to that state when a property changes (i.e. frozen water when the temperature drops).

Heat transfer problems tend to fall into two categories in engineering: rating problems and sizing problems. Rating problems consist of determining the heat

transfer rate for an existing system at a given temperature difference whereas sizing problems determine what the properties (i.e., like size) of a system must be for a specific heat transfer rate at a given temperature difference [6].

Fig 2-1 illustrates a standard approach to solving a rating problem, the details of which will be explored and expanded upon throughout this chapter. To solve a heat transfer problem, the mechanism of heat transfer and the energy contributions into and out of the system must be defined. Then, the problem must be mathematically formulated through heat transfer's three modes: conduction, convection, and radiation.

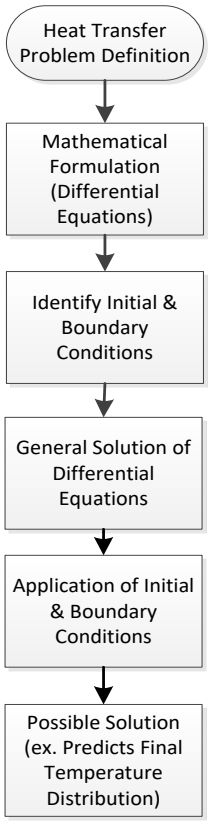

Figure 2-1: A general approach for solving rating heat transfer problems

2.1 Energy Transfer

Heat transfer analysis is a study of the energy transferred as a result of temperature difference; and therefore, concerns itself primarily with 'heat', i.e., thermal energy. Part of the process of heat transfer problem definition includes counting the contributions to a system's total energy - similar to accounting for all forces acting on an object in a free body diagram in Newtonian mechanics. Heat transfer analysis must start as energy transfer analysis. The total energy transfer from all sources is conserved. The mechanism of energy transfer to or from a system can be through heat, work and/or mass flow [7].

The first law of thermodynamics states regardless of the process being undergone by an isolated system that the total energy in that system remains constant. Stated in another way, the transfer of energy into or out of a system by heat, work or mass flow must be balanced against the change in the total energy of that system during the process:

$$\begin{bmatrix} Net\ energy\ transfer\ from \\ heat, work\ and\ mass\ flow \end{bmatrix} = \begin{bmatrix} Changes\ in\ total\ energy \\ i.e., internal, kinetic \\ and\ potential\ energies \end{bmatrix}$$

$$[E_{in} - E_{out}] = [\Delta E_{system}]$$

However, there is no requirement that the energy stays in the same form. For example, although we can correctly assign resistive losses as a 'heat source', these losses did not start as heat – the energy was transformed from

electromagnetic energy to thermal energy. The electromagnetic energy must be accounted for as part of total energy [8]:

$$\begin{bmatrix} Energy\ transfer\ into\ a\ system\ from \\ heat, work\ and\ mass\ flow \end{bmatrix}$$

$$= \begin{bmatrix} Energy\ transfer\ out\ of\ a\ system\ from \\ heat, work\ and\ mass\ flow \end{bmatrix}$$

Heat transfer analysis approaches also stress the need to identify assumptions and simplifications made throughout the procedure in Fig 2-1 and clarify its purpose. Once all sources of energy transfer have been identified, they need to be expressed it in the form of thermal energy, i.e. heat. The amount of heat transferred during a process, Q, measured in Joules, can be expressed as:

$$Q = \int_0^{\Delta t} \dot{Q}\, dt \tag{2-1}$$

Where $\dot{Q}$ represents the heat transfer rate measured in Watts (i.e. J/s). Heat flux is, therefore, the amount of heat transferred per unit time (i.e. $\dot{Q}$) per unit area normal to the direction of heat transfer. Average heat flux, in W/m^2, is, therefore:

$$\dot{q} = \frac{\dot{Q}}{A} \tag{2-2}$$

To account for energy transferred into the system from other sources we can define a rate of heat generation, $\dot{g}$. The rate of heat generation causes a volumetric rise in temperature throughout the medium and thus has units W/m^3. If

$\dot{g}$ varies throughout a volume we can calculate the total rate of heat generation, $\dot{G}$, like this:

$$\dot{G} = \int_V \dot{g} dV \tag{2-3}$$

Using these terms, we can define the rate of change of total energy within a volume in terms of heat transferred into and out of that volume and the energy transformed into heat within that volume:

$$\begin{pmatrix} rate\ of\ change\ of\ the \\ total\ energy\ within\ V_i \end{pmatrix} = \left[\begin{pmatrix} rate\ of\ heat\ transfer\ into \\ V_i \end{pmatrix} - \begin{pmatrix} rate\ of\ transfer\ out\ of \\ V_i \end{pmatrix}\right] + \begin{pmatrix} rate\ of\ heat\ generation \\ within\ V_i \end{pmatrix}$$

$$\left[\dot{Q}_{in} - \dot{Q}_{out}\right] + \dot{g}_i V_i = \frac{\Delta E_i}{\Delta t} \tag{2-4}$$

The first two terms can describe the rate of heat entering or leaving the element from any form of heat transfer [7].

2.2 Conduction

Conduction is the transfer of energy as a result of interactions between more energetic particles and less energetic particles in a medium or media. Fourier's law is a rate equation that describes how heat flows for conduction [7]:

$$\dot{Q}_{conduction} = -kA\frac{dT}{dx} \tag{2-5}$$

Where k is the thermal conductivity, A is the area across which the heat is transferred (always normal to the direction of heat transfer), and $-\frac{dT}{dx}$ indicates that heat will travel in the direction of decreasing temperature. Thermal conductivity has units of W/m^{2}K and is a measure of a material's ability to conduct heat.

Table 2-1: Boundary condition examples for a one-dimensional system

Type	Units	Example Boundary Conditions
Specified temperature	(K)	$T(a,t) = T_a$ $T(a+dx,t) = T_{a+dx}$
Heat flux (specified as a value, or from a heat flux equation such as convection or radiation)	(W/m^2)	$\dot{q}_a = -k\frac{\partial T(a,t)}{\partial x}$ $\dot{q}_{a+dx}$ $= -k\frac{\partial T(a+dx,t)}{\partial x}$

To solve this equation, we need boundary and initial conditions to describe the system. For a unique solution, a differential equation that is second order in space and first-order in time will require two spatial conditions for each dimension and one temporal condition. For a steady-state one dimensional system, we will need boundary conditions like those in table 2-1. We need far more boundary conditions for the Fourier-Biot Equation, however :

$$\frac{\partial^2 T}{\partial x^2} + \frac{\partial^2 T}{\partial y^2} + \frac{\partial^2 T}{\partial z^2} + \frac{\dot{g}}{k} = \frac{1}{\alpha}\frac{\partial T}{\partial t} \tag{2-6}$$

Where α is the thermal diffusivity of the material and proportional to thermal conductivity. A transient, three-dimensional problem like this will require seven pieces of information about the system (six in space, and one in time) while a steady-state one-dimensional problem will require only two (two in space, and since time is now a zeroth-order differential, we no longer need a condition for it). Reducing the number of dimensions, for instance, by using symmetry arguments, is useful to reduce the number of boundary conditions required.

2.3 Convection

Convection is the physical result of combining conduction and fluid motion. Within a solid, heat can only travel as fast as it can diffuse through a material. However, if the medium that heat is propagating through is already in motion, then heat transfer rates from a hot surface can speed up remarkably. Newton's law of cooling can describe the heat transfer rate of convection:

$$\dot{Q}_{convection} = hA_{surface}\left(T_{surface} - T_{ambient}\right) \tag{2-7}$$

Where h is the convection heat transfer coefficient (in W/m^{2}K), $A_{surface}$ is the area of the surface over which convection takes place, $T_{surface}$ is the temperature of that surface and $T_{ambient}$ is the temperature of the flowing medium sufficiently far away as not to be affected by the surface.

2.3.1 Convection Heat Transfer Coefficient

The convection heat transfer coefficient can be defined as the rate of heat transfer between a surface and a fluid (which should be moving) per unit area, per unit temperature difference. All the complexity of local fluid motion, fluid properties, surface geometry, and bulk fluid velocity is captured in this coefficient. Forced convection can achieve h values far higher than natural convection, as can be seen by the values for the convection heat transfer coefficient in table 2-2.

Table 2-2: Value ranges for types of convection[7]

Type of Convection	Value of Convection Heat Transfer Coefficient in $\mathrm{W/m^2C}$
Natural convection of gases	$2-25$
Natural convection of liquids	$10-1000$
Forced convection of gases	$25-250$
Forced convection of liquids	$50-20{,}000$

To determine h for a given geometry and fluid flow we can use computational fluid dynamics (CFD) or measure it experimentally. However, the minimum value of h in a given fluid will be the value for natural convection. Natural convection occurs when fluid moves due to internal buoyancy forces from temperature differences. Natural convection however still has a higher rate of heat transfer than pure conduction would have through the same material since conduction must travel at the speed of diffusion.

2.3.2 Boundary Layers and Dimensionless Numbers

Only moving fluid can take advantage of convective heat transfer rates; stationary fluids must rely on conduction just as a solid would. For heat transfer between a surface and a fluid, both the velocity of the flow and the temperature of the surface affect the heat transfer rate. When a fluid is forced to flow over an impermeable surface, the layer directly adjacent to the surface has zero velocity due to the viscosity of the fluid (with very few exceptions, such as rarefied gases[7]). The second layer away is slowed down by the first layer, and the third is slowed down, although not by as much, by the second layer. This continues until the velocity returns to its 'bulk' velocity value. This velocity profile is known as the velocity boundary layer, and the distance it extends into the fluid is known as the velocity boundary layer thickness, δ. Meanwhile, temperature also forms a boundary layer since a hotter surface conducts heat only to the first layer of cooler fluid. As energy is exchanged between fluid particles further and further from the plate a temperature profile develops known as the thermal boundary layer with its own thermal boundary layer thickness, δ_t. However, the fluid's velocity and temperature profiles are not easily determined analytically, requiring the solution of the Navier-Stokes and energy balance equations, which sometimes do not have analytical solutions for complex geometries. [9] Instead, to characterize the value of the coefficient we can use a series of dimensionless numbers to describe the flow. Table 2-3 shows some of the factors that must be considered when calculating these dimensionless numbers.

Table 2-3: Factors that distinguish flow classifications [7]

Property	Symbol	Fluid	Flow Classification
Dynamic viscosity (a measure of a fluid's resistance to flow)	μ	yes	Viscous vs. Inviscid
Thermal conductivity	k	yes	
Density	ρ	yes	Incompressible vs. Compressible
Specific Heat	c_p	yes	
Fluid Kinematic Viscosity	ν	no	
The geometry of the solid surface		no	Internal vs. External
Type of flow		no	Laminar vs. Turbulent

We can begin to characterize the flow by how much better a fluid flow is at transferring heat than could be transferred due to a non-moving, conduction-only fluid layer:

$$\frac{\dot{q}_{convection}}{\dot{q}_{conduction}} = \frac{h(T_2 - T_1)}{k\frac{\Delta T}{\Delta x}}$$

The only way for $T_2 - T_1 = \Delta T$ is for Δx to be set at the size of the whole fluid layer. We can call this the characteristic length, and denote it L_c. This allows us to define a dimensionless number known as the Nusselt number, Nu:

$$Nu = \frac{hL_c}{k} \tag{2-8}$$

$Nu \underline{=} 1$ where $hL_c = k$ indicates only conduction heat transfer is present. The Nusselt number gives an indication of how much the fluid movement enhances heat transfer, as seen in fig 2-2 a). However, the velocity and temperature profiles also contain the information of the relative thickness of the velocity and thermal boundary layers. This dimensionless number is known as the Prandtl number:

$$Pr = \frac{\mu c_p}{k} \tag{2-9}$$

Where once again μ is the dynamic viscosity and c_p is specific heat. Tab 2-4 gives some common values. The thermal boundary layer will be much thicker than the velocity boundary layer if $Pr \ll 1$ or thinner if $\mathrm{Pr} \gg 1$. Fig 2-2 b) shows the comparison between thermal and velocity boundary layer thicknesses.

Table 2-4: Value ranges for Prandtl number for example fluids

Fluid	Pr
Gases	$0.7 - 1.0$
Water	$1.7 - 13.7$
Oils	$50 - 100{,}0000$

The shape of the velocity profile also influences the heat transfer rate, which occurs with increasing velocity. Perhaps one of the most exciting transitions in convective flow occurs between the highly ordered motion of laminar flow to the highly disordered motion of the turbulent flow. Laminar flow follows an

approximately parabolic velocity profile, as seen in Fig 2-2 c), while turbulent flow exhibits a sharp change in velocity near the surface, followed by a much slower change for the rest of the layer. The transition region exhibits smooth flow broken up by random fluctuations. Fully turbulent flows exhibit both maximum convective heat transfer coefficients as well as maximum friction between the surface and the fluid. The transition between laminar and turbulent flow can be captured by the dimensionless Reynolds number:

$$Re = \frac{VL_c}{\nu} \tag{2-10}$$

Where V is the velocity of the fluid before coming into contact with the surface, and ν is once again the fluid's kinematic viscosity. Large values of Re result in turbulent flow, while small values of Re result in laminar flow.

These three dimensionless numbers allow the characterization of fluid flow without having to solve for its velocity and temperature profiles first. Instead of solving the Navier-Stokes equation, we can define experimental methods in terms of characteristic lengths and the results of those experiments in terms of convection correlations (presented in the form of Reynolds, Prandtl and Nusselt numbers). Given the appropriate selection of geometry and flow characteristics, a convection correlation can be applied to many similar situations.

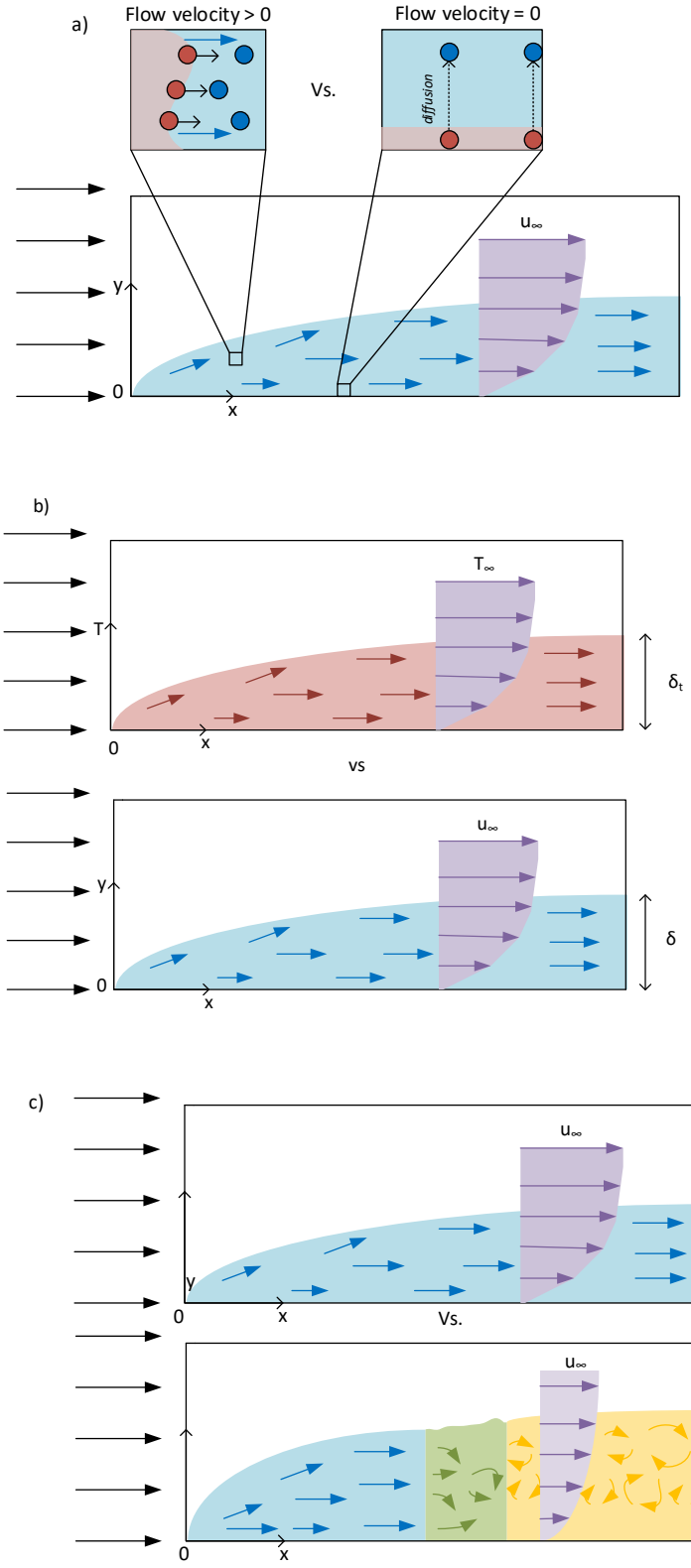
a)
Flow velocity > 0
Vs.
Flow velocity = 0
diffusion
u∞
y
0
x
b)
T∞
T
δt
0
x
vs
u∞
y
δ
0
x
c)
u∞
y
0
x
Vs.
u∞
0
x

Figure 2-2: A comparison between the fluid characteristics considered in the calculation of the a) Nusselt number, b) Prandtl number and c) Reynolds number

2.4 Radiation

Radiation in the field of heat transfer refers to thermal radiation, which is a type of electromagnetic radiation emitted by matter as a result of energy transitions that molecules, atoms and electrons undergo. Matter above absolute zero emits thermal radiation continuously, however the rate of these emissions increases as the temperature of a substance increases. Objects, or bodies, emit thermal radiation throughout the electromagnetic spectrum with the wavelength of that light determined by the temperature of the body (between about 0.1 to 100μm). Most objects around room temperature fall into the area of the electromagnetic spectrum called the infrared region (0.76 to 100 μm), while objects hotter than 800K can begin emitting noticeable light in the visible region (0.4-0.76 μm).

Radiation is a fundamentally different heat transfer mechanism than conduction or convection since it relies solely on the transfer of energy by photons. The constituent parts (atoms, electrons and molecules) of all matter can participate in radiation emission, absorption and transmission, meaning that its a volumetric phenomenon. However, for most non-transparent (i.e. opaque) solids like the kind, we will be dealing with only the activity along the surface meaningfully interacts with other objects. Therefore, we can assume for most objects in motor radiation is a surface phenomenon. From this perspective, radiation is emitted at every point along its surface in all directions and can propagate both through media or vacuum. For radiation heat transfer, energy does not only transfer from

a high-temperature area to a low-temperature area (as occurs for conducting media). Instead, both hotter and colder objects transfer energy. It is the *net* energy transfer that occurs from hotter to cooler objects.

2.4.1 Blackbody Radiation and the Stephen-Boltzmann Law

A blackbody is an object that emits blackbody radiation. Blackbody radiation is the spectrum we observe when the maximum rate of radiation is emitted from a surface at a specified temperature. However, objects at different emissivities will emit different amounts of radiation per unit surface area, even at the same temperature. A blackbody can also be described as any object with an emissivity of 1, which can be used as a standard since all other objects will have a lower emissivity. Therefore, emissivity can be defined as the emission of an object divided by the emission of a blackbody at the same temperature as the object. The emissivity depends on the makeup of the material, the object's temperature and the photon energy (ε_γ), and determines what fraction an object emits at when compared to a blackbody at the same temperature:

$$\epsilon_{rad} = \epsilon_{rad}(T, \varepsilon_\gamma) \;\; 0 \leq \epsilon_{rad} \leq 1$$

Blackbodies are also perfect absorbers; they absorb all incident radiation. Absorptivity measures how like a blackbody an object is when absorbing incident radiation, also as a fraction between 0 and 1, where 1 is 'absorbs as a blackbody':

$$\alpha_{rad} = \alpha_{rad}(T, \varepsilon_\gamma) \;\; 0 \leq \alpha_{rad} \leq 1$$

Emissivity and absorptivity can be thought of how reflective a surface is, i.e. a measure of how much incident radiation is absorbed by the object and how much is reflected. The composition of the blackbody does not affect its behaviour as a perfect emitter and absorber. Kirchoff's law of radiation equates emissivity and absorptivity for a given temperature and wavelength of light. If we take this over the entire spectrum, that means the total hemispherical radiation emitted by a body must be equal to the hemispherical radiation absorbed by it for a given temperature. While extremely convenient for calculation, Kirchoff's law begs the question of why does $\alpha_{rad}(T) = \epsilon_{rad}(T)$, not just for blackbodies but for all objects?

Assume we have an ensemble of photons at t_0 inside a rigid oven that is insulated from the rest of the Universe. The energy and volume of the combined photon + oven system are constant, i.e. *dE*=*dV*=0. If we assume the oven starts at T_0 and has an emissivity close to 1, then we would expect it to emit and absorb photons like a blackbody. In a physical system like air in a balloon, we can expect the number of air molecules in the balloon to remain constant. Thermodynamic equilibrium is reached when the temperature is no longer changing, i.e. there are no gradients. In this case, the energy has been distributed among the participating ensemble, i.e. the air molecules. Unlike the air in the balloon, we cannot expect the number of photons in the oven to remain constant in the period studied since photons can be absorbed. We can examine the spectrum of the photon ensemble within the oven – that is, the distribution of

wavelengths of all the photons – and find that it does not depend on the nature of the oven. Shape, surface roughness, shininess, and colour do not impact the spectrum. Therefore when in thermal equilibrium, the intensity of light radiated from an object (aka, emitted) must be identical to the intensity of light absorbed by the object for all photon energies and wavelengths. For a system in thermodynamic equilibrium, every process (e.g. matter absorbing a photon) occurs at the same rate as its inverse process (e.g. matter emitting a photon) such that there is no net flow of energy or matter [10]. Thus, emissivity and absorptivity must be identical at each wavelength, which is correlated with a well-defined temperature. Therefore, different temperatures will involve different wavelength spectra [11].

How does temperature relate to spectra? The Stephan-Boltzman law describes the radiation energy emitted by a blackbody per unit time, per unit surface area:

$$E_b(T) = \sigma_{rad} T^{\ 4} \tag{2-11}$$

Where E_b is the blackbody total emissive power, σ_{rad} is the Stephan-Boltzman constant. and T is the temperature of the emitting surface. E_b is measured in W/m^2. A blackbody is assumed to emit at uniform intensity in every direction, i.e. it is a diffuse emitter. The total blackbody emissive power is, therefore, the total radiation emitted over all wavelengths in all directions. A spectrum, however, considers each wavelength separately.

2.4.2 Radiation Flux and Radiation Intensity

Radiation is emitted by all objects at a temperature greater than absolute zero, along with all parts of its surface (quantized into planar elements) in all directions. So far, we have examined ideal blackbodies radiating in thermal equilibrium, which have uniform emission in all directions. If this were true of all objects, then emissive power would be enough to sufficiently quantify radiation. However, real objects can have directionally non-uniform emission. Heat transfer occurs between radiating bodies of different temperatures due to the net difference in their emissions. While net differences can sometimes remain scalar quantities, often, we require vector and higher-order directional quantities to better understand the system dynamics. Radiation intensity is a directional quantity that describes the magnitude of radiation “coming from” a specific direction in space. Radiation passing through a point could come from emitted or incident (i.e. redirected) radiation.

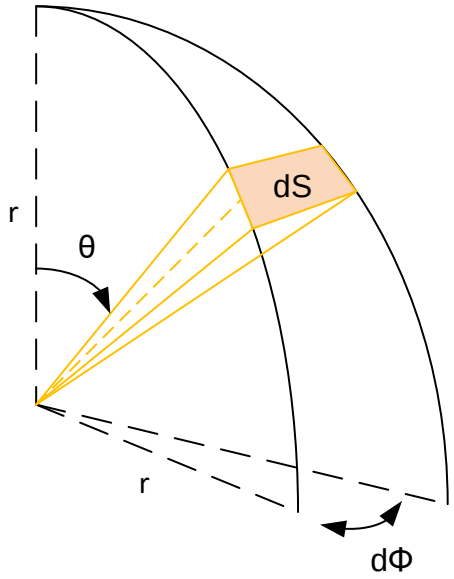

Figure 2-3: A solid angle describing radiation intensity of light

On a bright day, a car passing by could briefly dazzle our eyes with a flash of brilliant sunlight. The radiation did not originate at the car – it was instead redirected from its origin at the sun. At that moment, our field of view mattered as the car surface lined up with both the sun (or another reflective surface) and our eyes. The measure of field-of-view with respect to direction is known as a solid angle, and it can be thought of as the size of an opening in space. A solid angle is similar to the three-dimensional equivalent of a plane angle. If we can describe an arc by the angle, it sweeps out at the center of a circle; then, we can do the same for the area on a hemisphere by specifying zenith, θ, and azimuthal angles, ϕ. The region described in this fashion, shown in Fig 2-3, is the solid

angle, denoted by Ω and measured in steradians (sr). A differential surface area, dS_{rad}, or a sphere of radius r subtends the differential solid angle:

$$d\Omega = \frac{dS_{rad}}{r^2} = \sin\theta \, d\theta d\phi \tag{2-12}$$

If we stand at the center of the sphere, then the area dS is, of course, normal to our direction of view. If we consider a radiating differential area, dA, at the center of the sphere, then θ is measured from the direction normal to dA. Radiation is emitted in all directions from dA into this hemispherical space. As we change θ, an observer on the surface dS_{rad} would see a changing 'effective area' of dA. This effective area would be at its maximum when dS_{rad} is directly above dA ($\theta = 0$) and a minimum when dS_{rad} is at the horizon ($\theta = 90$):

$$effective\ area\ of\ dA\ seen\ by\ dS_{rad} = dA\ \cos\theta$$

Emitted Radiation, Incident Radiation and Total Radiation

Radiation intensity for the total (i.e. over all wavelengths) emitted radiation, I_e, in the direction of view (θ, ϕ) is therefore defined as:

$$I_e(\theta, \phi) = \frac{d\dot{Q}_e}{dA\ \cos\theta \, d\Omega} = \frac{d\dot{Q}_e}{dA\ \cos\theta \sin\theta \, d\theta d\phi} \tag{2-13}$$

Where $d\dot{Q}_e$ is the rate at which radiation energy is emitted over all wavelengths, and I_e is measured in W/m^2 sr. The denominator is the solid angle modified by the effective area, which is a projection of the actual area. This factor allows us to translate between quantities that relate to the actual area, and the ones that

relate to the 'direction of view' and thus, the effective area. Consider the relation of radiation intensity (directional) to emissive power (non-directional), i.e. the rate at which radiation energy is emitted from a surface, per unit area over all wavelengths:

$$dE_{rad} = \frac{d\dot{Q}_e}{dA} = I_e(\theta, \phi) \cos\theta \sin\theta \, d\theta d\phi \tag{2-14}$$

Emissive power is the radiation flux for emitted radiation, measured in W/m^2. Of course, surfaces do not just emit radiation, but they absorb or reflect it as well. If radiation is incident on a surface (whether because of the emission or reflection of another radiation source), then we can also use this factor to describe the intensity of incident radiation, I_i:

$$G_{rad} = \int_{hemisphere} dG_{rad} = I_i(\theta, \phi) \cos\theta \sin\theta \, d\theta d\phi \tag{2-15}$$

Where G is just the radiative flux of the incident radiation in W/m^2. If the incident radiation is diffuse (that is, the radiation incident on a surface from all directions is uniform) then we can integrate over the entire hemisphere:

$$G_{rad} = \int_{\phi=0}^{2\pi} \int_{\theta=0}^{\pi/2} I_i(\theta, \phi) \cos\theta \sin\theta \, d\theta d\phi = \pi I_i \tag{2-16}$$

Similarly, a diffusely emitting surface (like a blackbody) will be:

$$E_{rad} = \int_{\phi=0}^{2\pi} \int_{\theta=0}^{\pi/2} I_e(\theta, \phi) \cos\theta \sin\theta \, d\theta d\phi = \pi I_e \tag{2-17}$$

In the case of a blackbody, all the incident radiation will be absorbed, and all the radiation leaving the object will be diffuse emission. However, for an object with an emissivity not equal to one, some of the radiation that leaves the surface of an object will be reflected irradiation, in addition to its emission, as seen in Fig 2-4. The total radiation flux leaving a unit area of surface regardless of origin is known as radiosity, J, and measured in W/m^2:

$$J_{rad} = \int_{hemisphere} dJ_{rad} = I_{e+r}(\theta, \phi) \cos\theta \sin\theta \, d\theta d\phi \tag{2-18}$$

So far, equations 16, 17 and 18 have considered quantities integrated over all wavelengths. However, in truth it is a spectrum of wavelengths that are emitted, reflected and absorbed at each temperature. Radiation intensity can be further specified when considering the spectral radiative intensity I_λ, where again spectral refers to varying with wavelength, λ_{rad}.

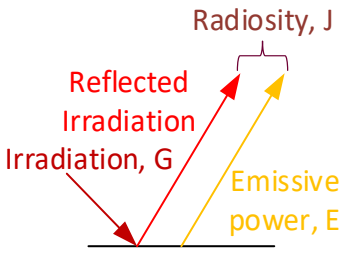

Figure 2-4: Total radiation leaving a surface with $\epsilon \neq 1$

Spectral Radiative Intensity

Radiation intensity can be further specified when considering the spectral radiative intensity I_λ, where again spectral refers to varying with wavelength. I_λ is the rate at which radiation energy is emitted, per unit solid angle, Ω, per unit area dA normal to the direction (θ, ϕ) for a wavelength between λ_{rad} and $\lambda_{rad} + d\lambda_{rad}$:

$$I_\lambda(\theta, \phi, \lambda_{rad}) = \frac{d\dot{Q}_e}{dA \cos\theta \sin\theta \, d\theta d\phi d\lambda_{rad}} \tag{2-19}$$

Spectral radiative intensity, sometimes known as specific intensity, has units of $\mathrm{W/m^2 \cdot sr \cdot \mu m}$, where $\mu\mathrm{m}$ is the measure of per unit wavelength interval. However, care must be taken since sometimes the units are written as $\mathrm{W}/m^3 \cdot \mathrm{sr}$. Emitted radiation, incident radiation and total radiation can all be expressed as spectral quantities. By considering the spectral and directional (which will be denoted by a subscript θ) qualities of radiation intensity, cumulative effects can be tallied:

$$Change\ in\ radiative\ energy$$
$$= +Gain\ due\ to\ emission - Loss\ due\ to\ absorption$$
$$-Loss\ due\ to\ outscattering + Gain\ due\ to\ inscattering$$

Scattering is any phenomenon that causes light to change its direction, such as reflection or transmission. As a light ray, i.e. radiative energy, travels it will lose strength due to scattering and absorption from matter in random directions.

However, some of that scattering and emission in the direction (along its path) will strengthen the light ray. For this direction and path, a Radiative Transfer Equation (RTE) in terms of I_λ can be determined. However, this is incredibly difficult given the complication that is inherent with real surfaces. Properties like emissivity, absorptivity, reflectivity and transmissivity in practice do vary with wavelength and direction, at least for some materials. A blackbody is a convenient reference; however, it is an ideal body. To consider the effect of radiation exchange between surfaces (of varying materials and number), it is helpful to introduce simplifying assumptions where applicable. Going forward, spectral quantities (i.e. varying with wavelength) will be denoted by a subscript λ, and directional quantities (varying with (θ, ϕ)) will be denoted by a subscript θ.

2.4.3 View Factor and Radiation Exchange Between Surfaces

For some problems, surfaces can be assumed as gray, diffuse and opaque, and we can use a much simpler formalism for describing the radiation exchange between two radiating bodies. A grey surface is one in which we can expect the emissivity to be constant for the wavelengths of radiation considered ($\epsilon_\lambda = constant$). ϵ_λ changes quite dramatically with wavelength for some materials, while others remain relatively constant.

Diffuse emitters obey $\epsilon_\theta = constant$. It is common in radiation analysis to assume surfaces have emissivities equal to their value in the normal direction ($\theta = 0$). Materials that are electrical conductors tend to have an emissivity value close to

$\theta = 0$ until the view angle exceeds $\theta = 40$, while non-conductors have an emissivity close to $\theta = 0$ until the view angle exceeds to $\theta = 70$. Polished metal is an example of a specular surface. To complicate matters, emissivity can also vary with the temperature of the surface. However, emissivity tends to be relatively constant for materials at temperatures below 260°C [12].

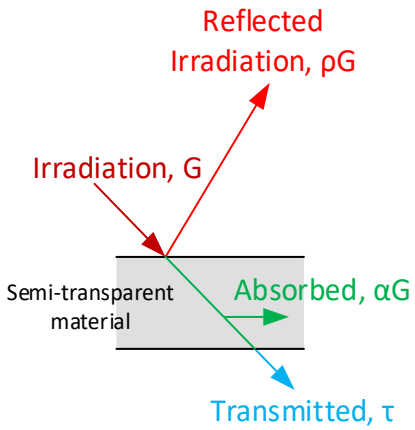

Figure 2-5: Media with a non-zero transmissivity, $1 \geq \tau > 0$

An opaque surface is one in which we can assume only the surface of the body participates in heat transfer. Transparent media, on the other hand, need to consider radiation heat transfer as a volumetric phenomenon [12]. As opacity increases, the amount of photons that can reach the surface diminishes, until some limit where only photons generated at the surface of a medium can escape. Opaque media only need to consider the effect of incident radiation in terms of reflection and absorption; however transparent media also need to consider the value of transmissivity, τ_{rad}, as seen in Fig 2-5. For opaque media $\tau = 0$.

Recall the total radiation leaving a surface is the sum of the emissive and reflected irradiation. For opaque surfaces, incident radiation is either absorbed or reflected. Reflectivity, ρ_{rad}, determines the fraction of the incident radiation that is reflected by the surface, and thus not absorbed:

$$\alpha_{rad} + \rho_{rad} = 1 \tag{2-20}$$

Reflectivity greatly complicates calculations since it requires bidirectional data, i.e. not only the angle of incidence of the incoming light ray but also the angle of the reflected ray(s). In practice to simplify, surfaces are considered either specular or diffuse, eliminating the need for bidirectional data. Specular surfaces reflect light at the same angle as the incident radiation, as seen in Fig 2-6 a), requiring only one piece of directional data. Diffuse surfaces redirect incident light in all directions, as seen in Fig 2-6 b), requiring no directional data. Thus, equations derived assuming diffuse surfaces and are not valid for specular surfaces.

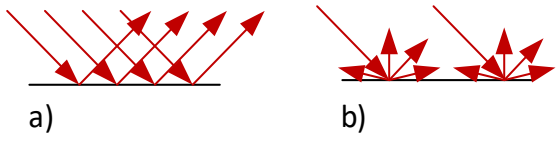

Figure 2-6: a) Intensity from specular surfaces varies with direction while b) Diffuse surfaces are equal in all directions [13]

View Factor

For surfaces that can be approximated as gray, diffuse and opaque, radiation exchange between surfaces becomes dependent only on their temperature, how

they view one another (i.e. what line-of-sight they may have between each other), and a constant value for emissivity. For instance, for a warm hand being waved in front of a cast-iron pan, we can describe $\dot{Q}_{radiation}$ (measured in W) from the surface of the hand to ambient via the Stephan-Boltzman equation:

$$\dot{Q}_{radiation} = \epsilon_{rad}\sigma_{rad}A_{surface}\left({T_{surface}}^4 - {T_{surroundings}}^4\right) \qquad (2\text{-}21)$$

Where ϵ_{rad} is the emissivity of the surface, σ_{rad} is the Stephan-Boltzman constant. $A_{surface}$ and $T_{surface}$ is the area and temperature of the emitting surface, respectively. $T_{surroundings}$ is the temperature of ambient, considered the hemispherical free space around the surface. To describe radiation exchange between surfaces (for instance the plane surfaces for hand-cast iron radiation heat transfer), a factor can be introduced to modify equation 2-21, known as angle factors, $F_{1\,2}$, or view factors [12]. Angle factors are algebraic relations for several geometric configurations that define the fraction of radiant energy, leaving one surface which impinges on another. For two elements separated by distance *r*:

$$F_{1\,2} = \frac{1}{A_1}\iint_{A_1\,A_2}\frac{\cos\beta_1\cos\beta_2}{\pi r^2}\,dA_1 dA_2 \qquad (2\text{-}22)$$

Where, β_1 and β_2 are the angles away from the normal direction for each face, as illustrated in Fig 2-7. The Stefan-Boltzmann equation can be modified as follows, for the net rate at which radiation is emitted from a surface with area A_1 to be absorbed by a surface with area A_2:

$$\dot{Q}_{1\,2} = A_1\,\sigma_{rad}\,F_{1\,2}\,\epsilon(T_1^4 - T_2^4) \tag{2-23}$$

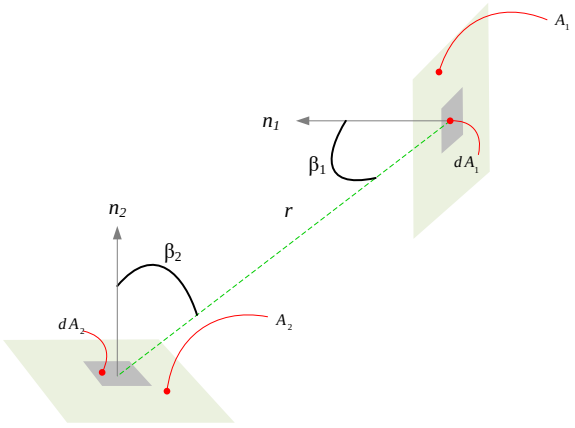

Figure 2-7:Illustration of angle factor between two surfaces.

Catalogues of view factors exist in the literature [12], [14]. For instance, radiation between a pair of concentric, similar surfaces, such as between the rotor and the stator, where:

$$q_{12} = \frac{\epsilon_1 A_1\,\sigma_{rad}\,(T_1^4 - T_2^4)}{1 + \epsilon_1\left({}^{A_1}/_{A_2}\right)\left[\left({}^{1}/_{\epsilon_2}\right) - 1\right]} \tag{2-24}$$

Or for parallel flat plates, while separated by a small distance, the equation would be:

$$q_{12} = \frac{A_{1-2}\sigma_{rad}(T_1^4 - T_2^4)}{{}^{1}/_{\epsilon_1} + {}^{1}/_{\epsilon_2} - 1} \tag{2-25}$$

Many finite element and lumped parameter models use algebraic variations of this formalism to simplify calculations. At low temperatures, the gray, diffuse and opaque assumption tends to be acceptable since the fourth power dependency of

emissive power causes radiation to be one of the weaker forms of heat transfer in and around room temperature [15].

Chapter 3

FUNDAMENTALS OF SWITCHED RELUCTANCE MACHINES

Switched reluctance motors operate based on fundamentally different principles than most conventional motors, such as permanent magnet or induction machines. Most motors function by creating torque due to the mutual interaction of magnetic fields. In contrast, switched reluctance motors (SRM) operate producing co-energy torque. Due to the saliency of rotor and stator teeth, changes occur in the magnetic circuit as the rotor rotates. During rotation, a rotor tooth will align and un-align with stator teeth. A switched reluctance motor is composed primarily of magnet wire wound into coils and electrical steel (or magnet steel) laminations. There are no permanent magnets, as seen in Fig 3-1.

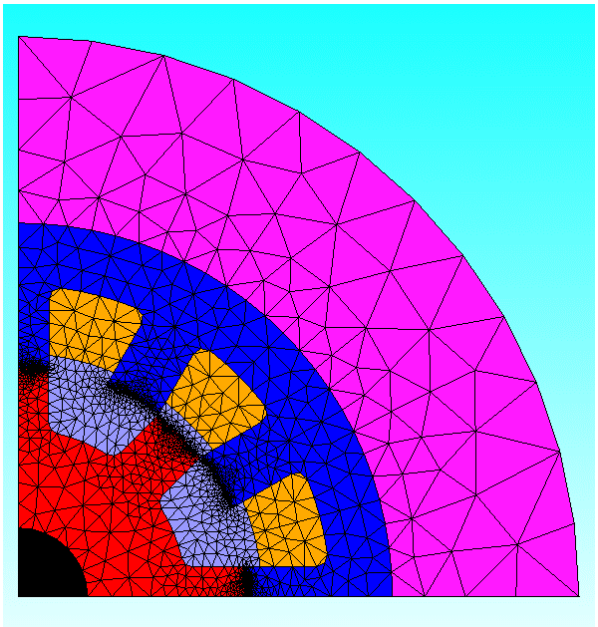

Figure 3-1: A fractional model of a 12/8 SRM where the red component is the rotor, the yellow are the coils, the blue is the stator and the purple is the housing [from JMAG]

In this chapter, we will explore the fundamentals of how SRMs operate and how that operation causes excess heat in the form of losses. We begin with the basics of how torque is produced in an SRM, followed by how we can maximize that torque. We will then examine the complications that arise in our attempt to control torque and finally the consequences of torque production: losses.

3.1 How Do We Produce Torque?

Torque is produced in an SRM when inductance changes in time. When an electric current flows through a coil, it causes changes in the magnetic circuit attached to that coil. The characteristics of that magnetic circuit, as well as the coil, can be described by the inductance, L.

In addition, due to the saliency on both the rotor and the stator, the inductance profile will also change with the effective shape of the airgap. This means rotor position, θ, is also a factor in producing torque [16]:

$$\tau = \frac{1}{2} i^2 \frac{\partial L(\theta)}{\partial \theta} \tag{3-1}$$

In a motor, for a non-saturated phase, inductance can be described by its relationship between flux-linkage and current:

$$\lambda = L(\theta) i \tag{3-2}$$

To describe the torque production dynamics of an SRM you need at the minimum information about the rotor position, current and inductance, or flux-linkage profiles. These dependencies are non-trivial and non-linear. Let's break all that down.

3.1.1 What is Electrical Angle and Rotor Position?

θ is known as the electrical angle and indicates the rotor position, for the overall electrical cycle. One electrical cycle is defined as the time it takes for a rotor pole to move from the unaligned position to the next unaligned position. Due to the symmetry of the machine, stator poles belonging to the same phase will be on the same electrical cycle.

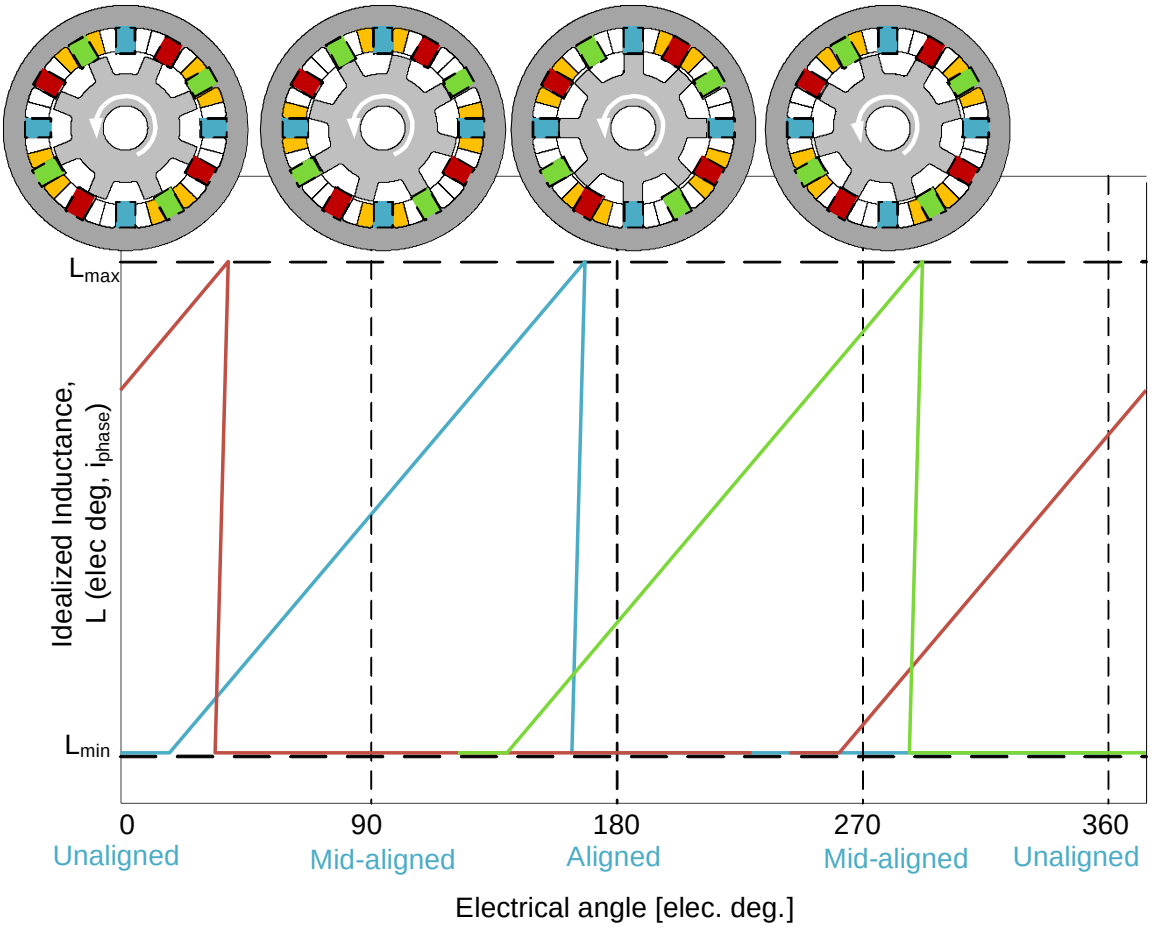

Figure 3-2: Idealized inductance versus rotor position by excited phase

Fig 3-2 shows the idealized inductance for three phases, along with a schematic showing the relative position of the rotor in the electric cycle for the blue phase. The yellow coils show which phase has been excited at each step. Continuous torque is produced by multiple phases acting in concert; each triggering sequentially when the preceding phase finishes its torque pulse. In other words, a rotor pole will be at the same relative position for each stator pole of the same phase. The total number of torque pulses or strokes, S, for one mechanical revolution, θ_{mech}, will be:

$$S = N_R m \tag{3-3}$$

Where m is the number of phases and N_R is the number of rotor poles. We can, therefore, define the electrical angle:

$$\theta_{elec} = N_R \theta_{mech} \tag{3-4}$$

3.1.2 What is a Magnetic Circuit?

The magnetic field inside a ferromagnetic material is known as the magnetic flux density, $\boldsymbol{B}$, while the external applied magnetic field is known as the magnetic field intensity, $\boldsymbol{H}$. Flux density is measured in units of tesla (T), while field intensity is measured in units of Ampere per meter (A/m). Within a material, the change in magnetic flux density can be described in relation to the relative permeability of the material, μ_r, to the permeability of free space, μ_0.

$$\boldsymbol{B} = \mu_r \mu_o \boldsymbol{H} \tag{3-5}$$

Magnetic flux prefers to flow through high magnetic permeability material. Lamination steel has much higher permeability than air, making travelling through steel the preferred route, as seen in Fig 3-4 a). In the absence of a ferromagnetic core material, magnetic flux lines form closed loops that diverge as they get farther from the magnetic source, as seen in Fig 3-4 b). The distance between flux lines denotes the relative intensity of the magnetic field. While flux is concentrated in the center of the solenoid, the flux quickly diverges outside of the

core, such that the region shaded ‘a’ is four times the flux density of region ‘b’. Without the core of the solenoid, the behaviour of the magnetic field lines must be expressed with vector calculus. However, with a core, we have the opportunity ton simplify our description of the behaviour of flux.

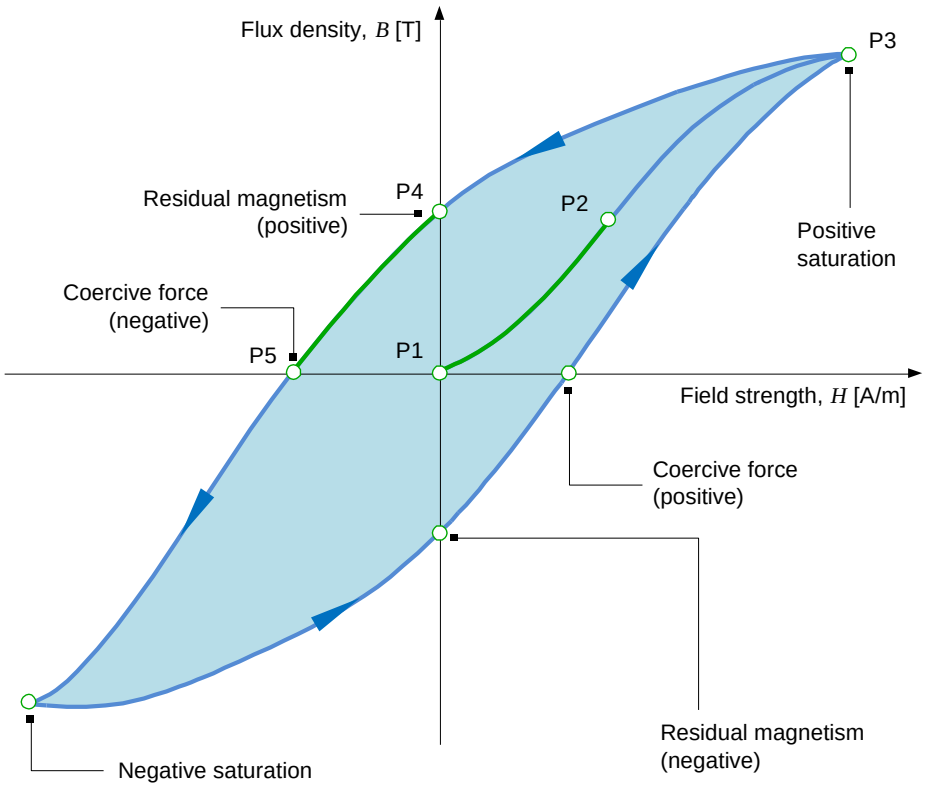

Figure 3-3: B-H curve [16]

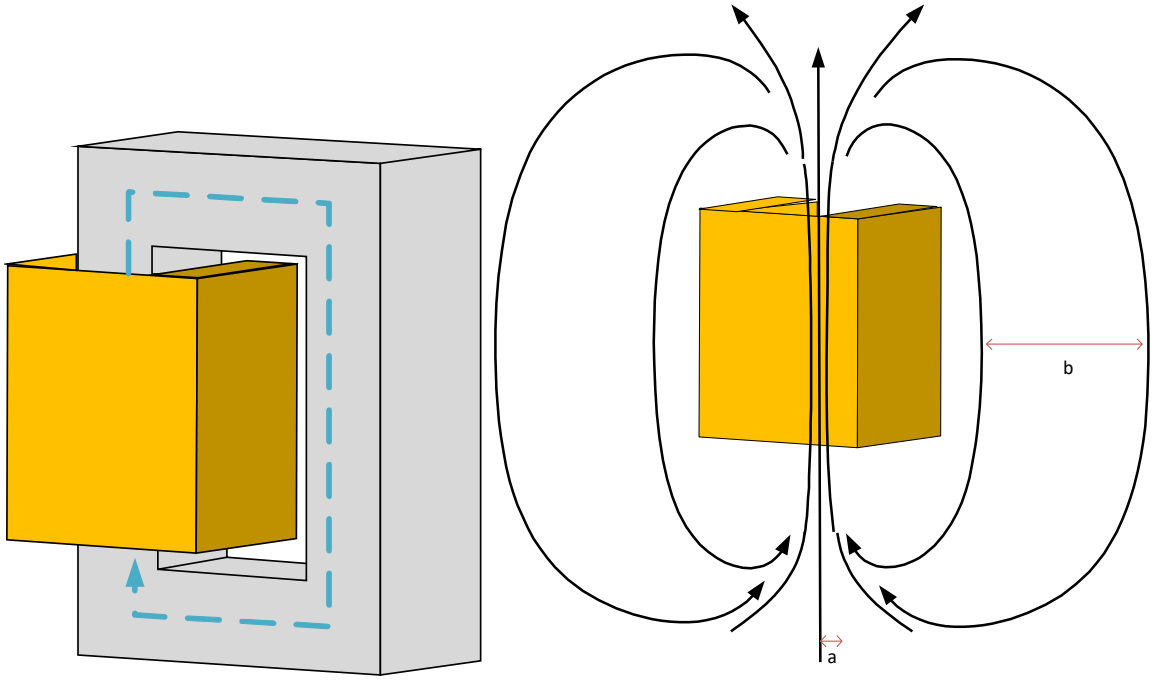

Figure 3-4: Flux path produced by a) a cored solenoid and b) a coreless solenoid

Within a ferromagnetic material like iron, the closed lines that make up the flux can be guided into a smaller cross-sectional area. We can define flux Φ, in Wb, based on the magnetic flux density through a given area, A:

$$\Phi = \boldsymbol{B}A \tag{3-6}$$

The flux in a magnetic circuit is analogous to current in an electric circuit; it is closed-loop that flows (mostly) through a 'conductive' (i.e. ferromagnetic) material. Following the electric circuit analogy, therefore we can define a magnetic circuit as:

$$\Phi = \frac{Ni}{\mathcal{R}} \tag{3-7}$$

Where N is the number of turns of the coil in the circuit, Ni is the magnetomotive force which describes the potential that 'induces' the flux to flow, and $\mathcal{R}$ is the reluctance of the circuit. Reluctance can be defined as:

$$\mathcal{R} = \frac{l}{\mu_r \mu_o A} \tag{3-8}$$

Where A is the cross-sectional area of the lamination steel, and l is the length of the magnetic flux path. As you would expect, it acts as a resistance to a magnetic field, for instance with the air-gap functioning as a rather large resistor. Even when the air-gap between steel is very small in comparison to the rest of the circuit, it dominates the reluctance contribution to the circuit. Specifically, the reluctance over the air-gap, g, (assuming the relative permeability of air is 1) is:

$$\mathcal{R}_g = \frac{g}{\mu_o A} \tag{3-9}$$

3.1.3 Flux-Linkage-Current Dependency

Flux-linkage describes the amount of flux 'linked' to a magnetic circuit, or in other words, the total magnetic flux, Φ, through the N-turn coil:

$$\lambda = N\,\Phi \tag{3-10}$$

Flux linkage (in units of Wb-turns) is dependant on the current and relative position of the rotor and stator, making the flux-linkage behaviour highly non-linear. Given this relationship, as well as equations 3-6 and 3-2 you may guess that inductance can be described in terms of material properties and magnetic

circuit properties. This is true, and for a simple ferromagnetic material inductance can be described as:

$$L = N^2 \mu_r \mu_o \frac{A}{l} \tag{3-11}$$

However, for a motor equation, 3-11 is too simple to be used. Instead, we need to be able to describe flux-linkage in terms of current and rotor position. We can do this with a flux-linkage current diagram, as seen in Fig 3-5. We see that flux-linkage also doesn't increase linearly with current which is due to the magnetic character of the circuit. We can see that the magnetization curve mimics the B-H curve in Fig 3-3. Given the flux-linkage-current diagram, inductance is just the slope of the curve.

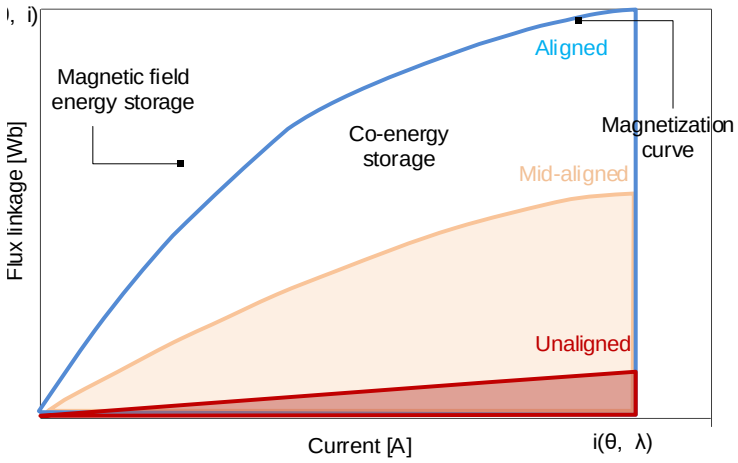

Figure 3-5: Flux-linkage vs current for various rotor positions [17]

As alluded to before, the rotor position matters because it changes the effective air gap length in the magnetic circuit as the motor rotates. Changing the effective air gap length causes a variation in the flux-linkage, as seen in Fig 3-5.

To determine the energy stored in the magnetic field, we can consider the non-physical quantity of co-energy. If work is a force applied to move an object a certain distance, Fdx, then co-energy is xdF – still in units of joules, but now we can imagine it describes the energy as if we fixed displacement and changed the force instead. This quantity is useful in describing systems that store energy.

For our SRM system, the magnetic field acts as a storage medium, bridging the electromagnetic energy conversion. Returning to Fig 3-4, the area above each magnetization curve is the energy stored in the magnetic field. However, the area we are most interested in is the area under the magnetization curve. This is the co-energy storage, and it is essential to calculating the torque produced by an SRM. Given an input of electrical energy into the system, some will be lost due to resistance in the coils, and the rest will be stored in the magnetic field, W_f or translated to mechanical energy*:*

$$dW_f(\lambda,\theta) + \tau d\theta = id\lambda \tag{3-12}$$

Therefore, torque and current can be isolated by holding either rotor position or flux linkage constant.

$$\tau = -\frac{\partial W_f}{\partial \theta}, at\ constant\ \lambda \tag{3-13}$$

$$i = \frac{\partial W_f}{\partial \lambda}, at\ constant\ \theta$$

W_f is difficult to attain, however. On the other hand, Co-energy, W_c, is just the bottom half of the flux linkage- current diagram and can, therefore, be defined as:

$$W_c = \lambda i - W_f(\lambda, \theta) \tag{3-14}$$

And thus, we can define torque in terms of co-energy:

$$\tau = \frac{\partial W_c}{\partial \theta}, at\ constant\ i \tag{3-15}$$

$$\lambda = \frac{\partial W_c}{\partial i}, at\ constant\ \theta$$

Thus, at a given current level we can calculate the torque based on where we are in the electrical cycle.

3.2 Maximizing Torque Production and Power Factor

To maximize the torque production available to us for a given machine geometry we need to maximize the difference between the aligned and unaligned flux linkage. At small currents, a SRM will work in the linear region of the magnetization curve and can be modelled using analytical expressions. In this region, less than half of the total magnetic energy supplied to the machine is converted to mechanical work, achieving a low power factor. In the non-linear region of the magnetization curve, an SRM can take advantage of the increased area under the non-linear region of the curve. This allows can achieve a much higher power factor and thus a much better utilization of the energy conversion process. Based on Fig 3-5 we can see the maximum flux linkage occurs in the non-linear region of the magnetization curve and at high current.

For any given current the energy available to be converted increases with rotor position approaching fully aligned, however, there is an upper limit. The

reluctance of the magnetic circuit increases as we saturate the electrical steel, in addition to changing with the position. Saturation is when the top of the B-H curve becomes almost horizontal. The air gap reluctance is highest when the rest of the circuit is saturated, at any given position. As we apply current, magnetic moments in the steel align to the external magnetic field. These contributions add up together, giving the B-H curve its shape. However, eventually, it becomes harder and harder to align the moments, gaining only an incremental increase with current increase [18].

Due to the nonlinear nature of the SRM, operational characteristics need to be analyzed using FEA software. Fig 3-6 shows a constant current excitation for a 12/8 SRM, using electromagnetic FEA software. Flux linkage is shown as it varies over one electric cycle (i.e. varying with rotor position) for several current levels. The shape of each curve shows the general character of how the rotor position affects the flux linkage. As phase current is increased, the flux linkage is also increased, however with diminishing returns as the magnetic core saturates. For instance, the difference between the two topmost flux linkage curve in Figure 3-6 is 50A, yet flux linkage changes less than going from 2.5 A to 5A.

Putting this all together, the position of the rotor will change the size of the effective air gap and therefore change the magnetic circuit. As the reluctance reduces from unaligned, to partially aligned and towards the aligned position, torque is produced. Flux linkage is minimized when the rotor is in the unaligned position, and when the stator pole is not likely to be saturated. In the aligned

position, flux linkage is maximized, and the stator pole is more likely to saturate. When the laminated steel core is saturated, the torque production capability increases.

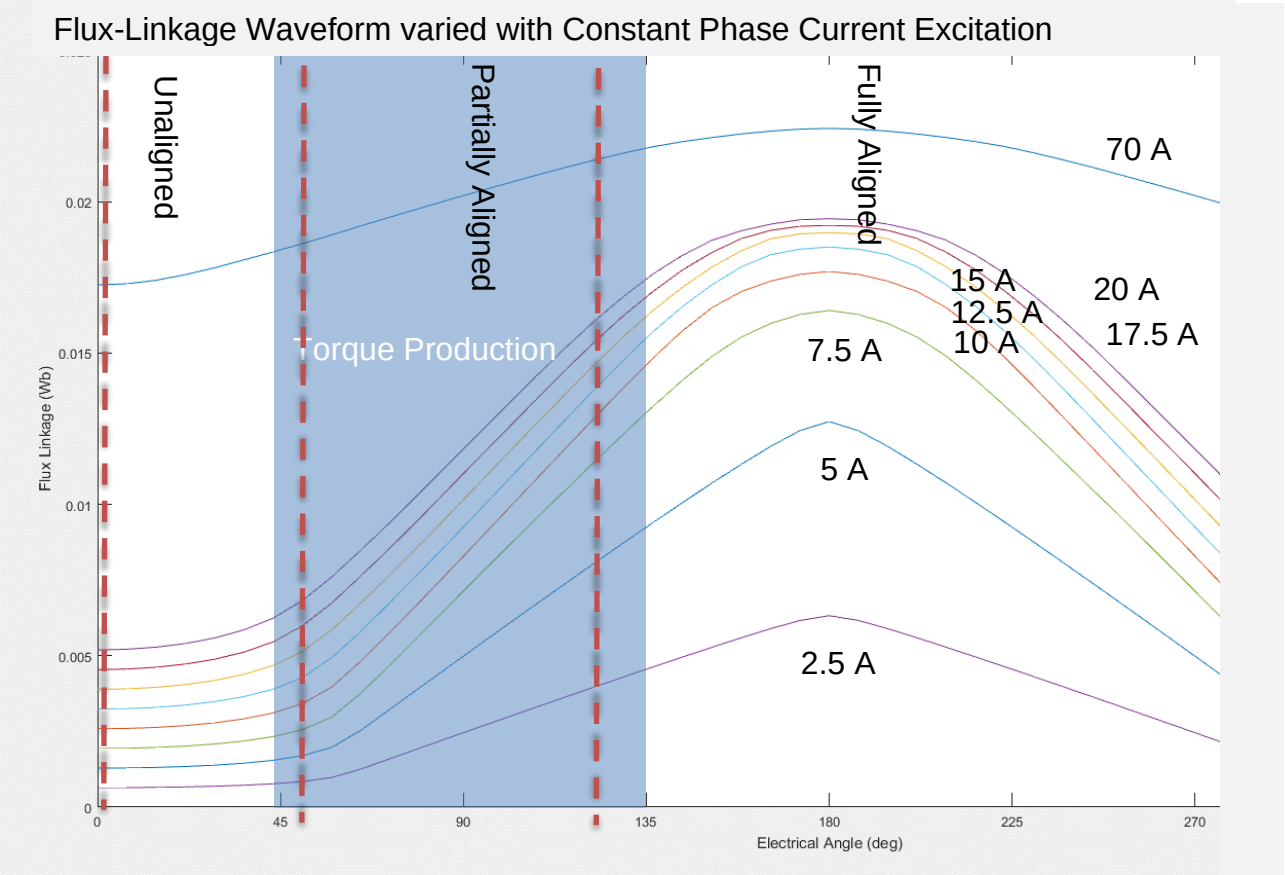

Figure 3-6: Variation of flux linkage with phase current and position

There are many design choices we can make when determining the machine geometry to maximize torque. It is difficult to predict how changes to the design of an SRM will affect torque production without electromagnetic modelling. In an SRM most geometry changes will affect how the circuit saturates, the position of the rotor poles, or both. Similarly, control strategy changes will affect the amount

of current available to saturate the poles at any given electrical angle. In both cases, the effect of changing even a small detail must be evaluated numerically the find both the flux-linkage waveform and the current for each operating point. Finally, the magnetic permeability of the lamination steel affects the torque density of an SRM, since it impacts how easily the flux links in the magnetic circuit (ie. a high permeability material will have a higher flux linkage in the aligned position). Flux density increases with an increasing external field, while permeability decreases. Thus, material choices must also be included in SRM modelling [19]

3.3 Complications to Torque Production

With only one source of excitation, the SRM only produces flux linkage when the phase coils are excited. However, increasing the current to the required level for our desired flux-linkage takes a finite amount of time:

$$\frac{d\lambda}{dt} = L(\theta)\frac{di}{dt} + i\frac{dL(\theta)}{d\theta}\frac{d\theta}{dt} \tag{3-16}$$

The term $i\frac{dL(\theta)}{d\theta}\frac{d\theta}{dt}$ is an induced voltage opposes the applied voltage in our phase circuit due to electromagnetic induction. The faster the motor spins, ω, the stronger this induced electromotive force (EMF), $\mathcal{E}$. We can, therefore, define the equivalent circuit of an SRM:

$$V = Ri \quad + L(\theta)\frac{di}{dt} + i\frac{dL(\theta)}{d\theta}\omega = \ Ri \quad + L(\theta)\frac{di}{dt} + \ \varepsilon \tag{3-17}$$

As per Lenz's law, the EMF will oppose our attempts to inject current into a phase. This will complicate our ability to control the machine. EMF is dependant both on inductance and rotor speed. If EMF gets too large it can limit our ability to grow current to reach the necessary level to meet a given torque-speed operating point:

$$\frac{V - \ \varepsilon}{L} = \frac{\partial i}{\partial t} \tag{3-18}$$

Where it should be noted that the above equation is neglecting the stator resistance. To understand how the EMF complicates torque production let's take a look at basic current control of an SRM using the asymmetric bridge converter. To generate a current level the DC link voltage has to overcome the induced EMF. At low speed, the controller can keep the phase current in a hysteresis band (between I_{upper} and $I_{lower,}$ as shown in Fig 3-7. DC link voltage is switched to maintain the current within these bounds, which allows the increase in inductance, and thus flux linkage with rotor position. However, as the speed rises, the time to reach the current level will increase, and thus phase turn on angles will need to be advanced. At a certain speed, the EMF will become so indomitable that the phase current is unable to reach the commanded value.

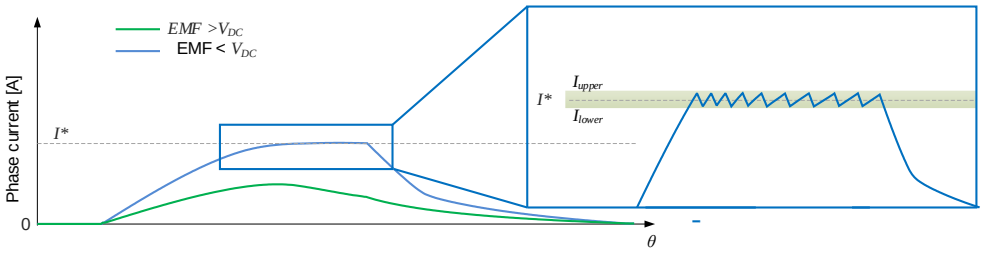

Figure 3-7: Phase current and voltage for low speed (blue) and high speed (green). (Adapted from [20]*)*

Asymmetric Bridge Converter

Each phase of an SRM is controlled via a phase-leg of an asymmetric bridge converter, as seen in Fig 3-8. Each phase can be used in one of three fundamental operation modes: forward current, freewheeling or reverse current. Forward current is the magnetization phase when electrical energy is converted into magnetic energy and heat. As seen in Fig 3-8, both switches will close on the phase leg, which applies a positive DC link voltage to start building current.

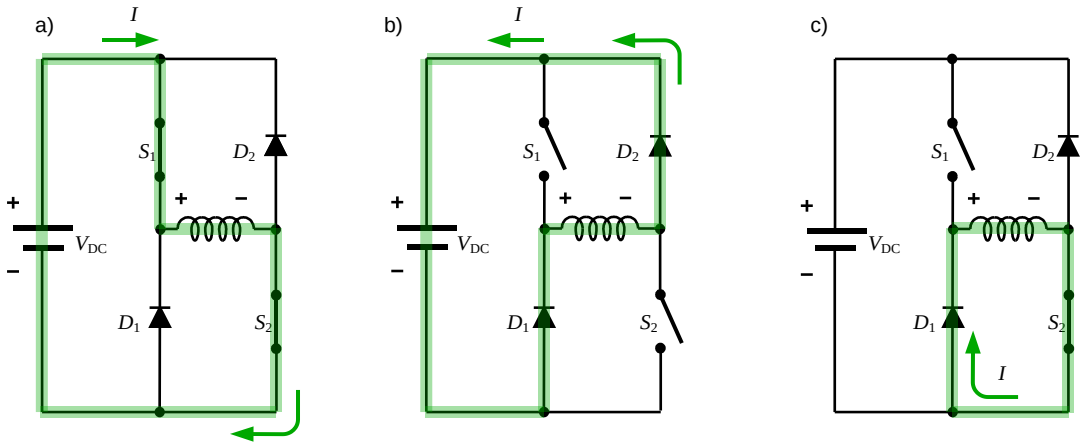

Figure 3-8: Phase leg of an asymmetric bridge converter for a) forward current, b) reverse current and c) freewheeling [21]

Due to inductance, after the voltage is applied it takes time for the current to reach the required level. Once the current has been built, it will need to be maintained at that level which can be done by utilizing the converter's free-wheeling mode of operation. During current regulation, we can close only the bottom switch causing current circulate through the phase coils. This slowly reduces the current to dissipate energy through resistive losses.

The phase will need to be turned off at the end of the torque production range to avoid generating negative torque. The reverse current mode is applied just before the phase turning off to demagnetize the phase. In this mode, both switches will be opened to reverse the voltage applied to quickly remove current from the coils.

3.4 Sources of Loss

As a motor converts electrical energy to mechanical energy, some energy is lost in the form of heat. Typically losses are classified by mechanism: copper, core, mechanical and 'other' or 'stray' losses.

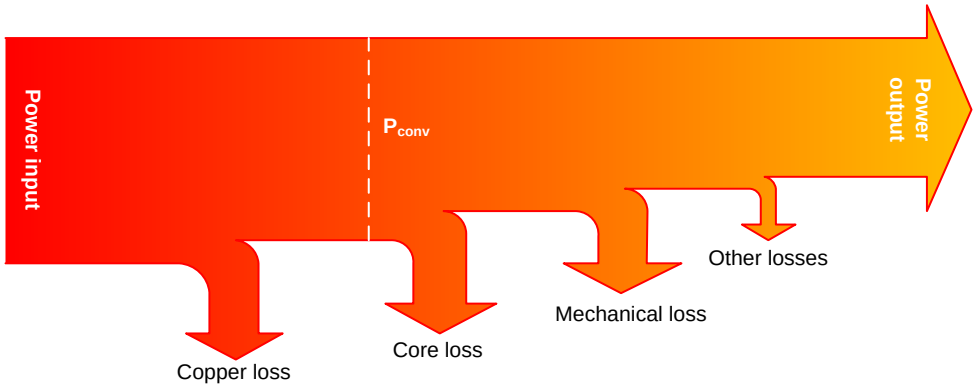

Figure 3-9:Power-flow diagram: Loss distribution of a typical switched reluctance machine. (Adapted from [22]*)*

As electrical energy is input into the system it will be turned into resistive losses first, with the rest converted to magnetic energy within the magnetic circuit, as seen in Fig 3-9. Core loss, mechanical loss and other losses are then removed from the system during the production of mechanical power [19]. The efficiency of the system, η, can be calculated by subtracting the input power, P_{in}, from the total losses, (P_{loss}):

$$\eta = \frac{P_{in} - P_{loss}}{P_{in}} \times 100\ \% \tag{3.19}$$

Mechanical losses typically refer to friction and air resistances such as: bearing friction and windage losses. Mechanical loss is dependant on the speed only, the load is not a factor. In low-speed operation mechanical and other losses are typically neglected. Copper loss and iron loss are typically the dominant components that determine the efficiency of the machine and are therefore focused on here.

3.4.1 Copper Loss

In switched reluctance machines, the copper loss is usually the most significant loss inside the machine [16]. Copper losses occur in the windings of a motor and are divided into AC and DC components. The DC component simply describes the loss of energy in the form of heat due to electrical resistance when current flows through a wire conductor under uniform current density:

$$P_{cu} = i^2 R \tag{3.20}$$

For the AC component, the current density may not be non-uniform depending on frequency. The total power loss is, therefore, dependant on the resistivity, length, cross-sectional area, as well as the current density across the radius of the wire:

$$P_{cu} = 2\pi l\rho \int_0^{r_0} J^2(r)\,\mathrm{r}\,dr \tag{3.21}$$

Where ρ is the resistivity of the wire material (copper), r_0 is the radius of a round wire, l is the length of wire and J is the current density in A/m^2. The skin effect, shown in Fig 3-10 a) occurs for a single conductor as AC frequency increases. The wire's self-induced flux linkage causes current density to increase towards the outside of the wire and decrease internally. Skin depth, δ, is how far into the wire you find the maximum current density:

$$\delta = \frac{1}{\sqrt{\pi\mu\sigma f}} \tag{3.22}$$

Where f is the excitation frequency, μ is the permeability of the conducting medium and σ is the conductivity of the conducting medium. As the skin depth increases the effective cross-section of the wire decreases. Therefore, the effective electrical resistance rises causing increased copper loss.

The current density radial distribution in a wire can also be affected by neighbouring conductors, known as proximity effect (shown in Fig 3-10 b)), or by

the leakage flux in the slot, known as slot effect. The slot effect tends to cause current to localize near the slot opening. Circulating currents, meanwhile, are an uneven distribution of the total current through parallel strands of a wire due to the field effect of nearby conductors [19], [23].

AC copper loss can be calculated analytically, numerically using FEA or a hybrid method of these two. Analytical models tend to make simplifying assumptions based on the coil winding type, however, in general, a physical parameter based on slot dimensions, conductor distribution and frequency is used to determine current density in the affected region of the wire [17]. Given the interdependent nature of these effects, electromagnetic FEA is popular, especially for complicated winding arrangements and slot geometries. However, it can be computationally costly, especially if every conductor is meshed with precision. The hybrid method combines the strengths of these two, calculating the slot flux leakage using FEA magnetostatic methods and then applying the result as an external field to an analytical model [24].

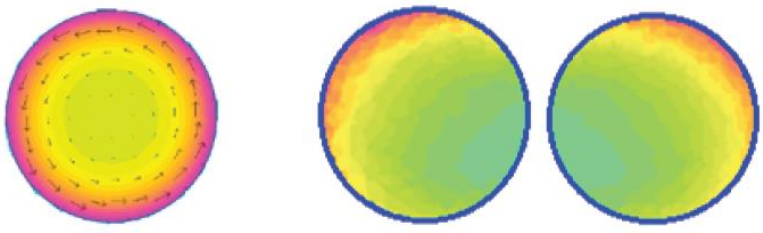

Figure 3-10: Skin effect in a circular wire (left) and proximity effect for adjacent wires with the same current direction (right) [25]

In addition to electromagnetic interactions, copper loss can also be influenced by winding temperature. As temperature increases, the electrical resistivity of conductors also increases. Therefore, a temperature feedback loop can occur where copper losses increase the temperature of the windings causing more copper loss. Copper loss is generally calculated at a constant temperature, however, the increase in resistivity of copper with temperature can be described as:

$$\rho = \rho_0[1 + \alpha(T - T_0)] \tag{3.23}$$

Where ρ_0 is the referenced resistivity of copper at the starting temperature T_0 and α is the temperature coefficient of resistivity of copper, $3.9 \times 10^{-3}/℃$.
Temperature rise can have a large effect on total copper loss, causing a 50% higher copper loss at 150℃ than 20℃ for the same operating point [26].

3.4.2 Core Loss

An electric motor runs at variable speed, meaning the frequency of the magnetic excitation is variable as well. As excitation frequency increases, core loss increases which creates a speed dependency on P_{core}. Core loss is also dependent on the magnetization strength of the external magnetic field

Fig 3-11 shows the loss curves produced by electrical steel under sinusoidal excitation at a constant frequency, which is the form provided by steel

companies. To accommodate variable speed motors FEA programs, like JMAG, take the loss curves and interpolate between them.

SRMs pose a particular challenge because the magnetic flux waveforms are non-sinusoidal [27]. There is no fundamental, physical model for microscopic magnetization to predict the core loss of steel under varying excitation [28]. Instead, empirical equations, like the Steinmentz equation, exist for sinusoidal excitations:

$$P_v = C_m \hat{B}^{\beta_s} f^{\alpha_s} \tag{3.24}$$

Where, the power by volume P_v, is given by the peak magnetic flux density $\hat{B}$, the frequency *f*, and then three fitting coefficients: α_s, β_s, C_m. Steinmentz equation's variable coefficients can be fit to loss data from a steel manufacturer (like Fig 3-11). Other macroscopic or empirical approaches include the hysteresis model (such as the Jiles-Atherton [29] and Preisach models [30]) and loss separation approach (such as Jordan [31] or shown in equation 3.24), however, they suffer from poor accuracy or limited practical use due to computational or experimental complexity [32]. Under sinusoidal flux conditions, core loss is computed in the frequency domain as follows[33], [34]:

$$P_v = P_h + P_c + P_e = K_h f \quad \hat{B} \quad + K_c f^2 \hat{B}^2 + K_e f^{1.5} \hat{B}^{1.5} \tag{3.25}$$

Where P_h is the hysteresis loss, P_c is the eddy current loss,

P_e is the excess loss, and similarly K_h, K_c and K_e are the material constants due to

hysteresis loss, eddy current loss and excess loss respectively. When a DC component exists in the flux density, the core loss is modified to the following:

$$P_v = C_{DC}P_h + P_c + P_e = K_h f \quad \hat{B} \quad + K_c f^2 \hat{B}^2 + K_e f^{1.5} \hat{B}^{1.5} \tag{3.26}$$

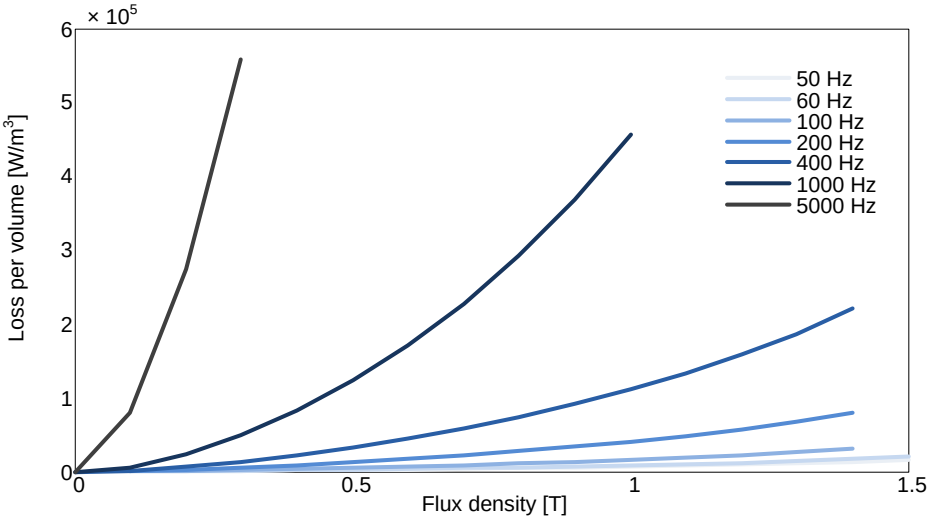

Figure 3-11: Curves of core losses at different frequencies, for lamination steel JFE 30JN loss per volume [18]

To extend this model to non-sinusoidal waveforms, the Modified Steinmetz Equation is produced, which allows for the calculation of core loss for arbitrary shapes of magnetic flux density [35]:

$$P_v = (C_m \hat{B}^{\beta_s} f_{eq}^{\alpha_s - 1}) f_r \tag{3.27}$$

where f_r and f_{eq} have been found by relating f to the macroscopic re-magnetization velocity. However, in addition to non-sinusoidal flux waveforms SRM also has as unevenly distributed flux density and frequency that must also be accounted for. Figure 3-12 shows the flux waveforms for an SRM rotor and

stator at low and high speed. This complex interaction is not accounted for in equation 3.26 but can be applied via FEA to each harmonic component separately, and take the total loss as the superposition of the separate components.

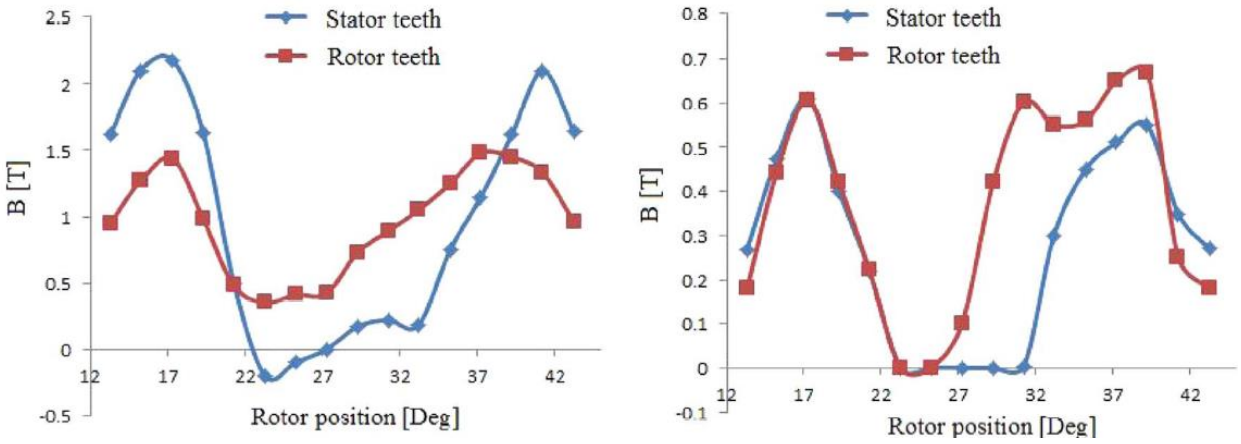

Figure 3-12: 4-phase 16/12 traction SRM flux density curves at low speed (left) and high speed (right) for a single element [36]

Yu et al. [36] proposed a new method that sums the effect of minor BH hysteresis loops over a discretized geometry using magnetic circuit calculations for computational speed. For each element, a local, time-varying flux distribution is used, and an empirical loss model is calculated. Analytical definitions for eddy current and hysteresis loss based on loss separation models and the Steinmetz equation are formulated. Loss coefficients are calculated for each element based on local frequency, flux density, rotor location, and operating conditions. Experimental validation was performed for a 16/12 30 kW 4-phase SRM and found an error in the predicted loss of less than 10%, even at high torque when the machine is greatly saturated. A secondary problem in estimating core loss

exists due to stress in the lattice leftover from manufacturing methods which can greatly change the B-H curve [37][38]. Yu et al.'s core loss method represents a good framework to apply loss effects due to manufacturing methods since the flux density is calculated based on geometry. Most stress effects from manufacturing have an affected region, outside of which the losses function as calculated in [36]. An element could be added to these circuit descriptions to better estimate the core loss effects of stress.

Chapter 4

LUMPED PARAMETER THERMAL MODELLING FOR ELECTRICAL MACHINES

A Lumped Parameter Thermal Network (LPTN) is a network of nodes that represent each individually represent a lumped volume. LPTN has been an attractive model choice for electric machine thermal modelling due to its low computing time and simple structure. However, this simple structure belies the non-trivial challenge of defining the network in a physically significant fashion for a given heat transfer problem. Transient thermal problems are a separate class of modelling challenges above and beyond the steady-state solution. In this chapter, we will introduce how LPTNs are utilized to model electric motors, including how they are defined and calculated. We will explore the major assumptions and factors that are required for high accuracy, spatially dependant LPTN, capable of dynamic simulations.

4.1 Lumped Systems Modelling

4.1.1 Lumped Parameter Networks

A lumped system is one in which temperature varies with time but remains uniform in space throughout the solid **at any time**, i.e. $\frac{dT}{dx} \cong 0$. Within the volume defined by the lumped system's characteristic length, $T(x)$ will be considered constant. The lumped system will therefore be considered in local thermal equilibrium across its volume. As time moves forward, i.e. as we advance the time step, Δt, the uniform temperature of the system will update as heat is exchanged with its environment. Each time Δt is advanced the volume of the lumped system will once more come into local thermal equilibrium. By iterating a lumped system forward in time with an appropriately chosen characteristic length and time step, the system can approximate continuum transient thermal behaviour [39].

An electrical machine can be divided geometrically into a number of varying lumped volumes, each with associated lumped parameters that describe the bulk thermal storage, heat generation and heat flow into and out of the volume. A network can be formed by connecting neighbouring volumes in contact through one of the three modes of heat transfer[40]. Each one of these volumes describes a region of local thermal equilibrium which will each need to come back to equilibrium at the end of every time step. In this way, the network can describe the transient heat flow through the machine, and thus its temperature distribution discretized by volume and time step.[41]

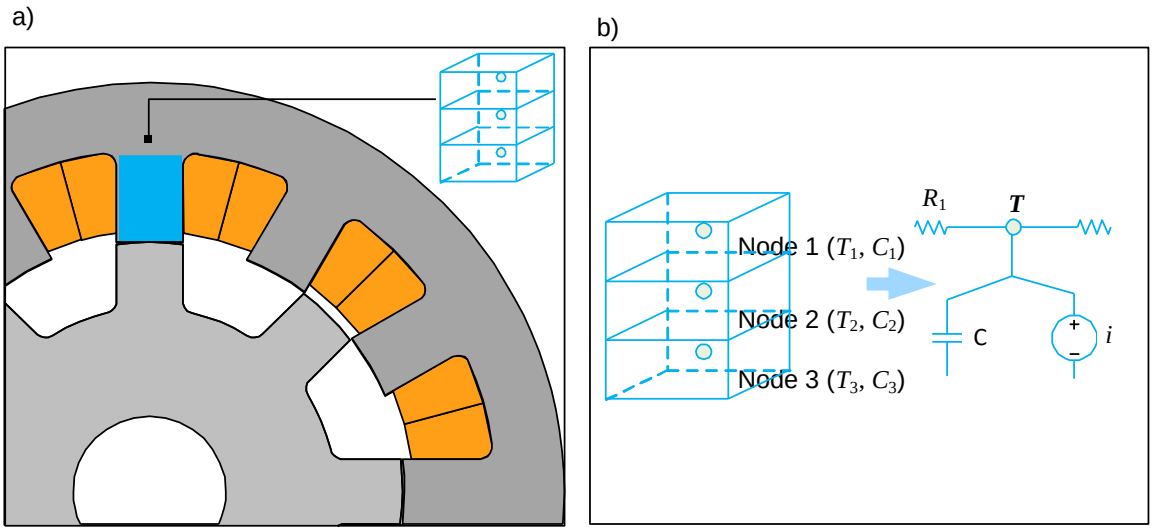

Figure 4-1: a) Nodalization of the motor geometry b) Node within the classic thermal circuit

Dividing the motor volume into lumped volumes is called nodalization, as seen in Fig 4-1 a) [22]. Each lumped volume consists of a central node, as seen in Fig 4-1 b), which is connected to a capacitor and some number of resistors, with each circuit element functioning as we would expect [26]:

- Average temperature corresponds to the potential across the central node
- Anything that impedes the flow of heat is represented by a resistor
- Energy added to the system in the form of losses is represented by a current source
- The energy storage of the volume is captured by the capacitor

The validity of the assumption of local equilibrium for the lumped volume depends on the definition of the characteristic length and time step, which in turn informs the values of the circuit elements.[42] If the characteristic length is too big the

volume may include regions within it that do not conform to $\frac{dT}{dx} \cong 0$. If the time step is too small, then the system will not have time to come into local thermal equilibrium in the time Δt. Given that a thermal transient system is non-linear, error in these foundational definitions can propagate quickly throughout the system.

4.1.2 Characteristic Length Definition

A well-chosen characteristic length for a lumped volume will allow the following assumptions:

- Radial, tangential, and axial heat flow is independent
- A single mean nodal temperature characterizes the volume for that node in all directions
- Thermal capacitance and heat generation are uniformly distributed within the nodal volume

It is not trivial to determine the size of the lumped volume for these assumptions for all systems[43]. For instance, heat generation can be highly distributed given the loss mechanisms discussed in Chapter 3[44]. The size of a lumped volume will be determined by the size of the spatial temperature gradients between and within components.[45] Due to the discretization of the system in time and space, there will always be some error between the lumped volume solution and the continuum solution given by equation 2-6. What is the acceptable variation in

$\frac{dT}{dx} \cong 0$, for any given system that will allow the local thermal equilibrium assumption to hold for the lumped volume?

The Biot number, Bi, can be thought of as a measure of how valid it is to consider a region as a lumped volume. The Biot number can be formulated in several ways [46]:

$$Bi = \frac{L_c/k}{1/\bar{h}} = \frac{conduction\ resistance\ within\ the\ body}{convection\ resistance\ at\ the\ surface\ of\ the\ body} \quad (4\text{-}1)$$

$$Bi = \frac{\bar{h}}{k/L_c} = \frac{convection\ at\ surface\ of\ the\ body}{conduction\ within\ the\ body} \quad (4\text{-}2)$$

Where L_c is the characteristic length of the volume, k is the effective thermal conductivity in the direction of the characteristic length and $\bar{h}$ is the effective heat transfer coefficient from the surface from all sources. For a region to be considered a lumped volume, the following requirement should be met:

$$Bi \leq 0.1 \quad (4\text{-}3)$$

Which ensures that temperatures within the lumped volume should be within 5% of each other [39]. Another way of looking at Equation 4-2, this condition is satisfied if there is ‘speedy transport’ of heat via conduction to the surface compared to the rate of heat removal via convection. Each lumped volume in the motor would need to satisfy Equation 4-3 to be considered ‘physically accurate’. For a complicated system like a motor, determining the local value of k, L_c and $\bar{h}$ for a given node may not be trivial. Heat transfer coefficients can have complex

dependencies on motor parameters and operating conditions [47], which we will explore in the next section.

4.2 Heat Transfer Coefficient Approximation in Motors

4.2.1 Conductive Heat Transfer

Conductive heat transfer in an LPTN is governed by the conduction thermal resistance:

$$R_{cond} = \frac{l}{kA} \tag{4-4}$$

Where l is the length of a solid measured in the direction of heat flow, A is its cross-sectional area and k is its thermal conductivity. Three primary areas in the motor suffer from significant uncertainty for the values of R_{cond}: the contact between the coil and slot, the through-plane contact between rotor and stator laminations and the interface between stator and ambient (the housing for internal rotor motors and the shaft for external rotor motors) [26].

Shaft and Housing

The shaft and housing conduction resistances can be approximated by known interfacial resistances between similar materials, and the bearing thermal resistance can be found through previous experimental studies [48].

Rotor and Stator Laminations

The lamination stacks on the rotor and stator are anisotropic in structure. Thin sheets of rolled electrical steel are separated by a thin coating layer between sheets stacked axially. Due to the difference in thermal conductivities between these composite layers, the through-plane effective thermal conductivity of a lamination stack was roughly one-tenth that of the in-plane value (38.7 vs 3.7 W/m°K respectively) for the motor studied in [49]. Also, the through-plane value is dependent on the manufacturing process and motor geometry. A study by the US Department of Energy found that the effective thermal conductivity for a lamination stack dropped to around 1.5 W/m°K depending on the pressure used to press the stack together and the stack length [50]. Several studies have reported experimental values for a variety of stack dimensions and electrical steel grades; however, manufacturing conditions seem to still be not commonly reported [47], [51], [52]. For this study, the stator stack is approximated as a homogenous material with an effective thermal conductivity considering both in-plane and through-plane values[53].

Slot Contact Resistance

In the radial plane of the motor, there are several high thermal resistance steps in the conductive heat path for a random-wound coil to the stator tooth:

1. Heat is transferred from the regions in the coil where it is generated between round wires
2. Through a varnish or encapsulation material (if present)

3. Through the slot liner
4. Into the lamination steel of the stator tooth

Most of those materials have low thermal conductivities and for many motors, those thermal contacts will be of low quality [51]. To determine the equivalent thermal conductivity, some studies have modelled the stator slot as an equivalent homogeneous material for a given slot fill factor [54]–[56]. Other studies have created equivalent models based on the slot shape and dimensions [57],[58]. However, manufacturing differences alone can introduce uncertainty into the contact resistances of the slot.

4.2.2 Convective Heat Transfer

Convective heat transfer is governed in an LPTN by the convective thermal resistance:

$$R_{conv} = \frac{1}{hA} \tag{5-2}$$

Where A is the area of the surface over which the heat transfer coefficient h is applied. The exact evaluation of h for the complex structure of an electrical machine is one of the most challenging tasks in thermal modelling [47]. The heat transfer coefficients in an electric motor are generally broken down into three regions: frame-to-ambient, air-gap and end-winding convective heat transfer. The thermal capacitance of the air in the air-gap can be neglected compared to the mass of the motor components [4].

The treatment of convective heat transfer in the air-gap has been a difficult topic for most types of electric machines [59]. Convection correlations can be found for simple concentric cylindrical structures, rotating around each other[60], [61]. However, the modern power dense electrical machine with its emphasis on weight and size reduction normally has little in common with these idealized cylinders [57]. Previous authors have already noted the lack of applicable convection correlations for the expansive library of possible motor configurations [49], [52]. However, convection correlations are determined for the specific characteristic lengths from the original study, meaning that a deviation from these ‘standard forms’ results in an uncertainty in the accuracy of the resulting convection heat transfer coefficient.

Switched reluctance motors face a lack of appropriate semi-empirical correlations for the air-gap region. Romanazzi et al. studied an 8/6 internal rotor SRM for traction applications, modelling saliency only on the rotor with a completely smooth stator surface [62]. However, in line with other studies on slotted rotating cylinders, a critical value of the Taylor number was found above which increasing instability in the flow occurred. For external rotor SRM, there are no CFD or experimentally determined convection correlation studies available to date. A thorough study of the effect of the double saliency of the rotor and stator slots for both internal and external rotor SRM over a range of pole numbers, slot shapes, axial heights and speeds is missing in the literature.

In the absence of applicable correlations for this geometry, the heat transfer coefficient can be varied in the air-gap during model validation and compared to other studies as a baseline. Li et al [54] used the low-speed correlation from [63] and calculated an average air-gap radius from an internal rotor SRM's outer rotor radius and stator inner radius to conform to the requirements of the correlation. A very similar correlation was used for a low-speed axial-flux permanent magnet machine [49], which rotates in a completely different fashion to an internal rotor SRM. Such use of a very similar correlation [57] for a very diverse range of geometries is illustrative of the uncertainty the literature has for the definition of this coefficient. The Taylor number depends on the average stator and rotor radii, as well as the square of the rotor speed, and thus it is often considered in the literature that simplification of the air-gap geometry can be permitted as long as the correct speed range is used.

A similar situation is encountered in the frame-to-ambient and end-winding convective heat transfer coefficients since components in these areas for many motors can vary significantly from ideal shapes. For the hub motor currently considered, there are no fins or mounting feet, allowing the radial face to approximate a cylinder. However, the end-winding region is a very difficult geometry to approximate. There are many faces with non-standard geometries, for instance, the large variety of winding techniques that can result in very different end-winding geometries. Tovar-Barranco et al. found that the movement of air in the end-space was highly influenced even by rotor wafers, to the point

the correlations for similar induction machines could not be used in a smooth rotor Permanent Magnet Synchronous Motor (PMSM). The region is notoriously difficult to model even in numerical methods and is beyond the scope of this thesis [52], [64]. As such the film coefficients off the many faces in this region are lumped into a single effective heat transfer coefficient and tuned to experimental data[65].

4.2.3 Radiative Heat Transfer

Radiation is the least studied of the modes of heat transfer, primarily because it has been deemed negligible at motor temperatures by many studies. Boglietti et al demonstrated that for small, low-speed enclosed motors that assumption is not valid [66]. For these motors, the contribution is of the same strength as natural convection, and in a vacuum, it is the only mode between the housing and ambient. Three areas of primary interest were proposed for modelling radiation exchange: between housing and ambient, between end-windings and the end-plate and between the coils and the stator slot.

Radiation heat transfer is represented by the radiative thermal resistance of LPTN:

$$R_{rad} = \frac{1}{\zeta_{rad} A_{surface}} \tag{5-3}$$

Where for a surface of area $A_{surface}$ radiating to ambient, ζ_{rad} is given by:

$$\zeta_{rad} = \frac{\sigma_{rad}\epsilon_{rad}\left({T_{surface}}^4 - {T_{surroundings}}^4\right)}{T_{surface} - T_{surroundings}} \tag{5-4}$$

Where ϵ_{rad} is the hemispherical emissivity of the surface, σ_{rad} is the Stephan-Boltzman constant. If instead, we are describing the radiation exchange between two surfaces, ζ_{rad} and $A_{surface}$ can be described as:

$$\zeta_{rad} = \frac{\sigma_{rad}\epsilon_{rad}\left({T_1}^4 - {T_2}^4\right)}{T_1 - T_2} \tag{5-5}$$

$$A_{surface} = A_1 \ F_{1\,2}$$

Where $\mathrm{F}_{1\,2}$ is the view factor given by Equation 2-23. Characterizing motor geometry into a discrete number of faces is quite challenging, especially in the end-space. As such, view factor calculations primarily consider simple shapes with well-known equations like flat plates and concentric cylinders [67]. Due to the low strength of radiation, the emissivity is often approximated over a wide range, such as 0.9 to 0.3 [49]. Rostami et al. varied the emissivity of the frame surface by +/- 30% to determine the sensitivity of the temperature of radiation exchange between the coils and end-plate. This variation resulted in a +/- 4.5 °C difference in end-winding temperature for their low speed enclosed motor. The same study found only a 1.6 °C drop in end-winding temperature after increasing the air-gap convection coefficient by 50% and only 1.8 °C drop after increasing the end-winding convection coefficient by 50%. A possible 9 °C difference in end-winding temperature is not negligible and this finding implies low speed, power-dense, enclosed motors radiation must accurately be considered.

View factor calculations rely on surfaces being gray, diffuse and opaque. Over the temperature range of a motor, most of its constituent parts will not have their emissivities meaningfully change with temperature, making gray a safe assumption. However, for instance, stator windings or non-painted housings may not be well suited to these assumptions. Polished metal is known to be specular, and wire insulation coating is usually transparent [68]. Specular surfaces make the measurement of emissivity difficult since they are dependent on viewing angle. Enclosures having specular and diffuse surfaces can use the net-radiation method [67]. However, the complication involved with accurately modelling specular and transparent media would require a special application for the trade-off in time to be acceptable. When considered, specular and transparent media are often modelled as covered with a thin diffuse and opaque high emissivity spray coating [49].

4.3 Physically Accurate Lumped Systems in an Electric Machine

Formulating an LPTN requires physical geometry parameters, ambient temperatures, losses from operation, material properties, and the equations that characterize fluid movement inside and outside the motor (air or liquid). The overall thermal dynamics of the system depends on the local temperature gradients inside motor components, which are captured in the definition of lumped volume. The definition of the lumped volume depends on the generation and transfer of heat inside a region versus the ability to remove it, via convection or radiation. Determining local heat transfer coefficients depends on the

manufacturing parameters, and operating conditions [56]. We can determine whether the model is physically accurate by solving for the Biot number with these restrictions in mind. This process is challenging and requires information that may not be readily available.

It is not surprising that most LPTN studies do not consider the validity of the lumped assumption, and instead opt for either a simplified system without high-temperature gradients or a symbolic, non-physical LPTN with tuned parameters. Criticisms of the non-physical LPTN technique for rating problems include:

- the motor is modelled in a symbolic fashion where nodes don't relate to physical parameters, making models difficult generalize findings to other motors or setups,
- the model is restricted to solving for average motor temperature which doesn't provide information about the localized temperatures of critical components, like coils,
- the model doesn't allow for the spatial detail needed to correctly represent inhomogeneous losses. With a lack of spatial information on heat flow it is difficult to draw conclusions about what heat dissipation is occurring in the motor or suggest thermal management strategies effectively.

Components with higher spatial thermal gradients will need more nodes to properly represent temperature changes across a given area or volume. Regions with higher internal heat generation will generally have higher spatial thermal

gradients, like the coils which are a critical component to thermally model. Since iron and copper losses can be inhomogeneously distributed throughout a motor component like the stator laminations, the validity of uniform distribution over a node must be evaluated. Therefore, nodes may be chosen in such a way that they represent the averaged areas of highest loss [46].

With accurate lumped volumes, LPTN can represent a physical lumped system, with nodes representing real points in space. This level of detailed spatial information allows the LPTN to approach the FEA solutions for hot spot and average machine temperatures [26]. This can be achieved with a high discretization of components, without knowing the Biot number, resulting in tens or hundreds of nodes over the entire motor. However, there are diminishing returns to the amount of accuracy improvement versus computation time with increasing discretization.

Chapter 5

THERMAL ANALYSIS OF A 12/16 EXTERNAL ROTOR SWITCHED RELUCTANCE MOTOR

In Chapter 4, the requirements for an LPTN capable of modelling a highly thermally transient system were reviewed and the Biot Number was introduced as a condition of validity for our network. It was highlighted, however, the difficulty in accurately determining the value of the Biot number for every lumped volume in the network. In this Chapter, a power-dense, low speed 12/16 external rotor switched reluctance motor (ERSRM) is analyzed based on available heat paths, possible heating dynamics and ease of modelling. Also, dimensional analysis is presented to check the validity of modelling a concentrated random wound stator core with only a few lumped volumes.

5.1 Characterizing the Motor Transient Thermal Response

5.1.1 External Rotor Motor Heat Paths

The ERSRM under consideration is a hub motor designed for traction applications; specifically, to match the form factor and performance of commercially available E-bike motors. The details of the motor were originally presented in [69], and the motor is illustrated in Fig 5-1.

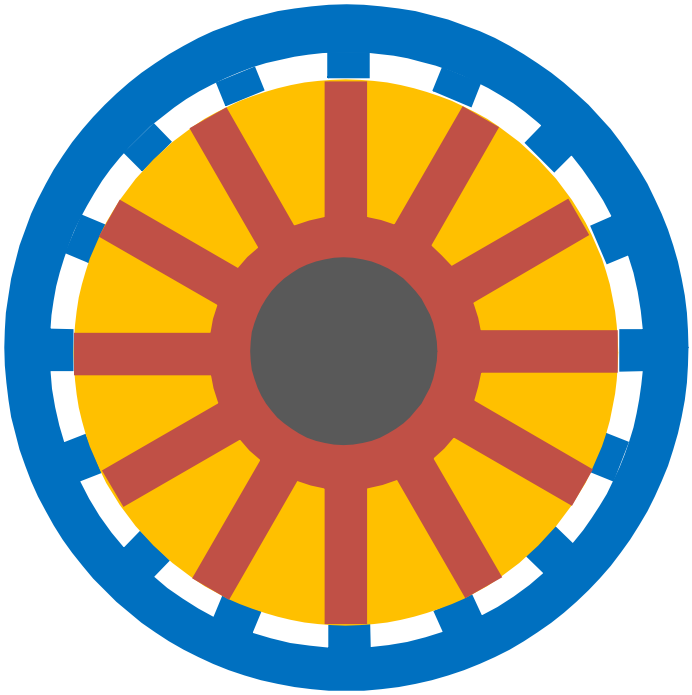

Figure 5-1: Illustration of the 12/16 E-bike ERSRM

In the hub motor configuration, the traction motor can be contained within the wheel with the motor shaft serving as the wheel's axle. The stator is attached to the shaft while the rotor is connected to housing that spins, connected to the shaft through bearings. The rotor + housing arrangement is connected to the rim

of the driven wheel by a series of spokes and surrounds the stator on both the axial and radial faces. The motor is enclosed from ambient and the salient structure of the motor is reduced in its ability to act as a fan by rotor and stator slot liners.

For an internal rotor motor, the stator back iron is in thermal contact with the housing, forming a conductive path with a low but non-negligible thermal resistance [52], as seen in Fig 5-2. This direct contact allows heat to flow radially from high thermal gradient areas like the coils and stator teeth through the stator back iron and into the housing frame to ambient.

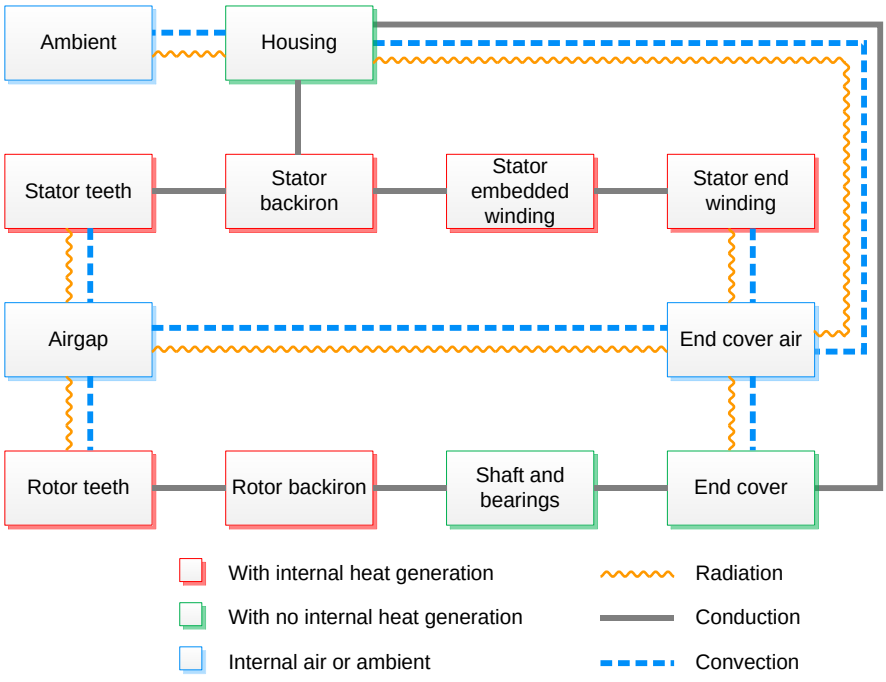

Figure 5-2: Internal Rotor SRM Heat Paths

For an external rotor SRM, the stator is not directly connected to the ambient through the housing. Instead, it must travel through the shaft and to the bearings,

as seen in Fig 5-3. This change in the heat path to ambient results in two primary shifts in the thermal network: convective thermal resistances appear in different locations [52] and the surface area between the shaft and the stator is much less than the surface area between the housing and the stator. The thermal resistances along the heat paths to ambient will have the greatest contribution to overall motor temperature [49].

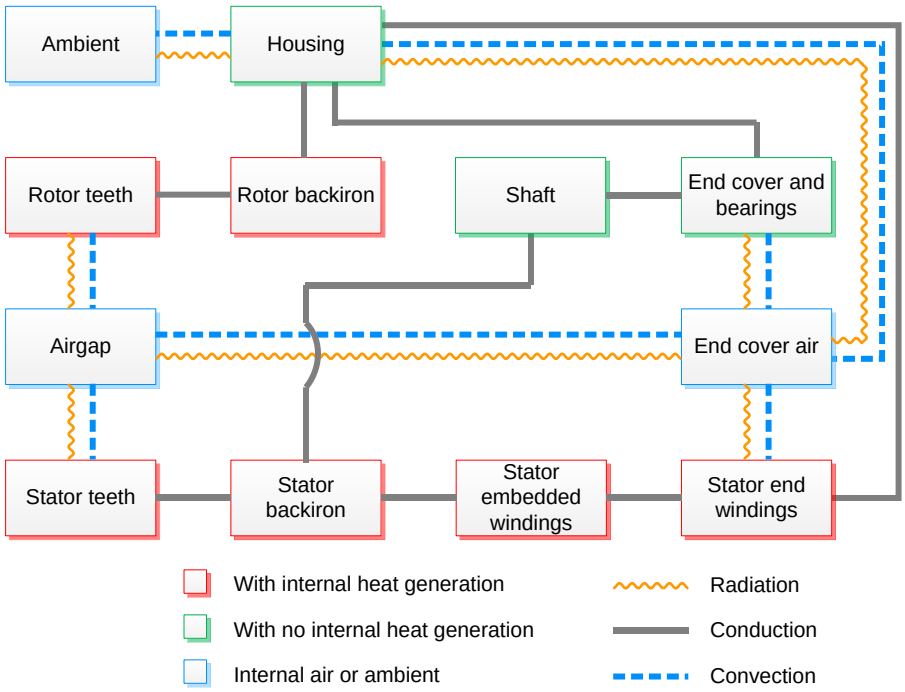

Figure 5-3: External Rotor SRM Heat Paths

For an external rotor motor, this includes the air-gap thermal resistance which is likely very high and the resistance through the shaft + bearings. The difference between housing temperature and coil temperature indicates how difficult it is for heat to reach ambient. The distribution of housing temperatures meanwhile indicates the relative strengths of radial vs. axial heat transfer. Given that the size

of a lumped volume depends on temperature gradient it is important to begin to describe how heat moves through the motor and where the largest gradients might be. Therefore heat dissipation in this motor faces added challenges over the internal rotor motor: heat generation in the motor largely occurs in the coils, which are stranded in the center of the machine with only high thermal resistance paths to ambient. The lack of strong sources of forced convection and high loss causes this problem to be very transient and sensitive to parameter variation.

5.1.2 Traction Motor Transient Operation

Transient, intermittent or duty-cycle operation for traction motors describes the accelerations, decelerations, glides and stops that are common dynamics for traction applications [70]. This behaviour falls under the umbrella of short time transients, where constant loads are maintained for minutes or less [71]. For motors with sufficient thermal capacity, this dynamic loading can allow for brief periods of high loading that would overload a motor designed for continuous operation. The fastest rise in temperature in an overloaded motor occurs in the stator windings [72], which are a vulnerable component to high temperatures.

However, as has been discussed in the literature [70]–[72], many benefits can come from harnessing the ‘window of opportunity’ that can occur between performance request and transient thermal response. Motors designed for intermittent operation can therefore be smaller, require less cooling, etc. than a motor in a continuous loading application with the same power capability. Also, increasingly high energy density systems are required for large momentary load

peaks for rapid acceleration in traction systems and launch requirements for aircraft [72]. For these highly dynamic systems, the transient thermal capabilities of motors need to be well characterized. However, modelling the transient thermal response of motors can be challenging due to the thermal and mechanical parameters that depend on non-analytical properties like the manufacturing method, as discussed in Chapter 4.

To better characterize the transient response, the heating trend can be broken into four regimes: sub-transient, transition, transient and temperature creep as discussed in [72]. The time constant describes the typical exponential increase in temperature that occurs in the transient region. However, before that, the sub-transient regime occurs which is characterized by adiabatic conduction only within the conductor. This is a linear increase in temperature in the stator windings due to the low thermal diffusivity from the center of the copper to the environment (through insulation and possibly low surface area contacts with other surfaces). Heat is stored in the thermal mass of the conductor and a large temperature gradient forms between the coil and its environment. The coil can hit its thermal limit under strong overloads during the sub-transient regime. After the initial adiabatic temperature rises within the coil, the heat begins to meaningfully escape the windings and the end-space begins to increase meaningfully in temperature. This is the transition regime and is difficult to model analytically [72]. By time heat meaningfully reaches the end caps by conduction, convection, and radiation to escape into ambient we have moved to the transient regime.

Therefore, the transient response of a low-speed motor in the sub-transient and transition regimes will be dominated by the coil thermal response. Motors in overload conditions will similarly be dominated by the coil dynamics both due to the physics of what is occurring and the coil sensitivity to high temperatures. Let us investigate this component in more detail.

5.2 Analysis of Lumped Systems Approximation for Motor Coils

5.2.1 Winding System Anisotropy

The temperature of stator windings is a limiting factor in the potential torque density of a motor. Accuracy is required in the thermal modelling of these components since they are both temperature-sensitive, due to their polymer insulation, as well as sources of internal heat generation. Modelling the temperature rise in random wound coils is not a trivial task since their construction is not homogenous, leading to highly anisotropic heat transfer through the coil [47], [57]. Heat transfer out of a coil is affected by thermal resistances in both the motor's frame of reference, shown in Fig 5-4 a) as well as the wire's frame of reference, shown in Fig 5-4 b).

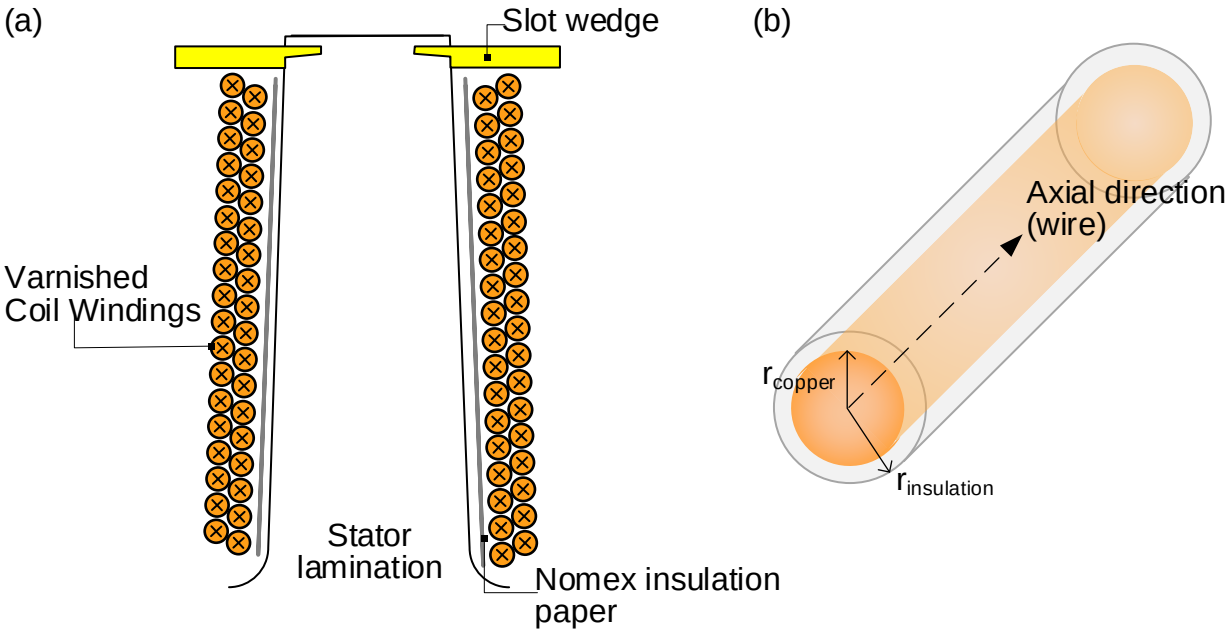

Figure 5-4: Frames of reference for coil heat transfer: a) Motor frame: cross-section illustration in the radial plane of the ERSRM b) Wire frame: radial and axial directions of an individual wire

The anisotropy of the coil means that it is much easier for conductive heat transfer to occur within the coil rather than to ambient. Heat can travel along the length of the wire through the copper conductor, which has an excellent thermal conductivity of 400 W/m°C [57]. However, heat attempting to escape through the surface of the wire (in the wire's radial direction) will experience a sudden drop in thermal conductivity as it moves through one or more insulation layers (thermal conductivity ~<1 W/ m°C).

The heat that travels along the length of the wire, and thus in the axial direction of the motor, will end up in the end-windings [57]. For many motors, the end-windings are stranded from other thermal contacts due to the curvature of the wire, and thus must rely on whatever cooling fluid is in the end-windings such as

air, oil spray, etc [49]. Thus, the heat path for heat to leave the coil overall is dependant on many factors such as motor and coil geometry, fill factor, wire build, material properties and manufacturing process. The factors that affect the winding of a coil can be found in [73]. Due to these requirements for coil winding, in the end-winding area of the coil, the wire's axial and radial directions are no longer orthogonal to the motor's axial and radial directions complicating the modelling of these structures [57]. FEA has been used to model some of these more difficult solid components that can then be included in an LPTN [54]. However, modelling each wire is still a difficult and inefficient task even for FEA [49]. Any method that does not consider the anisotropy of the coil structure may oversimplify the transient behaviour of this critical component.

5.2.2 RC Dynamics of Cuboids

To achieve both average and maximum temperatures, coils are normally broken down into lumped spatial units called cuboids [58]. Cuboids are lumped volumes that conform to the requirements for lumped volumes laid out in Chapter 4. When adding an $R_{thermal}C_{thermal}$ leg to a circuit, its effect can be understood by the time constant:

$$\tau_{thermal} = R_{thermal}C_{thermal} = \frac{1}{hA}mc_p \tag{5-1}$$

Where c_p is the specific heat at constant pressure, m is the mass of the body, h is the convective heat transfer, and A is the area of the body exposed to convection. The time constant,$\tau_{thermal}$ represents the time it takes a body to cool by a factor

of 1/e from its initial temperature difference towards ambient. It is a convenient way of discussing the dynamic thermal response of a system. If our system had only a single lumped capacitance, cooling from an initial temperature, T_{init}, the equation would follow the simple exponential curve:

$$T(t) = T_{init} e^{-t/\tau_{thermal}} \tag{5-2}$$

Where T_{init} is the maximum temperature of the profile. Increasing the number of capacitances, and thus the number of time constants helps describe complicated dynamic systems [46]:

$$T(t) = T_{init} + \sum_{i \to k}^{i=1} -Coeff_k e^{-t/\tau_k} \tag{5-3}$$

A single time constant is not sufficient to describe the entire motor, but what about the coil? How could we determine the number of cuboids required?

5.2.3 Lumped Volume Dimensional Analysis

We can assume speedy transport of heat to the surface of a lumped volume if:

$$\frac{\bar{h} L_c}{k} \leq 0.1 \tag{5-4}$$

Based on equation 4-2, a value <<1 implies that heat transport within the body has a greater contribution than the convection at the surface of the body. To evaluate a coil, let's start at the smallest lumped volume and work outward to see where transport to the surface stops winning. The smallest component is a single copper wire. The thermal conductivity of copper will be much greater than L_c for

the wire. Thus the internal conduction rate becomes irrelevant to the cooling process because there is more than enough heat waiting to be removed from a single wire.

Moving outward radially, what is the rate over the insulation? L_c will be small but so will k.[74] What about the rest of the coil, extending out from one wire? This is where it becomes more difficult to determine the value of the characteristic length since the definition $L_c = \frac{V_{body}}{A}$ assumes a homogenous, isotropic volume. However, we have a composite anisotropic volume. Recall however the definition of a lumped volume is one in which local thermal equilibrium applies. Therefore, we can have a volume that is different lengths axially and radially. Axially, the transport from the copper wire will dominate and the entire active length of the coil can be considered “lumped”. Radially, will be determined instead by how many nearest neighbours fall under the $\frac{dT}{dx} \cong 0$ requirement.

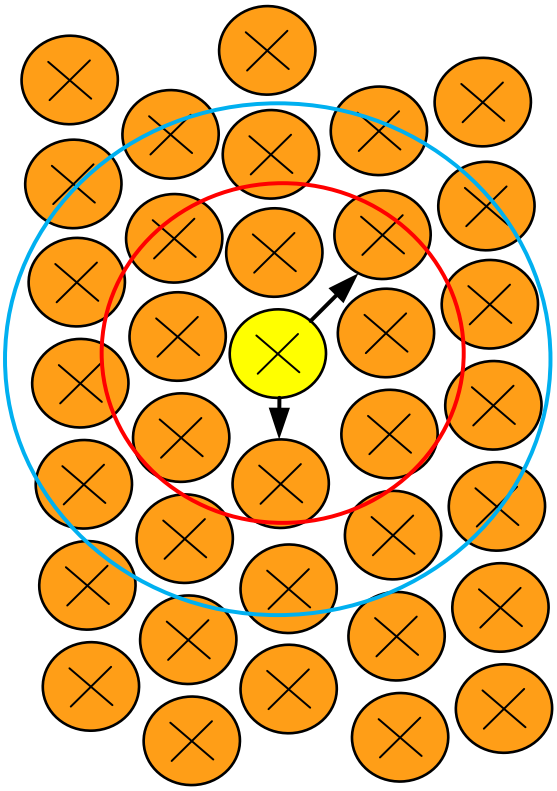

Figure 5-5: Nearest neighbours in the radial wire frame for local equilibrium from an individual wire

Fig 5-5 shows the general directions over which we encounter a repeating arrangement over which we encounter our “nearest neighbours”. Starting from the yellow wire nine neighbours are either in direct contact or adjacent through a gap in the coils. Do these nine nearest neighbours satisfy the requirement? Let’s consider the Biot number of the characteristic length composed of the materials between two wires. That would include the insulation thickness of both wires and the thickness of the gap between coils, with whatever material was present (air or resin most likely). Let’s consider $h = 2.5\ W/m^2K$, i.e. in the range of natural convection and a resin thermal conductivity $k = 1\ W/m\ \ K$, which is rather

generous for most polymer resins. With a wire insulation thickness of, 0.0000584, we can safely say that the nearest neighbours should be in local equilibrium:

$$\frac{(2.5)(0.0001 + \text{gap width})}{1} \ll 1 \tag{5-5}$$

If thermal conductivity were to decrease or h were to increase this would change. Let's assume the gap was full of air, which has a $k = 0.024\ W/m\ \ K$

$$\frac{(2.5)(0.0001 + \text{gap width})}{0.024} \sim 0.01 \tag{5-6}$$

Suddenly we're only two orders of magnitude away. It would require an $h = 200\ W/m^2K$ to cause the same change which is probably unlikely for our low-speed motor. But what is the likelihood of this:

$$\frac{(25)(0.0001 + \text{gap width})}{0.024} \sim 1.042 \tag{5-7}$$

This dimensional analysis is simple but illustrates how easy it is for the system to exceed the Biot number. The coil should never be modelled as a single lumped volume. To find the number of cuboids we can calculate the characteristic length and divide the coil depth by that. Of course, many assumptions are being made in this calculation and it is not exact. Instead, this dimensional analysis can begin to indicate how the number of lumped volumes is affected by coil construction which will affect the values of k_{radial} and $\bar{h}_{cuboid}$. As discussed in section 4.2.2, motor speed can also affect the value of the convection coefficient over a surface

– however to what extent this effect affects us here will have to be left to future work.

A sizing criterion is proposed in Equation 5-8 for approximating the number of cuboids in the radial direction based on the expected value of h over the cuboid, the radial value of thermal conductivity, k_{radial}, and the desired Bi value based on the amount of error that can be tolerated (i.e. usually ≤ 0.1). For a motor of this size there is only one cuboid in the axial direction. Note that in contrast to the tendency to homogenize the stator coil in literature, this criterion maintains its anisotropic nature.

$$L_{cuboid} = \frac{k_{radial}\, Bi}{\bar{h}_{cuboid}} \tag{5-8}$$

$$\#\ of\ cuboids \sim \frac{slot\ depth}{L_{cuboid}}$$

Chapter 6

EXPERIMENTAL VALIDATION – 12/16 EXTERNAL ROTOR SWITCHED RELUCTANCE MOTOR

Little attention has been paid in the motor thermal modelling community to the issue of thermal capacitance in Lumped Parameter Thermal Network (LPTN) models. Thermal capacitance is a crucial parameter for the determination of transient thermal behaviour in a motor. Of particular interest is the thermal capacitance of the stator coils. Coil insulation is vulnerable to heat, copper losses can be a powerful heat source for low-speed high power density motors and coils are hard to model. In this chapter, we will introduce a capacitance calculation method, implement it into an LPTN model and validate that model based on experimental results The LPTN which will be used for primary validation is a 61 node network, modified from a Motor-CAD network formulation. Motor-CAD is commercially available LPTN software that uses a 3D lumped circuit model,

capable of modelling steady-state, simple transient and duty-cycle transient thermal characteristics. The model uses the general cylindrical component and T-equivalent circuit described in [26], [47], [58].

6.1 Experimental Investigation

6.1.1 Set-up

To investigate the thermal cooldown response of an electrical machine a transient thermal test with a rapid heat up and long cooldown has been performed on a traction hub motor; specifically, a three-phase External Rotor Switched Reluctance Motor (ERSRM) is designed for commercial E-bike applications. Fig 6-1 shows the motor under test (MUT), mounted and connected to the dynamometer.

Figure 6-1: MUT with electrical tape on the radial housing to prepare for measurements by the thermal camera

The motor is designed to be driven at low speeds, of approximately 32 km/h. Due to the long constant power region for an SRM, the maximum speed for the motor is 400 RPM which for a 22-inch bicycle wheel would translate to approx. 75 km/h. However, we can still consider the motor to be 'low speed' since during a normal drive-cycle it would rarely leave the constant torque region of the torque-speed curve. The motor is considered power-dense, as seen in Table 6-1, with an average torque density below base speed (i.e. in the constant torque region) of 5Nm/kg.

Table 6-1: Basic ERSRM Details

Peak Efficiency	85.4 %
Rotor Pole Number	16
Stator Pole Number	12
Stator Winding Connection	Delta
DC link Voltage	36 V (DC link)
Maximum RMS phase current	55 A RMS
Average Torque (below base speed)	51.8 Nm
Average Torque (400 RPM)	25.5 Nm
Mass	10.36 kg
Stator Stack Length	39.61 mm

To validate the proposed thermal model, this ERSRM was run on a dynamometer under observation from a FLIR E75 thermal imaging camera and with nine interior thermistors on the coils. The motor was run at near-constant load and then allowed to cool down while stationary, and not excited for an hour. The motor was run using constant current control, with the DC motor acting as the load on the dynamometer shorted to provide the maximum load it could provide. The simple transient period lasted until the maximum coil temperature approached within 10°C of the thermal rating of the magnet wire.

The camera recorded a thermographic video of the radial exterior of the motor, as shown in Fig 6-2, at a frame rate of 30 Hz. The camera was mounted on a tripod above the motor and controlled remotely. Care was taken to align the surface of the lens to be parallel with the tangent plane on the rotor surface closest to the camera. This ensures accurate emissivity calculations due to distance. Since the motor initially at room temperature, nearby warm objects could be reflected in the surface of the motor and appear as changes in apparent temperature. To diffuse or block reflected radiation from the room, a crumpled aluminum foil shield was placed around the dynamometer. This was the plane most of the reflection was coming from, with only minimal radiation sources above the motor (except for the camera itself). Also, black electrical tape was used to raise the emissivity of the surface since it was very reflective of infrared light.

Fig 6-3 shows the positions of the nine thermistors (recording at 100 Hz); arranged three per phase in the same relative positioning. The thermistor at

position one (1) is in the axial center of the coil, near the air cap, position two (2) is in the axial and radial center of the coil and position three (3) is on the top of the tooth near the end-windings at the tooth base. The thermistors used were standard type glass encapsulated NTC thermistors, from TDK (Series B57540G1).

6.1.2 Experimental Results

The motor was run for ~ 97 s before approaching its target limit of 120°C and being manually turned off. Figure 6-4 shows the rise in thermistor temperature by position, where noise is present due to electromagnetic interference from the motor operation. This noise has been filtered using a low-pass filter in Fig 6-6 for comparison. There is some variation between the three phases for each thermistor position. The thermistors themselves were all tested to be within their stated accuracy before insertion in the motor, and the maximum deviation between phase resistances at room temperature was 0.00148 Ω [69]. Therefore, the differences observed between different phases at the same position is likely due to small differences in thermistor placement and the quality of contact between the thermistor and the coil for each installation.

The average maximum temperature between the three phases is 109.5 °C, which occurs at position 3, i.e. the end-windings. There is a 30 °C difference in temperature at motor turn off which supports the conclusion from chapter 5: the coil cannot be considered by a single lumped volume. The temperature gradient across it is far too steep.

Figure 6-2: Placement of the camera and tripod relative to the motor outer surface

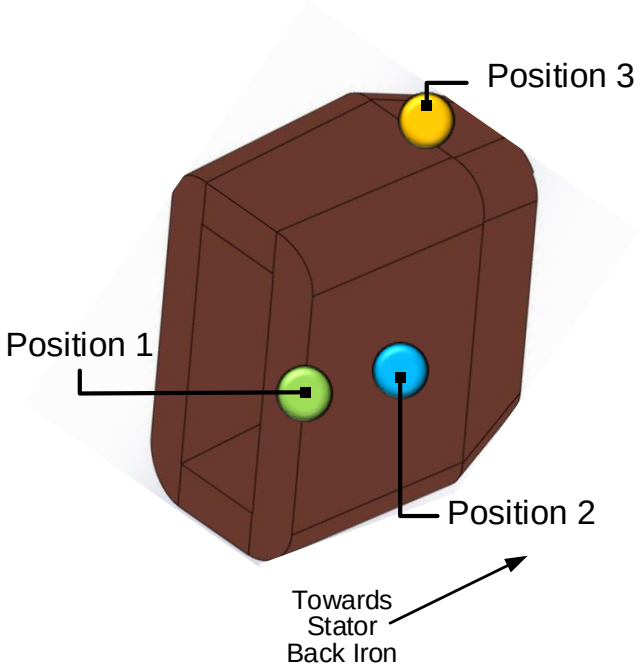

Figure 6-3: Thermistor positions are shown schematically which are placed on phases A, B and C

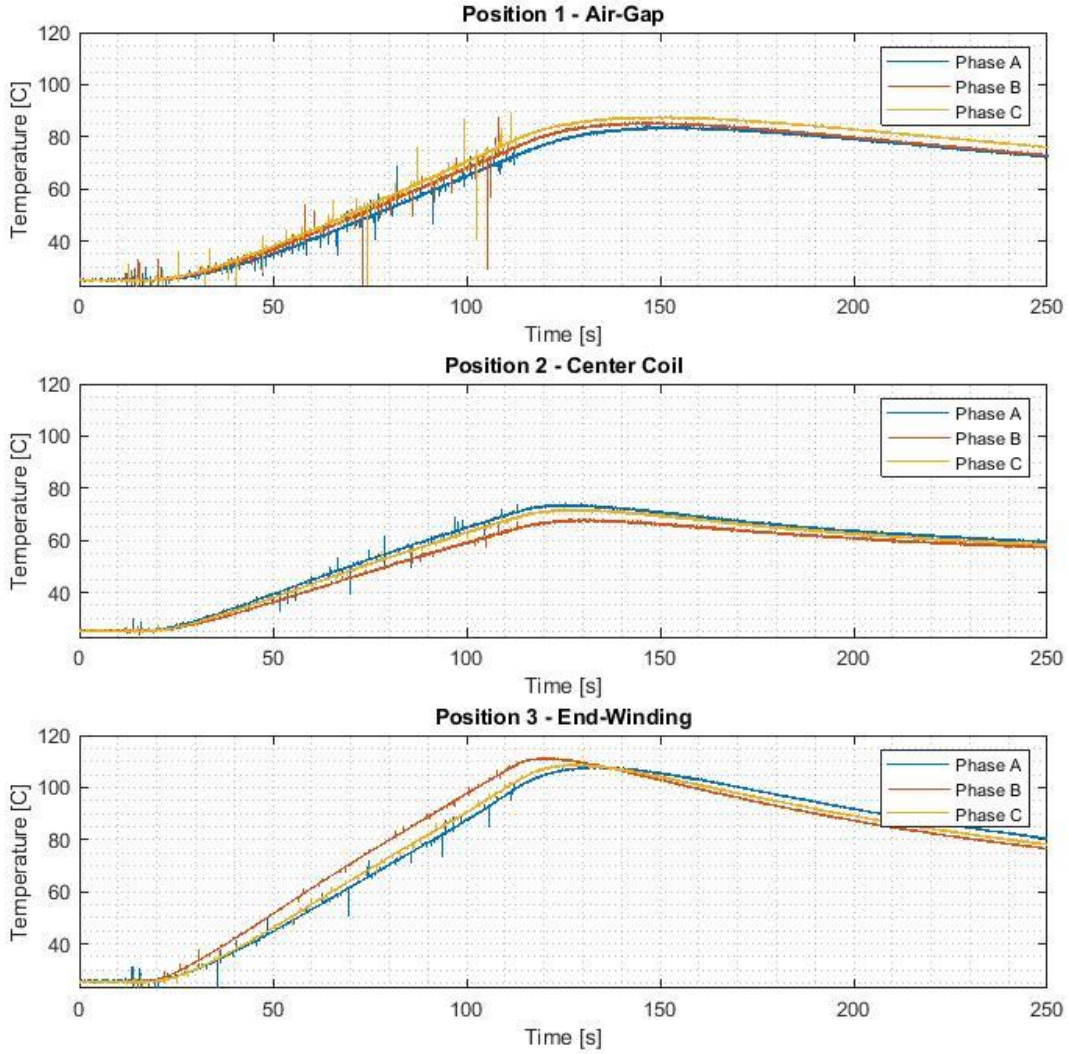

Figure 6-4: Temperature over time for the three positions on phases A, B and C

Fig 6-5 shows the temperature profile for phase A along with the temperature rise in the housing. The housing temperature rises by 1°C in the first ~106 s and is almost 10°C cooler than the coils after 30 minutes of cooling. Therefore, there is a large thermal resistance between the coils and ambient.

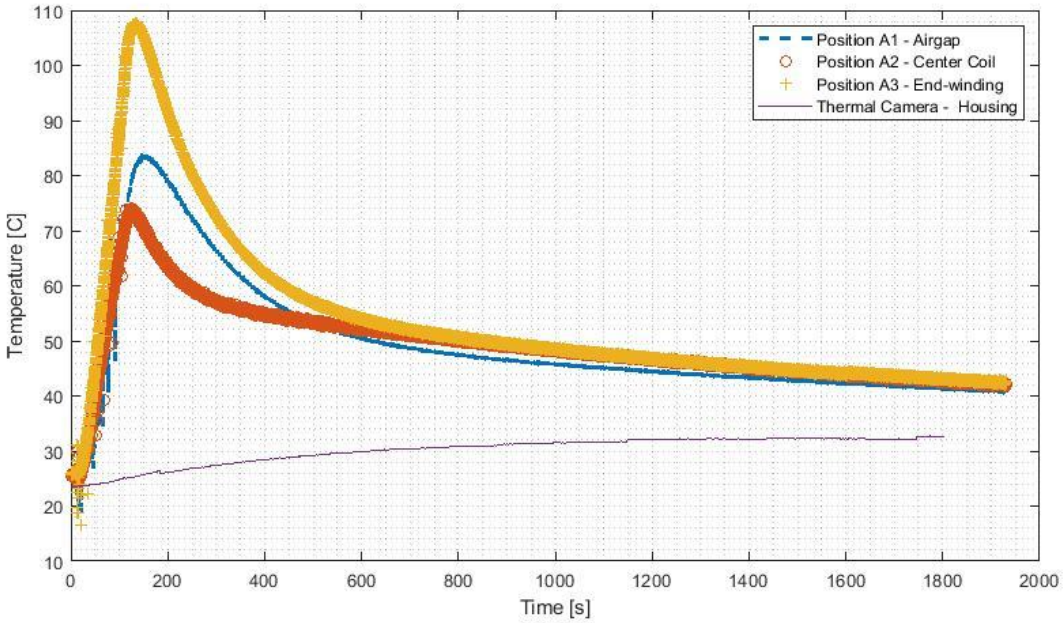

Figure 6-5: Temperature over time for the thermistors on one phase vs. the housing temperature

The motor switches off at ~113 s, causing the motor to enter the transition between heating and cooling regions, as seen in Fig 6-6. The peak temperature occurs in this transition region. The location of the peak temperature for each thermistor position is different: position 2 records an immediate reduction in temperature while position 1 and 3 continue to increase in temperature. Position 2 lies along the active length of the coil and thus has the greatest access to heat paths out of the motor which could be why it responds the fastest.

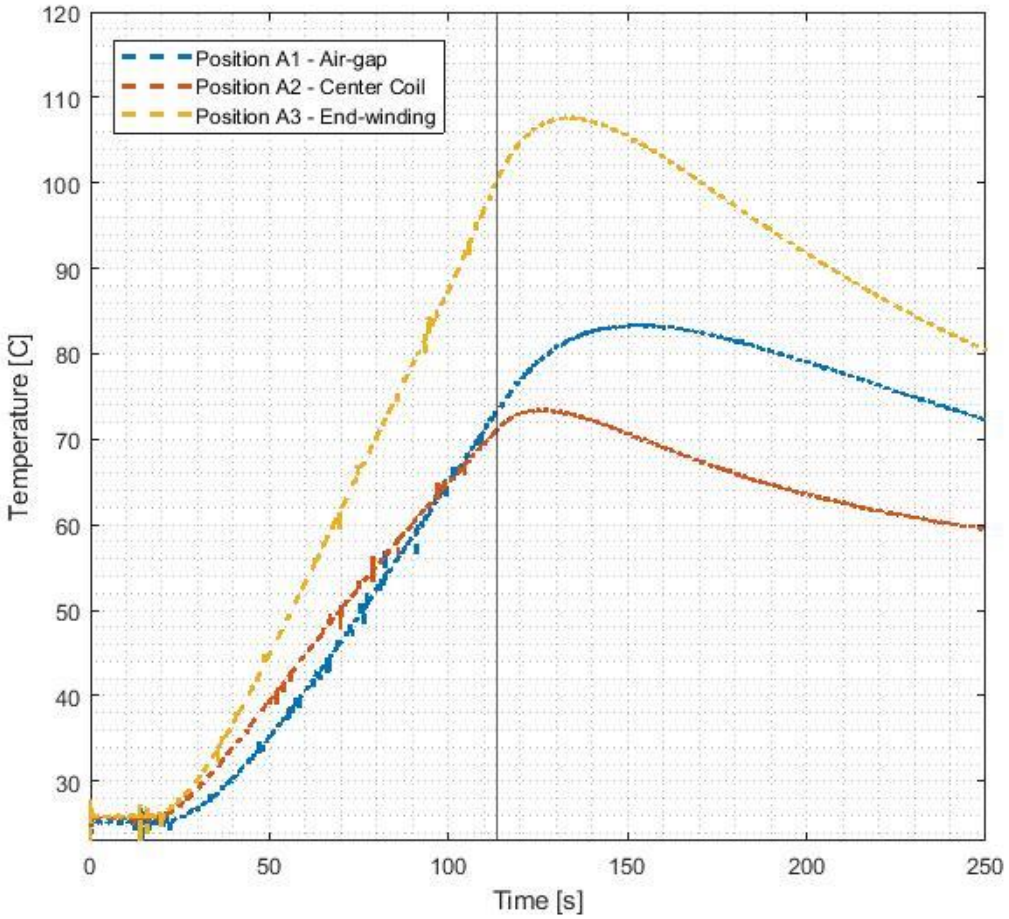

Figure 6-6: The heating trend of the three thermistor positions for phase A resampled with a low pass filter, with motor turn off at 113.31 s (vertical line)

6.2 Stator Winding Thermal Capacitance

6.2.1 Methods for Determining Model Capacitance

The stator winding system consists of randomly distributed motor wire with some combination of varnish, encapsulant, and air. This system is in contact with a slot liner and slot wedge, which are in contact with the stator tooth. The thermal behavior of the stator winding system is dependent on the arrangement of motor

wire, the material properties of all components in the system, and the manufacturing technique [75].

Due to this complexity, the empirical measurement of the thermal capacitance is often preferred [76]. Finding a lumped capacitance of the stator winding system at the component level simplifies calculation since it does not need to independently determine values for all the factors that can influence thermal capacitance. However, during the design of an SRM, the coil's specifics are determined through iteration to find the optimal balance of several performance, manufacturability and lifetime trade-offs. For round concentrated windings in an SRM [77] the choice of coil and slot dimensions has a wide-ranging impact on the performance of the machine:

- The height and width of the slot will impact the wire fill factor as well as the electromagnetic performance of the machine
- The wire fill factor impacts the winding methods that can be used on the machine, the height of the end-windings and even whether the coil will have enough space to be inserted into the slot
- Torque production capability is defined by the current density in the slot which in turn is limited by the slot area, the slot fill factor, the number of turns and the number of strands

- The number of turns and strands depends on the current and voltage rating of the machine.

Empirical measurements are generally performed on a winding sample [58], [76], [78], utilizing some form of calorimetric technique. Without a physical model, thermal considerations cannot be taken into account in the above decisions and thus a sample would have to be manufactured and tested for each configuration designed. Instead of measuring a coil's equivalent thermal capacitance directly, the rate of increase in temperature can inform the capacitance for an already built motor. By fitting temperature rise to curves of known expression, the time constant can be determined and applied to motor rating [79], or for modelling performance under extreme temperatures [80]. Alternatively, the energy injected to excite the coil can be plotted as a function of winding temperature variation. This plot can be fit to provide a value for equivalent thermal capacitance for a reduced-order model [75].

Analytical calculations for coil thermal capacitance are often in the form [54], [71],

$$C_{winding} = V_{winding}\rho_{Cu}c_{cu} \tag{6-1}$$

Where $V_{winding}$ is the volume of the motor coil, ρ_{Cu} is the density of pure copper at 20 °C and c_{cu} is the specific heat of pure copper at 20 °C. This method lumps the volume of the entire coil into a single capacitance, similar to the empirical methods, however without all the detail about the coil construction intrinsically

lumped in the measurement. Equation 6-1 is the least accurate of the capacitance determination techniques presented here and is generally used in models that do not depend on exact transient temperature variation rates. The contribution of the wire insulation material may also be calculated similarly, with some volume modification based on slot volume and fill factor [71]. Simpson et al. included the contribution of an encapsulant compound by considering the proportion of materials, the packing factor, and sample and conductor dimensions and calculating the equivalent specific heat capacity of the resulting “composite” material. Wire insulation was neglected [76].

Empirical approaches, while useful for the motors under study, fail to characterize the coil’s thermal capacitance for generalization to other motors for the same reason they are considered so accurate: they measure *effective* thermal capacitance that lumps the interior contributions to capacitance. We cannot be certain if applied to another motor how much the effective thermal capacitance will vary for a different slot area, slot length, slot width, fill factor, wire gauge, conductor shape, or conductor number in the slot. To make this determination, we would need a physically valid theoretical model of the coil that considered the variation of winding parameters. Such a numerical model, if modelled wire-by-wire, would be tremendously computationally intensive. Meanwhile, current analytical models are not close to being able to incorporate such detail. For an analytical model to be appropriately physically valid, it would need to be grounded in the physical realities of the materials and motor parameters.

However, it would also need to be able to leverage the computational efficiency of the lumped parameter formalism to be able to be incorporated effectively into motor design and optimization.

6.2.2 Maximum Packing Factor Model

A physically accurate representation of the capacitance of the coil in the slot would need to be dependant on the number of strands, the number of turns, stack length, and the gauge of the wire. Dependency on these motor design parameters allows the capacitance model to be generalizable to other coil configurations. We will begin by calculating the volume of an individual wire in the active region, which is just the volume of a cylinder:

$$V_{wire} = \left(\frac{0.701\ mm}{2}\right)^2 \pi(39.61\ mm) \tag{6-2}$$

The total number of wires in the slot is $N_{wire} = (43)(16)(2)$ which are packed into the cuboid volume. The maximum cylinder packing density for cylinders into a cube is:

$$\frac{\pi}{6}\sqrt{3} \tag{6-3}$$

The maximum volume density of objects in a cell can be calculated [5]:

$$packing\ density = \frac{volume\ of\ x\ in\ cell}{total\ unit\ cell\ volume} \tag{6-4}$$

Which results in a total volume of wires in all the slots at the maximum allowable density:

$$V_{Total} = (12)\frac{V_{wire}N_{wire}}{\frac{\pi}{6}\sqrt{3}} = (12)(2.32 \times 10^4\ mm^3) = 2.78 \times 10^5\ mm^3 \quad (6\text{-}5)$$

This is the volume taken up by the entire wire, however, the wire is composed of conductor and insulation materials. By using the same calculation on the copper diameter and subtracting the total volume from the copper volume we can get a composite capacitance for the Maximum Packing Factor (MPF) using Equation 6-1:

$$C_{MPF} = V_{cu}\rho_{Cu}c_{cu} + V_{ins}\rho_{ins}c_{ins} \quad (6\text{-}6)$$

Similarly, if there was a resin present we could find its volume from the coil dimension minus the volume calculated in 6-5. Concentrated wires are unlikely to be wound at precisely the maximum packing density of cylinders in a cube, making our value an absolute lowest bound for a cube. Thus, if the packing factor for a coil is known from experiment, as done in [76], it can be included to modify the packing density.

Total capacitances from MotorCAD and the MPF model are given in Table 6-3.

Table 6-2: Capacitances Comparison between MotorCAD and the Maximum Packing Factor Model

	Calculated Values	MPF Model Values
Total Active Length Capacitance (copper)	730 J/C	1109.9 J/C
Total End-Winding Capacitance	498 J/C	756.742 J/C

The end-windings are challenging to calculate due to even less information being known generally about the wire placement. MotorCAD calculates the value by assuming a volume based on the end-winding over-hang and the wire-fill factor. Our value was calculated by assuming a similar ratio existed to the MotorCAD values as was present for the active length calculation.

6.3 Implementation and Validation of Physically Accurate Capacitance in LPTN Model

A thermal model for the 12/16 ERSRM introduced in Chapter 5 was created using the commercial software MotorCAD. MotorCAD does not have an LPTN for an ERSRM as one of the presets so modifications were made to an external rotor brushless permanent magnet motor circuit. Motor geometry, winding configuration and losses modelled in JMAG in a previous study [69] were used to configure the LPTN. Several simplifications to the geometry were made, such as excluding the conductor shield, bolts, rotor slot wedge, and variations in axle diameter. The radial and axial representation of the geometry can be seen in Fig 6-7.

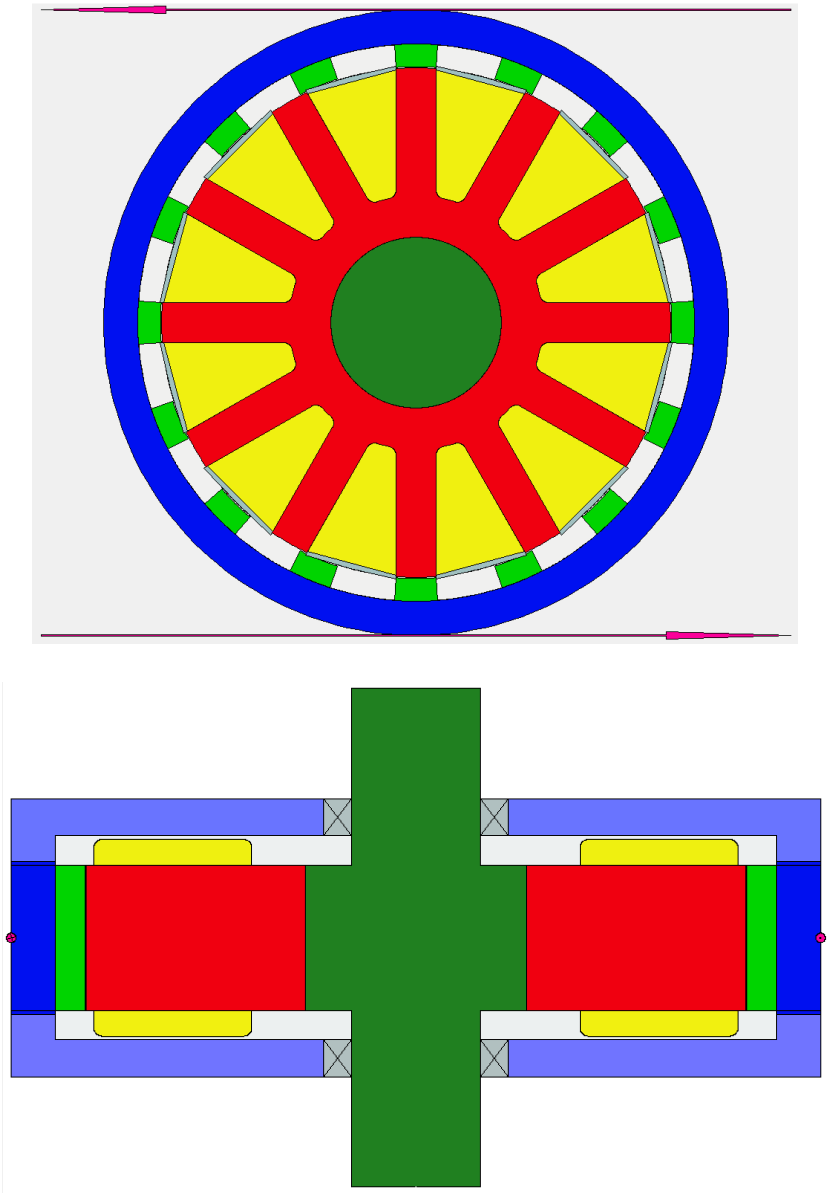

Figure 6-7: Motor geometry representation in MotorCAD: radial (top), axial (bottom)

Windings were modelled by fifteen cuboids using the sizing criterion described in section 5.2.3 and the motor specifications in Table 6-3. Five cuboids in the active length represent the front and back of the coil, and ten in the end-windings do the same. Six is the default number in MotorCAD regardless of coil size. However,

based on the Biot number for this motor six is far too few lumped regions for this coil and causes the model to underestimate temperature. Fifteen was the number chosen to balance accuracy and computational efficiency for modelling the full motor. To verify the model's coil dimensions, the values for the wire fill factor and the slot area were calculated from the input parameters and were found to be are within approx. 2% of each other.

Table 6-3: Coil Specifications for the 12/16 ERSRM and Corresponding Model Parameters

	Motor Specifications	Model Parameters
Winding Type	Concentrated	Concentrated
Number of Turns	43	43
Strands	16	16
Gauge	22 AWG, Single Build	22 AWG, Single Build
Wire Fill Factor	0.6	0.5994
Nominal Copper Diameter	0.6426 mm	0.6426 mm
Nominal Wire Diameter	0.701 mm	0.701 mm
Insulation Class	Class E (rated for 120°C) or better	-
Slot Area	874.9813 mm^2	890.3 mm^2

The goal of this validation is to compare the peak temperature and the heating rate of the experimentally measured winding hot spot temperature profile against the MotorCAD model hot spot profile.

To validate the rate of heating and cooling the experimental results can be broken down into four main regions: initial temperature lag, heating region, final temperature lag, and cooling region. After the motor is excited there is a temperature lag in the response of the recorded temperature [46] which occurs again after the motor is turned off. The heating region can be defined as the temperature rise between the end of the initial temperature lag and the start of the final temperature lag, as shown in Fig 6-8. Similarly, the cooling region can be defined as the temperature decrease at the end of the final temperature lag.

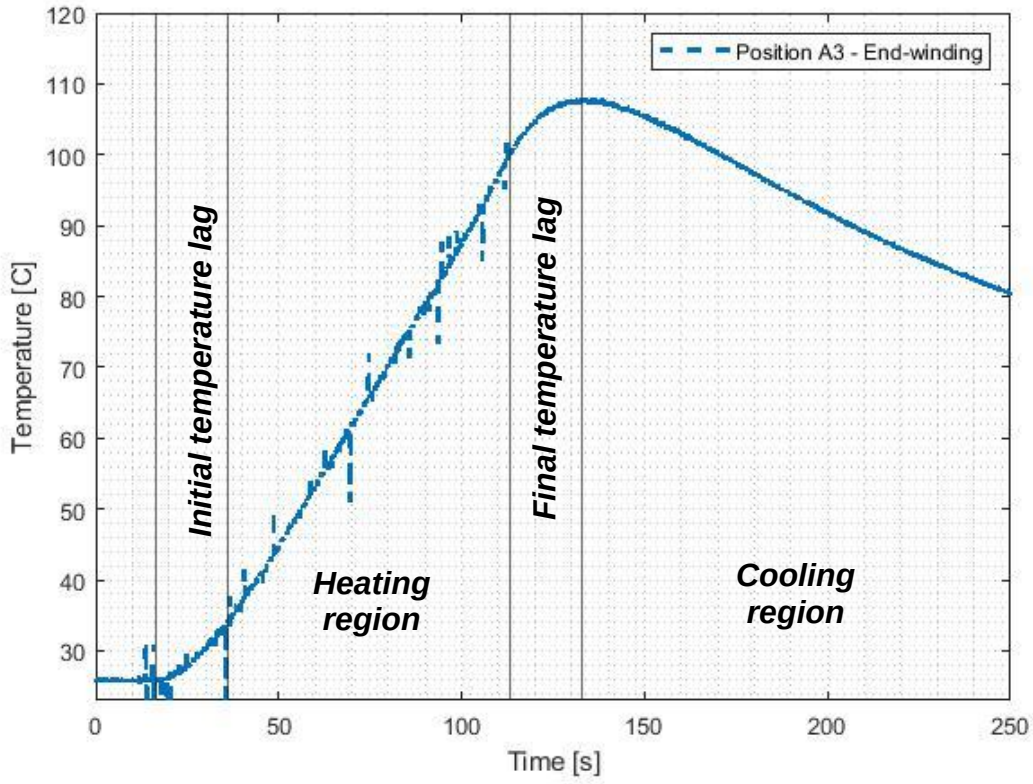

Figure 6-8: Main temperature profile regions for phase A, position 3 thermistor

With these definitions, the heating and cooling regions can be fit via the least-squares method (linear or non-linear respectively) and the system response can be analyzed. The temperature lag regions are not chosen arbitrarily: the final temperature lag is the time between when the motor turns off and when the peak temperature is reached for that profile. This should depend on the time constant of the coil + thermistor system and should be the same for both initial and final temperature lags. However, note that this value is individual to a given coil or part of a coil and therefore the exact definition of the heating and cooling regions will be different for each profile.

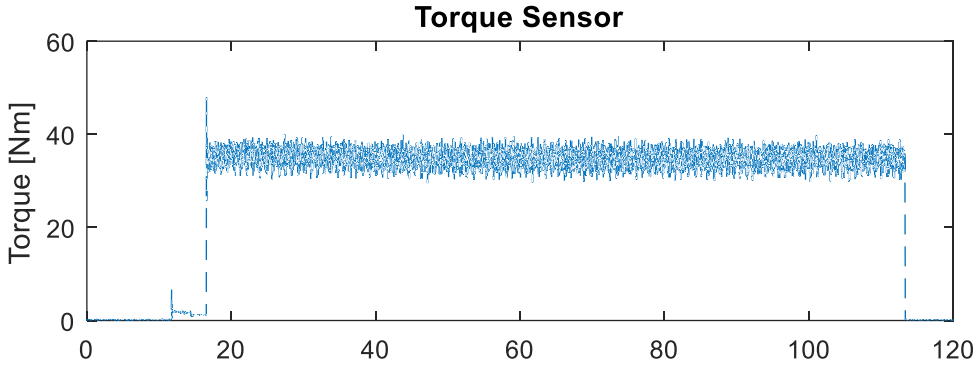

Figure 6-9: Torque profile of the MUT during loading

The heating region was modelled in MotorCAD at the end-windings for the load shown in Fig 6-9 at 150 RPM, with the result shown in Fig 6-10. The curve shown has been shifted to account for the temperature lag. The shifted model was then interpolated using the matlab function interp1 to compare to the model data. The model matches the experimental data in the heating region with a root mean squared error of 2.99, allowing it to approximate the rate and peak temperature.

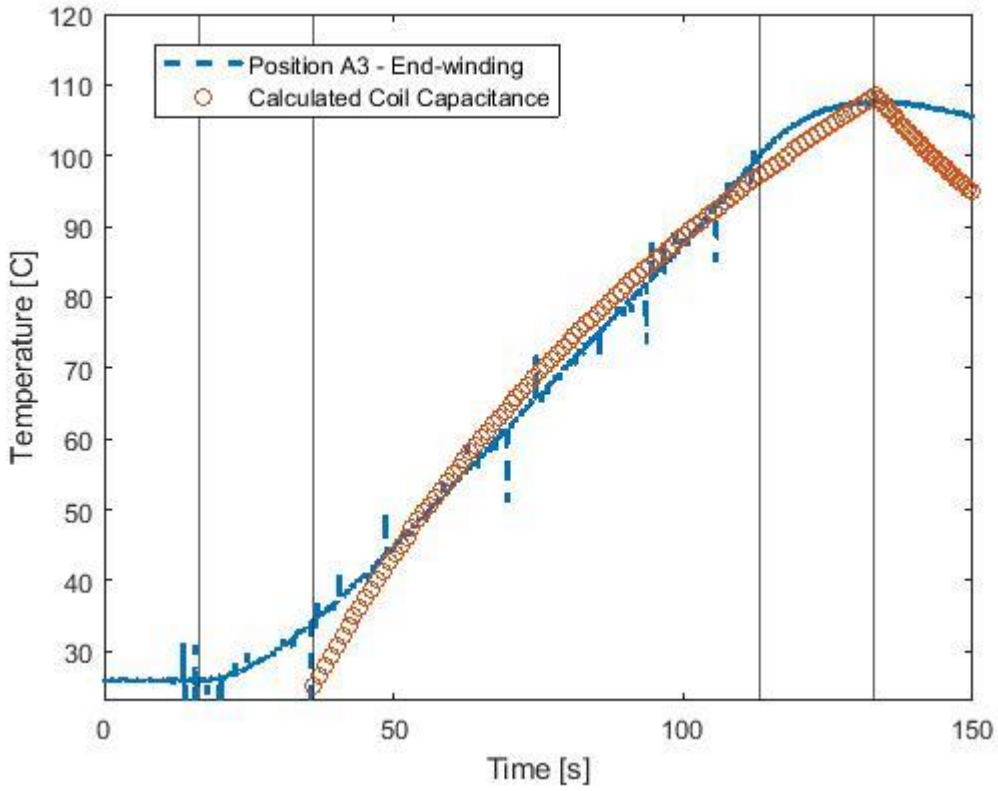

Figure 6-10: LPTN with MPF capacitance calculation plotted against the temperature profile for phase A, position 3 thermistor

Considering the dramatic increase in the stator windings, and the low value for the housing in both experiment and model, can only the maximum winding temperature be modelled for high overload conditions? It has been proposed in other studies [26] that some number of components in the rest of the motor can be considered isothermal during the heating region. Whether or not the coil itself can be considered adiabatic will be explored in Chapter 7. Also, the MPF-LPTN model will be examined for the likelihood of validity at other operating points.

Chapter 7

SENSITIVITY ANALYSIS OF VALIDATED LUMPED PARAMETER THERMAL NETWORK MODEL

The Maximum Packing Factor (PF) model for capacitance, introduced in Chapter 6, is dependant on the number of strands, the number of turns, stack length, and the gauge of the wire. This is a physically accurate representation of the coil for heat transfer, which is also stated in terms of motor design parameters. Using this model, we can explore what is the impact of a more accurate thermal capacitance? How much does the capacitance of the coil have to change for the thermal model prediction to vary by more than a few degrees? Finally, how sensitive is the model hot-spot temperature to changes in coil capacitance versus changing the capacitance of other components along the heat path? These questions will be addressed in this chapter.

7.1 Dynamics at Severe Overload Conditions

7.1.2 Hot-Spot Temperature Profile Sensitivity to Thermal Capacitance Variance

Varying the capacitance in a thermal model means varying the quantity of energy storage available to the system. In principle, the difference between steady-state and transient operation is whether this energy storage is 'at capacity' (in steady-state) or not (transient). As heat is generated in the system it raises the amount of energy stored in the system which we record as a temperature increase. Fig 7-1 shows the variation of thermal capacitance in the coil nodes. The default capacitance calculated by MotorCAD is compared against the Maximum PF capacitance value calculated in Chapter 6.

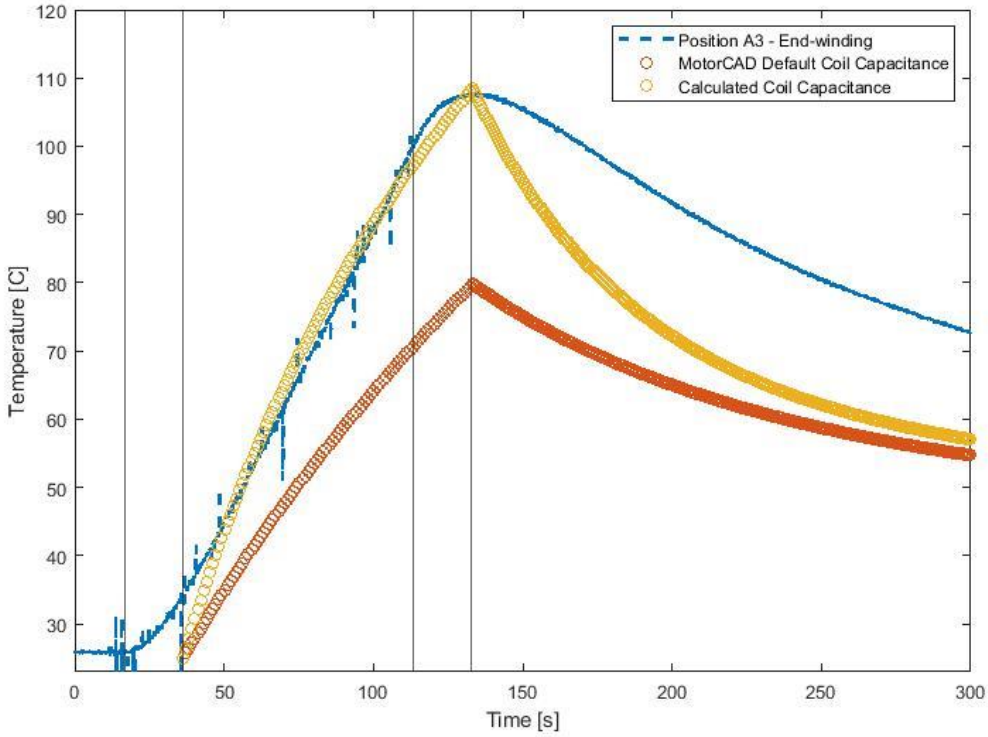

Figure 7-1: Variation in Coil Capacitance for Fifteen Cuboids

Table 7-1 breaks down the capacitance variation by cuboid for Fig 7-1, which uses fifteen cuboids. The total Maximum PF capacitance is 65% of the total MotorCAD capacitance and this variation causes a roughly 30 °C difference in peak temperature.

Table 7-1: Variation of Coil Thermal Capacitances

	Maximum PF Model - End Winding (J/C)	Maximum PF Model - Active Length (J/C)	MotorCAD -End Winding (J/C)	MotorCAD - Active Length (J/C)
1	49.77	146.02	60.22	176.66
2	49.77	146.02	81.01	237.62
3	49.77	146.02	99.54	291.98
4	49.77	146.02	80.29	235.53
5	49.77	146.02	57.31	168.11

While the rate of heating and peak temperature match well in Fig 7-1 to the experiment, we see a noticeable deviation in the cooling region. Recall that the definition of a lumped parameter region is one in which we can consider the temperature within a volume to be uniform. For small temperature gradients, the lumped parameter volume can be large and for large temperature gradients, the lumped parameter volume will be small. The stator laminations represent a large

thermal capacitance compared to the coil. If the coil were able to access this thermal capacitance effectively over the time the motor was running, we would expect a low coil temperature as the stator capacitance ‘filled’. However, this is not what we observe. Instead, Boglietti et al. proposed that for short-time thermal transients the coil could be considered adiabatic and the rest of the motor could be considered isothermal, which they defined as temperature rise less than 1 °C [71]. We could imagine that we could also consider the coil adiabatic if a large change in stator capacitance had a correspondingly small change in peak temperature. This would imply that a small temperature gradient existed inside the stator and that the winding hot spot was not meaningfully able to access the stator thermal capacity. Fig 7-2 shows the results of varying the stator, rotor, end-plate and axle capacitances, which are detailed in Table 7-2.

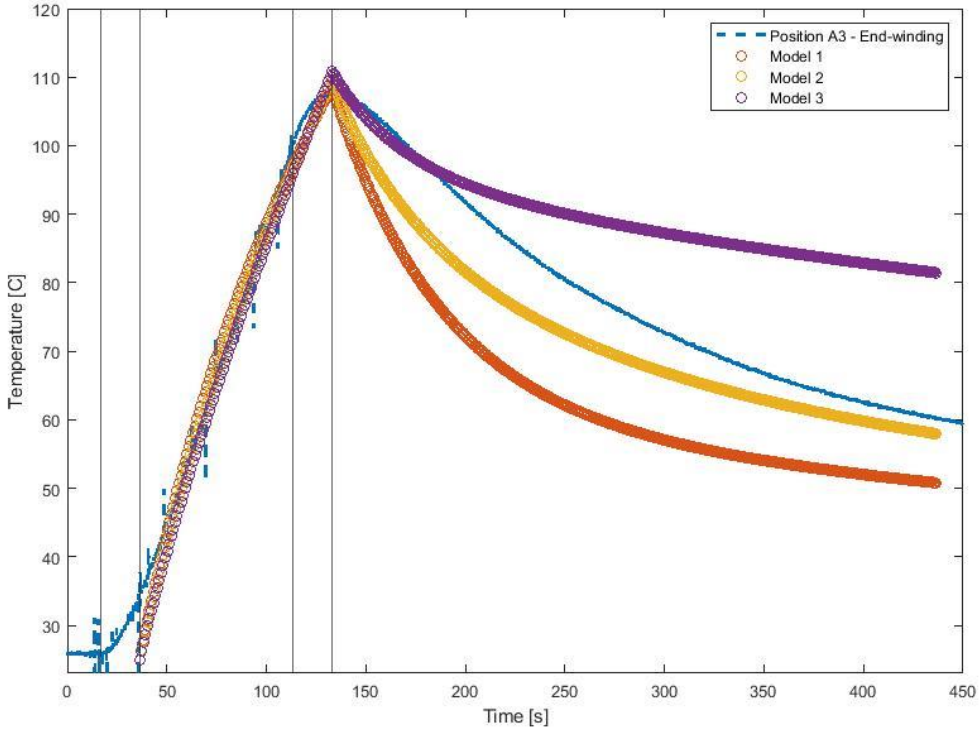

Figure 7-2: Reduction in stator capacitance by component,

for the three models shown in Table 7-2

Table 7-2: Variation of Stator Thermal Capacitances

Component	Model 1: Full Stator Capacitance (J/C)	Model 2: Stator Tooth Reduced Capacitance (J/C)	Model 3: All Capacitance Reduced (J/C)
Tooth	770.04	50.00	5.00
Stator Yoke	462.64	462.64	10.00
Stator Surface	256.68	256.68	1.00

Rotor Surface	79.97	79.97	1.00
Rotor Tooth	159.93	159.93	3.00
Axle Centre	732.62	732.62	50.00
Rotor Yoke	1102.11	1102.11	10.00
End Caps	1927.54	1927.54	10.00

There is a difference of 5401.54 J/C between Model 1 which is the default MotorCAD capacitance, and Model 3, where all non-components have been greatly reduced in capacitance. And yet, for the first 50 seconds after the maximum temperature is reached Model 3 does a much better job of estimating the temperature. This result supports the conclusion that for severe overload conditions the coil can be considered adiabatic for short periods. This implies we can indeed reduce the complexity of the rest of the motor to assume near-isothermal conditions, as was done by Bogletti et al. and Buyukdegirmenci et al. [71], [79]. However, our result implies additional critical information: variation in the coil capacitance greatly affects the outcome of the hot-spot temperature accuracy even in a reduced-order model. Thus, for short term transient operation, which occurs very frequently in traction motor drive-cycles, the need for accurate coil thermal capacitance modelling is paramount. Both the lumped value of capacitance and in terms of number of lumped regions are critical factors in this result, which must be tied back to motor parameters as we have done here.

7.2 Dynamics Over the Operating Envelope

We've classified the operating point in Chapter 6 as a severe overload condition such that within a reasonable margin of error the coil can be considered adiabatic. However, that corresponds to a peak current of about 55 A, for a machine that reaches a peak current of 76.5A at peak torque [69]. What about the operating points at smaller values of peak current?

A series of operating points were run throughout the torque-speed map. Temperatures were recorded by the interior thermistors for short periods. The operating points were each attained by the motor for about a minute before the temperature recording which lasted five seconds. These temperature 'snapshots' are in the heating regime after the heating temperature lag region is described in Chapter 6. For each of these snapshots, a line equation was fit and the slope of each line was recorded, i.e. the heating rate. Fig 7-3 shows the heating rate increases at a constant rate with current under low speeds, and increasingly deviates from this profile at higher speeds. At high speeds, the heating rate of the motor will be influenced by the higher convection heat transfer coefficient interior and exterior to the motor.

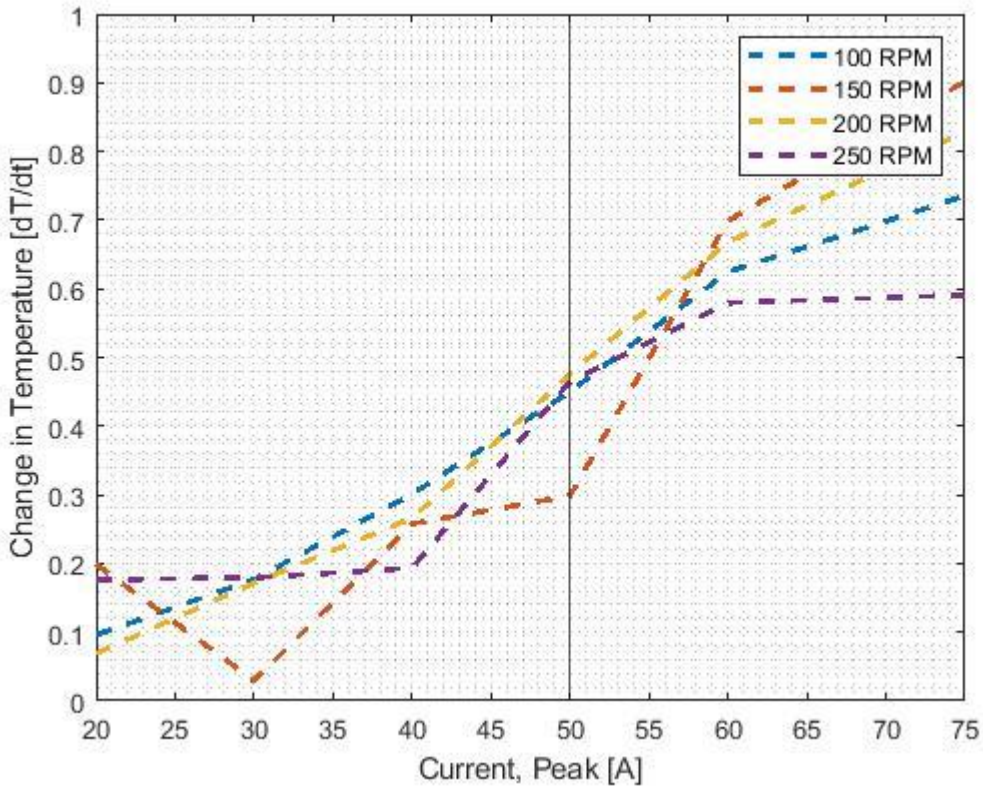

Figure 7-3: Change in dT/dt by operating point for five-second temperature 'snapshots'

Between 20-30A the value of $^{dT}/_{dt}$ for all speeds is approximately constant, however above 50A the values diverge. At low levels of peak current, and therefore low copper loss, there is simply less heat to remove from the coils regardless of how fast the motor is going.

Figure 7-4 shows the temperature profile for 25A,150 RPM using the capacitance model schemes from Table 7-2. The profiles mimic the curves shown in Figure 7-2 for our overload condition, but now the difference between Model 1 and Model 3 at 400 s is only 3°C.

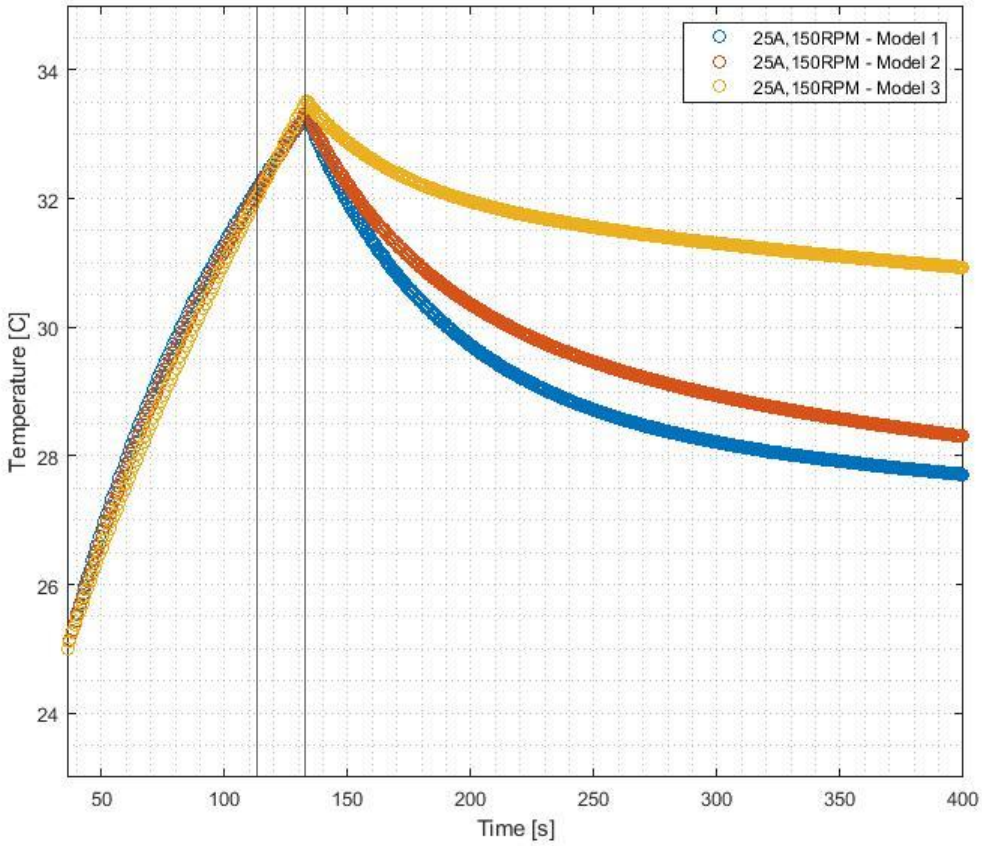

Figure 7-4: Change in Cooling Profile with Reducing Thermal Capacitance for 25A peak, 150 RPM

The transition observed in Fig 7-3 could be the point at which the convective heat transfer coefficient begins to dominate the temperature profile. This would imply that the adiabatic assumption made for the coil in 7.1 may not be valid for overload conditions at high speeds. Additional experimental testing would need to be done to confirm this hypothesis.

Chapter 8

CONCLUSIONS AND FUTURE WORK

8.1 Summary and Conclusions

In this thesis, the transient thermal response of a 12-16 ERSRM for an E-bike application has been characterized. However, the results can be applied to other high-performance power-dense applications with short-time transients or duty-cycles such as traction motors (automotive, railway, heavy industry), aerospace (aircraft, satellites) or any application that requires short, high power bursts of performance, such as aircraft launch systems on aircraft carriers.

The thermal modelling approaches presented in this work show how an appropriate combination of analytical methods from machine design, materials and heat transfer can solve complicated physical problems that no one of them could solve. The developed thermal models are simple, yet accurate descriptions of heat transfer in electric machines. Their simplicity owes to their success, allowing their use in many types of thermal modelling applications, such as

reduced-order modelling for online temperature estimation and multi-objective motor design optimization.[81]

In Chapter 5, the heat paths and dynamics of external rotor motors were reviewed and the importance of considering coil and slot anisotropy was emphasized. Contrary to the trend of homogenization in thermal winding models, an anisotropic materials-based approach was adopted. By considering the region of local thermal equilibrium within the coil a characteristic length for the validity of the lumped parameter approximation was discovered. An analytical proof was provided that a small number of capacitances is not sufficient to model a typical power-dense coil design. A sizing criterion was proposed for the cuboid number in a physically accurate LPTN coil model design. This sizing criterion considers the change in model size with motor speed or forced convection which allows us to *adaptively nodalize* the motor coil, giving tremendous design power to the designer for large data sets. Even if the number of cuboids for a physical calculation would need would be unfeasible for calculation, by correlating to the Biot number the margin of error from an improperly lumped system can be calculated.

In Chapter 6, the Maximum Packing Factor (MPF) method for calculating coil capacitance based on machine design parameters was introduced and implemented into a standard commercial LPTN. The ease of design allowed the calculation to be integrated without issue, and the combined MPF-LPTN was validated with experimental results. With a more accurate calculation of

capacitance within the coil and a known number of cuboids in the coil, we can approach a more physically accurate estimation of coil hot-spot temperature. The MPF method is highly applicable to other motors, based on its dependency on coil design parameters. Specifically, the MPF method's dependency on critical electromagnetic design criteria allows for coupled electromagnetic-thermal stator slot design optimization[82]. It provides a bridge between the effects on thermal and motor performance for the same parameter change. This is highly valuable to design parameter identification.

In Chapter 7, the impact of a more accurate capacitance calculation method on motor temperature was investigated for overload and rated operation. During overload conditions, it was found that the standard capacitance calculation from commercial software massively underestimated the heating rate and peak temperature of the coil hot-spot, even with the same number of cuboids. With the confidence of the physically accurate coil capacitance, the capacitance of the rest of the motor was able to be varied and investigated for its effects on cooldown dynamics. It was found that for short-time transients the rest of the motor could have its capacitances reduced or eliminated, immensely speeding up calculation time. At its extreme, the 61-node model under investigation was transformed into effectively a 'reduced-order model' of only 15 nodes with capacitance values. This aligned with previous work that had predicted the coil to act adiabatically in this operating range. Also, operating points across the operating envelope for the motor under study were mapped to determine the region where the adiabatic

assumption could be made. It was shown that a transition occurred at high-speed where high-current points did not maintain the same rate of heating at the same points. This result is expected due to the 'turn on' of higher values of h at higher motor speeds but indicates that care must be taken to determine when the adiabatic assumption ceases to be valid.

8.2 Future Work

The work presented is an exploratory study that has adapted a physical sciences perspective to motor applications. Continued work should be done to develop and grow the robustness of the models presented. The affect of increasing the number of cuboids on the system should be more thoroughly studied, with an experimentally validated value for the convective heat transfer coefficient. Future study should include the determination of a convection correlation for the ERSRM. This would allow a greater understanding of the dynamics studied in section 7.1.2. This study has identified there is a gap in our understanding of the dynamics between the coil and the rest of the machine in overload conditions for external rotor motors. However, more work needs to be done to fully address it. By having a greater confidence in the value of h, the dynamics of section 7.1.2 could be understood with more clarity.

In addition, a thorough independent experimental study of coil capacitance would be valuable to determine the accuracy of the MPF model proposed. The packing factor could be measured experimentally for several different types of coil

configurations and encapsulants to add as a factor to the MPF model for added accuracy.

Finally, a study to understand the computational requirements of the reduced order model and how it can be optimized would be beneficial to understand the systems this work can be applied to. Thus, these methods should be applied to thermal models designed for other highly transient problems and applications including, but not limited to:

1. Application to other power-dense motor types and configurations and validated to confirm generalizability, as well as determine the requirements for ‘the adiabatic assumption’
2. Use this tool to design and evaluate active and passive thermal management techniques
3. Apply as part of the optimization criteria for a coupled electromagnetic-thermal motor design optimization
4. Apply the coil temperature prediction as boundary conditions in a transient CFD calculation of air-gap and end-winding regions. Also, use CFD or experimental calculations to get a better idea of local values of h along the coil surface. to better determine the value of h for this
5. Integration into an online estimation model and included in a control technique like Model Predictive Control (MPC).

The tools presented allows for the evaluation of adding additional heat paths from convection and radiation thermal management on coil thermal dynamics. Better transient utilization of the available thermal capacity of the motor would take better advantage of the stator back-iron thermal capacitance. This suggests a change in motor design or thermal management design objective, where a knowledge of the behaviour discussed could be integrated into early trade-off decisions. For instance, adding a highly thermally conductive polymer encapsulant around the end-windings would allow for an additional heat path with more surface area from a hot-spot region. More direct contact means greater utilization of thermal capacitance of the stator back iron. The gap that this thesis has attempted to address opens the door to answering some of these questions. It is my hope that future work will continue to grow and address finding unexpected answers to non-intuitive questions.

Bibliography

[1] B. Bilgin and A. Emadi, “Electric motors in electrified transportation: A step toward achieving a sustainable and highly efficient transportation system,” *IEEE Power Electron. Mag.*, vol. 1, no. 2, pp. 10–17, Jun. 2014, doi: 10.1109/MPEL.2014.2312275.

[2] C. Kral, A. Haumer, and S. Bin Lee, “A practical thermal model for the estimation of permanent magnet and stator winding temperatures,” *IEEE Trans. Power Electron.*, vol. 29, no. 1, pp. 455–464, 2014, doi: 10.1109/TPEL.2013.2253128.

[3] X. Yi and K. S. Haran, “Transient Performance Study of High-Specific-Power Motor Integrated with Phase Change Material for Transportation Electrification,” 2020, pp. 119–124, doi: 10.1109/itec48692.2020.9161727.

[4] A. Boglietti, A. Cavagnino, D. Staton, M. Shanel, M. Mueller, and C. Mejuto, “Evolution and modern approaches for thermal analysis of electrical machines,” in *IEEE Transactions on Industrial Electronics*, 2009, vol. 56, no. 3, pp. 871–882, doi: 10.1109/TIE.2008.2011622.

[5] W. D. Callister and D. G. Rethwisch, *Materials Science and Engineering: An Introduction*, 10th ed. New York: John Wiley & Sons, 2018.

[6] J. R. Howell, R. Siegel, and M. P. Mengüç, *Thermal Radiation Heat Transfer, 5th Edition*, 5th ed. Boca Raton: CRC Press, 2011.

[7] Y. A. Cengel and A. J. Ghajar, *Heat and Mass Transfer, Fundamentals & Application*, 5th ed. McGraw-Hill, 2015.

[8] R. Harris, *Nonclassical Physics: Beyond Newton's View*. Pearson, 1999.

[9] B. Bilgin *et al.*, "Modeling and Analysis of Electric Motors: State-of-the-Art Review," *IEEE Trans. Transp. Electrif.*, vol. 5, no. 3, pp. 602–617, 2019, doi: 10.1109/TTE.2019.2931123.

[10] K. Stowe, *An Introduction to Thermodynamics and Statistical Mechanics*, 2nd ed. Cambridge University Press, 2007.

[11] B. W. Carroll and D. A. Ostlie, *An introduction to modern astrophysics and cosmology*, 2nd ed. Cambridge University Press, 2017.

[12] F. P. Incropera and D. P. DeWitt, *Fundamentals of Heat and Mass Transfer*. New York: J. Wiley, 2002.

[13] W. A. Gray and R. Muller, "Direct Radiative Transfer," in *Engineering Calculations in Radiative Heat Transfer*, 1st ed., D. W. Hopkins, Ed. Pergamon, 1974.

[14] "Heat Transfer Data Book," Schenectady, NY, USA, 1977.

[15] Aldo Boglietti, Andrea Cavagnino, David Staton, Martin Shanel, Markus Mueller, and Carlos Mejuto, "Evolution and Modern Approaches for Thermal Analysis of Electrical Machines," *IEEE Trans. Ind. Electron.*, vol.

56, no. 3, pp. 871–882, 2009, doi: 10.1109/TIE.2008.2011622.

[16] B. Bilgin, “Electromagnetic Principles of Switched Reluctance Machines,” in *Switched Reluctance Motor Drives: Fundamentals to Applications*, 1st ed., B. Bilgin, J. W. Jiang, and A. Emadi, Eds. Boca Raton: CRC Press, 2019.

[17] N. Schofield, “ECE 788 - Electric Machine Design.” McMaster University, 2015.

[18] E. Rowan and J. Jiang, “Materials used in Switched Reluctance Machines,” in *Switched Reluctance Motor Drives: Fundamentals to Applications*, 1st ed., B. Bilgin, J. W. Jiang, and A. Emadi, Eds. Boca Raton: CRC Press, 2019.

[19] S. Chapman, *Electric Machinery Fundamentals*. New York: McGraw-Hill, 2012.

[20] J. Ye, H. Li, and J. W. Jiang, “Control of Switched Reluctance Machines,” in *Switched Reluctance Motor Drives: Fundamentals to Applications*, 1st ed., B. Bilgin, J. W. Jiang, and A. Emadi, Eds. Boca Raton: CRC Press, 2019.

[21] B. Howey and H. Li, “Operational Principles and Modelling of Switched Reluctance Machines,” in *Switched Reluctance Motor Drives: Fundamentals to Applications*, 1st ed., B. Bilgin, J. W. Jiang, and A. Emadi, Eds. Boca Raton: CRC Press, 2019.

[22] J. W. Jiang, Y. Yang, and E. Rowan, “Thermal Management in Switched

Reluctance Motors," in *Switched Reluctance Motor Drives: Fundamentals to Applications*, 1st ed., B. Bilgin, J. W. Jiang, and A. Emadi, Eds. Boca Raton: CRC Press, 2019.

[23] B. Bilgin *et al.*, "Modeling and Analysis of Electric Motors: State-of-the-Art Review," *IEEE Trans. Transp. Electrif.*, vol. 5, no. 3, pp. 602–617, 2019, doi: 10.1109/TTE.2019.2931123.

[24] C. Roth, F. Birnkammer, and D. Gerling, "Analytical Model for AC Loss Calculation Applied to Parallel Conductors in Electrical Machines," in *Proceedings - 2018 23rd International Conference on Electrical Machines, ICEM 2018*, 2018, pp. 1088–1094, doi: 10.1109/ICELMACH.2018.8507237.

[25] G. Volpe, "Accounting for AC Winding Losses in the Electric Machine Design Process," 2018.

[26] F. Qi, M. Schenk, and R. W. De Doncker, "Discussing details of lumped parameter thermal modeling in electrical machines," in *IET Conference Publications*, 2014, vol. 2014, no. 628 CP, doi: 10.1049/cp.2014.0479.

[27] M. Torrent, P. Andrada, B. Blanqué, E. Martinez, J. I. Perat, and J. A. Sanchez, "Method for estimating core losses in switched reluctance motors," *Eur. Trans. Electr. Power*, vol. 21, no. 1, pp. 757–771, Jan. 2011, doi: 10.1002/etep.475.

[28] R. Harris, *Modern Physics*. Pearson/Addison Wesley, 2008.

[29] D. C. Jiles and D. L. Atherton, “Theory of ferromagnetic hysteresis,” *J. Magn. Magn. Mater.*, vol. 61, no. 1–2, pp. 48–60, Sep. 1986, doi: 10.1016/0304-8853(86)90066-1.

[30] S. Y. R. Hui and J. Zhu, “Magnetic hysteresis modeling and simulation using the Preisach theory and TLM technique,” in *PESC Record - IEEE Annual Power Electronics Specialists Conference*, 1994, vol. 2, pp. 837–842, doi: 10.1109/pesc.1994.373776.

[31] H. Jordan, “Die ferromagnetischen Konstanten für schwache Wechselfelder,” *Elektr. Nach. Techn*, 1924.

[32] J. Reinert, A. Brockmeyer, and R. W. A. A. De Doncker, “Calculation of losses in ferro- and ferrimagnetic materials based on the modified Steinmetz equation,” *IEEE Trans. Ind. Appl.*, vol. 37, no. 4, pp. 1055–1061, Jul. 2001, doi: 10.1109/28.936396.

[33] J. Coey, *Magnetism and Magnetic Materials*. Cambridge University Press, 2009.

[34] P. Beckley, *Electrical Steels for Rotating Machines*. 2002.

[35] C. P. Steinmetz, “On the law of hysteresis,” *Proc. IEEE*, vol. 72, no. 2, pp. 197–221, 1984, doi: 10.1109/PROC.1984.12842.

[36] Q. Yu, B. Bilgin, and A. Emadi, “Loss and Efficiency Analysis of Switched Reluctance Machines Using a New Calculation Method,” *IEEE Trans. Ind. Electron.*, vol. 62, no. 5, pp. 3072–3080, May 2015, doi: 10.1109/TIE.2015.2392716.

[37] A. Al-Timimy, G. Vakil, M. Degano, P. Giangrande, C. Gerada, and M. Galea, “Considerations on the Effects That Core Material Machining Has on an Electrical Machine’s Performance,” *IEEE Trans. Energy Convers.*, vol. 33, no. 3, pp. 1154–1163, 2018, doi: 10.1109/TEC.2018.2808041.

[38] C. C. Chiang *et al.*, “Effects of annealing on magnetic properties of electrical steel and performances of SRM after punching,” *IEEE Trans. Magn.*, vol. 50, no. 11, Nov. 2014, doi: 10.1109/TMAG.2014.2329708.

[39] Y. A. Cengel and A. J. Ghajar, *Heat and Mass Transfer, Fundamentals & Application, Fifth Edition in SI Units*. 2015.

[40] Z. Lan, X. Wei, and L. Chen, “Thermal analysis of PMSM based on lumped parameter thermal network method,” *19th Int. Conf. Electr. Mach. Syst. ICEMS 2016*, 2017.

[41] D. Kuehbacher, A. Kelleter, and D. Gerling, “An improved approach for transient thermal modeling using lumped parameter networks,” *Proc. 2013 IEEE Int. Electr. Mach. Drives Conf. IEMDC 2013*, pp. 824–831, 2013, doi: 10.1109/IEMDC.2013.6556188.

[42] P. Romanazzi, V. Galizzi, F. Carbone, A. Miotto, and D. A. Howey, “Improved thermal equivalent circuit element applied to an external rotor SPM machine,” *Proc. - 2016 22nd Int. Conf. Electr. Mach. ICEM 2016*, no. 2, pp. 2718–2724, 2016, doi: 10.1109/ICELMACH.2016.7732906.

[43] F. Qi, A. Stippich, M. Guettler, M. Neubert, and R. W. De Doncker, “Methodical considerations for setting up space-resolved lumped-parameter thermal models for electrical machines,” *2014 17th Int. Conf. Electr. Mach. Syst. ICEMS 2014*, pp. 651–657, 2014, doi: 10.1109/ICEMS.2014.7013567.

[44] T. Lange, F. Qi, J. Dehn, and R. W. De Doncker, “Synchronous machine model considering dynamic losses and thermal behavior,” pp. 536–542, 2016, doi: 10.1109/iemdc.2015.7409110.

[45] G. Guedia Guemo, P. Chantrenne, and J. Jac, “Application of classic and T lumped parameter thermal models for Permanent Magnet Synchronous Machines,” *Proc. 2013 IEEE Int. Electr. Mach. Drives Conf. IEMDC 2013*, pp. 809–815, 2013, doi: 10.1109/IEMDC.2013.6556186.

[46] J. H. Lienhard IV and J. H. Lienhard V, *A Heat Transfer Textbook*, 5th ed. Mineola, NY: Dover Publications, 2019.

[47] P. H. Mellor, D. Roberts, and D. R. Turner, “Lumped parameter thermal model for electrical machines of TEFC design,” *IEE Proc. B Electr. Power*

Appl., vol. 138, no. 5, pp. 205–218, 1991, doi: 10.1049/ip-b.1991.0025.

[48] G. Kylander, “Thermal modelling of small cage induction motors,” Chalmers University of Technology, 1995.

[49] N. Rostami, M. R. Feyzi, J. Pyrhonen, A. Parviainen, and M. Niemela, “Lumped-parameter thermal model for axial flux permanent magnet machines,” *IEEE Trans. Magn.*, vol. 49, no. 3, pp. 1178–1184, 2013, doi: 10.1109/TMAG.2012.2210051.

[50] K. Bennion, “Electric Motor Thermal Management,” 2012.

[51] D. Staton, A. Boglietti, and A. Cavagnino, “Solving the more difficult aspects of electric motor thermal analysis in small and medium size industrial induction motors,” *IEEE Trans. Energy Convers.*, vol. 20, no. 3, pp. 620–628, 2005, doi: 10.1109/TEC.2005.847979.

[52] A. Tovar-Barranco, A. Lopez-de-Heredia, I. Villar, and F. Briz, “Modeling of End-Space Convection Heat-Transfer for Internal and External Rotor PMSMs with Fractional-Slot Concentrated Windings,” *IEEE Trans. Ind. Electron.*, vol. 0046, no. c, pp. 1–1, 2020, doi: 10.1109/tie.2020.2972471.

[53] F. Chauvicourt, P. Romanazzi, D. Howey, A. Dziechciarz, C. Martis, and C. T. Faria, “Review of multidisciplinary homogenization techniques applied to electric machines,” *2016 11th Int. Conf. Ecol. Veh. Renew. Energies, EVER 2016*, 2016, doi: 10.1109/EVER.2016.7476431.

[54] G. J. Li, J. Ojeda, E. Hoang, M. Lecrivain, and M. Gabsi, “Comparative studies between classical and mutually coupled switched reluctance motors using thermal-electromagnetic analysis for driving cycles,” *IEEE Trans. Magn.*, vol. 47, no. 4, pp. 839–847, 2011, doi: 10.1109/TMAG.2011.2104968.

[55] A. M. El-Refaie, N. C. Harris, T. M. Jahns, and K. M. Rahman, “Thermal analysis of multibarrier interior PM synchronous machine using lumped parameter model,” *IEEE Trans. Energy Convers.*, vol. 19, no. 2, pp. 303–309, Jun. 2004, doi: 10.1109/TEC.2004.827011.

[56] J. F. Trigeol, Y. Bertin, and P. Lagonotte, “Thermal modeling of an induction machine through the association of two numerical approaches,” *IEEE Trans. Energy Convers.*, vol. 21, no. 2, pp. 314–323, Jun. 2006, doi: 10.1109/TEC.2005.859964.

[57] J. Nerg, M. Rilla, and J. Pyrhönen, “Thermal analysis of radial-flux electrical machines with a high power density,” *IEEE Trans. Ind. Electron.*, vol. 55, no. 10, pp. 3543–3554, 2008, doi: 10.1109/TIE.2008.927403.

[58] R. Wrobel and P. H. Mellor, “A general cuboidal element for three-dimensional thermal modelling,” *IEEE Trans. Magn.*, vol. 46, no. 8, pp. 3197–3200, 2010, doi: 10.1109/TMAG.2010.2043928.

[59] L. Hosain and R. Bel, “Air-Gap Heat Transfer in Rotating Electrical

Machines : A Parametric Study," *Energy Procedia*, vol. 142, no. August, pp. 4176–4181, 2017.

[60] M. Fénot, Y. Bertin, E. Dorignac, and G. Lalizel, "A review of heat transfer between concentric rotating cylinders with or without axial flow," *Int. J. Therm. Sci.*, vol. 50, no. 7, pp. 1138–1155, 2011, doi: 10.1016/j.ijthermalsci.2011.02.013.

[61] M. Fénot, E. Dorignac, A. Giret, and G. Lalizel, "Convective heat transfer in the entry region of an annular channel with slotted rotating inner cylinder," *Appl. Therm. Eng.*, vol. 54, no. 1, pp. 345–358, 2013, doi: 10.1016/j.applthermaleng.2012.10.039.

[62] P. Romanazzi and D. A. Howey, "Air-gap convection in a switched reluctance machine," *2015 10th Int. Conf. Ecol. Veh. Renew. Energies, EVER 2015*, 2015, doi: 10.1109/EVER.2015.7112962.

[63] K. M. Becker and J. Kaye, "Measurements of diabatic flow in an annulus with an inner rotating cylinder," *J. Heat Transfer*, vol. 84, no. 2, pp. 97–104, May 1962, doi: 10.1115/1.3684335.

[64] C. Micallef, S. J. Pickering, K. A. Simmons, and K. J. Bradley, "Improved cooling in the end region of a strip-wound totally enclosed fan-cooled induction electric machine," *IEEE Trans. Ind. Electron.*, vol. 55, no. 10, pp. 3517–3524, 2008, doi: 10.1109/TIE.2008.2003101.

[65] A. J. Grobler, S. R. Holm, and G. Van Schoor, “Empirical parameter identification for a hybrid thermal model of a high-speed permanent magnet synchronous machine,” *IEEE Trans. Ind. Electron.*, vol. 65, no. 2, pp. 1616–1625, Jul. 2017, doi: 10.1109/TIE.2017.2733499.

[66] A. B. I. C. I. Member *et al.*, “Evaluation of Radiation Thermal Resistances in Industrial Motors,” *IEEE Trans. Ind. Appl.*, vol. 42, no. 3, pp. 481–485, 2005, doi: 10.1109/TIA.2006.873655.

[67] J. R. Howell, R. Siegel, and M. P. Mengüç, *Thermal Radiation Heat Transfer*, 5th ed. Boca Raton: CRC Press, 2011.

[68] *Heat Transfer Data Book*. Schenectady, NY, USA: General Electric Co, 1977.

[69] B. Howey, “Non-Coupled and Mutually Coupled Switched Reluctance Machines for an E-Bike Traction Application: Pole Configurations, Design, and Comparison,” p. 404, 2018.

[70] M. F. Momen and I. Husain, “Design and performance analysis of a switched reluctance motor for low duty cycle operation,” *IEEE Trans. Ind. Appl.*, vol. 41, no. 6, pp. 1612–1618, 2005, doi: 10.1109/TIA.2005.858271.

[71] A. Boglietti, E. Carpaneto, M. Cossale, and S. Vaschetto, “Stator-Winding Thermal Models for Short-Time Thermal Transients: Definition and Validation,” *IEEE Trans. Ind. Electron.*, vol. 63, no. 5, pp. 2713–2721, 2016,

doi: 10.1109/TIE.2015.2511170.

[72] V. T. Buyukdegirmenci and P. T. Krein, “Induction Machine Characterization for Short-Term or Momentary Stall Torque,” *IEEE Trans. Ind. Appl.*, vol. 51, no. 3, pp. 2237–2245, 2015, doi: 10.1109/TIA.2014.2365633.

[73] “NEMA MW 1000 - Magnet Wire.” National Electrical Manufacturers Association (NEMA), Rosslyn, Virginia, USA, 2015.

[74] A. A. Wereszczak, J. E. Cousineau, K. Bennion, H. Wang, R. H. Wiles, and T. B. Burress, “Anisotropic thermal response of packed copper wire,” *J. Therm. Sci. Eng. Appl.*, vol. 9, no. 4, 2017, doi: 10.1115/1.4035972.

[75] A. Boglietti, I. R. Bojoi, S. Rubino, and M. Cossale, “Overload Capability of Multiphase Machines under Normal and Open-Phase Fault Conditions: A Thermal Analysis Approach,” *IEEE Trans. Ind. Appl.*, vol. 56, no. 3, pp. 2560–2569, 2020, doi: 10.1109/TIA.2020.2978767.

[76] N. Simpson, R. Wrobel, and P. H. Mellor, “Estimation of equivalent thermal parameters of impregnated electrical windings,” *IEEE Trans. Ind. Appl.*, vol. 49, no. 6, pp. 2505–2515, 2013, doi: 10.1109/TIA.2013.2263271.

[77] J. W. Jiang, “Design Considerations for Switched Reluctance Machines,” in *Switched Reluctance Motor Drives: Fundamentals to Applications*, 1st ed., B. Bilgin, J. W. Jiang, and A. Emadi, Eds. Boca Raton: CRC Press, 2019.

[78] R. Wrobel and P. H. Mellor, “Thermal design of high-energy-density wound components,” *IEEE Trans. Ind. Electron.*, vol. 58, no. 9, pp. 4096–4104, Sep. 2011, doi: 10.1109/TIE.2010.2093485.

[79] V. T. Buyukdegirmenci and P. T. Krein, “Machine characterization for short-term or instantaneous torque capabilities: An approach based on transient thermal response,” *Proc. 2013 IEEE Int. Electr. Mach. Drives Conf. IEMDC 2013*, pp. 801–808, 2013, doi: 10.1109/IEMDC.2013.6556185.

[80] L. Idoughi, X. Mininger, F. Bouillault, L. Bernard, and E. Hoang, “Thermal model with winding homogenization and FIT discretization for stator slot,” *IEEE Trans. Magn.*, vol. 47, no. 12, pp. 4822–4826, Dec. 2011, doi: 10.1109/TMAG.2011.2159013.

[81] C. Sciascera, P. Giangrande, L. Papini, C. Gerada, and M. Galea, “Analytical thermal model for fast stator winding temperature prediction,” *IEEE Trans. Ind. Electron.*, vol. 64, no. 8, pp. 6116–6126, 2017, doi: 10.1109/TIE.2017.2682010.

[82] N. Bracikowski, M. Hecquet, P. Brochet, and S. V. Shirinskii, “Multiphysics modeling of a permanent magnet synchronous machine by using lumped models,” *IEEE Trans. Ind. Electron.*, vol. 59, no. 6, pp. 2426–2437, 2012, doi: 10.1109/TIE.2011.2169640.

Appendix A: Lumped Parameter Thermal Network Model Parameters

Materials:

Material	Thermal Conductivity (W/m/C)	Specific Heat (J/kg/C)	Density (kg/m^3)	Components
M350-50A	30	460	7650	Rotor, Stator
Aluminum Alloy (Cast)	168	833	2790	Housing
Copper (Pure)	401	385	8933	Coils
Wire Insulation	0.21	1000	1400	Wire
Varnish	0.2	1700	1400	Coils
Nomex	0.21	1000	700	Slot Liner

Input Data:

Parameter	Value	Unit
Copper loss (increases with coil temperature)	325	W
Speed	150	RPM
Lamination Stacking Factor	0.97	-
Ambient Temperature	25	Celsius
Altitude	0	m

Model Heat Transfer Values:

Type	Value	Area Affected
Effective Radial k Value	0.84	Coil active length, coil end winding
Effective Axial k Value	258.4	Coil active length, coil end winding
h, convection, end space	12.94	End winding, rotor tooth, axle, bearings, endcap, housing
h, convection, ambient	14.98	shaft
h, convection, airgap	65.94	airgap
h, radiation, airgap	4.934	airgap

Thermal Resistances for Heat Paths Out of the Coil:

Resistance Name	Resistance Value	Node 1	Node 2
R_50	13.07	27 (rotor ES R	363 Ewdg Rear R C2
R_18	6.45	6 (housing OH R	336 Ewdg_outer_R (C1)
R_49	71.41	27 Rotor ES R	360 Ewdg Bore R (C2)
R_23	0.82	8 Ecap R	340 Ewdg Rear R (C1)

R_47	28.51	27 (rotor ES R	336 Ewdg_outer_R (C1)
R_48	13.07	27 Rotor ES R	340 Ewdg Rear R (C1)
R_41	13.07	26 Rotor ES F	333 Ewdg Front F C1
R_15	0.82	4 Ecap F	333 Ewdg Front F C1
R_76	0.28	342 Wedge	373 Winding Average C2
R_42	71.41	26 Rotor ES F	354 Ewdg Bore F C2
R_43	13.07	26 Rotor ES F	356 Ewdg Front F C2
R_10	6.45	2 Housing OH F	330 Ewdg Outer F C1
R_40	28.51	26 Rotor ES F	330 Ewdg Outer F C1
R_79	0.08	344 Liner C1	350 Winding Average C1
R_81	0.29	345 Liner Yoke	350 Winding Average C1
R_78	0.08	343 Slot Center C1	350 Winding Average C1
R_82	-0.86	345 Liner Yoke	370 Wdg Inner c (C2)
R_108	0.08	367 Liner C2	373 Winding Average C2

R_107	0.08	366 Slot Center C2	373 Winding Average C2

Cuboidal Dimensions:

Cuboid Number	Width	Height (mm)	Volume (mm^3)
1.00	6.32	8.59	2150.62
2.00	8.51	8.59	2892.81
3.00	10.45	8.59	3554.59
4.00	8.43	8.59	2867.38
5.00	6.02	8.59	2046.59